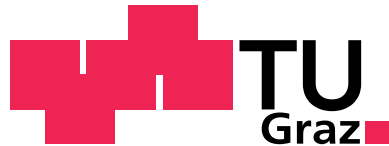Daniel Pieber, BSc

Physical Characterization of Low Hydrogen Plasma Enhanced Chemical Vapor Deposited Silicon Nitride

MASTER THESIS

For obtaining the academic degree
Diplom-Ingenieur

Master Programme of
Advanced Materials Science

GRAZ UNIVERSITY OF TECHNOLOGY

Supervisor:
Univ.-Prof. Ph.D. Peter Hadley
Institute of Solid State Physics

In cooperation with:
Infineon Technologies Austria AG

Villach, June 2015

Obstacles are what you see when you take your eyes off the goal.
(Vince Lombardi)

EIDESSTATTLICHE ERKLÄRUNG

AFFIDAVIT

Ich erkläre an Eides statt, dass ich die vorliegende Arbeit selbstständig verfasst, andere als die angegebenen Quellen/Hilfsmittel nicht benutzt, und die den benutzten Quellen wörtlich und inhaltlich entnommenen Stellen als solche kenntlich gemacht habe. Das in TUGRAZonline hochgeladene Textdokument ist mit der vorliegenden Masterarbeit/Diplomarbeit/Dissertation identisch.

I declare that I have authored this thesis independently, that I have not used other than the declared sources/resources, and that I have explicitly indicated all material which has been quoted either literally or by content from the sources used. The text document uploaded to TUGRAZonline is identical to the present master's thesis/diploma thesis/doctoral dissertation.

_____   _____

Datum / Date   Unterschrift / Signature

IV

Abstract

Silicon nitride films with thicknesses from 40 nm to 800 nm were deposited on 6 and 8 inch Si(100) substrate wafers inside PECVD reactors using a RF generator at 13.56 MHz. With designed experiments deposition recipes for films with a low Si-H bond concentration were tuned. A Matlab script was programmed to calculate the hydrogen content from FTIR absorption spectra as it is associated with changes of electrical properties and shortened lifetime of microelectronic devices. The bulk-limited Poole-Frenkel emission was found to be the dominating conduction mechanism through the dielectric films with trap depths of 0.45 eV and 0.59 eV for different $SiN_x{:}H_y$ variants. The average breakdown field strength was between 5.7 and 9.1 MV/cm. A correlation between Si-H bond concentration and leakage current was observed and a possible approach to predict the leakage current via refractive index measurements was presented.

Contents

List of Figures

List of Tables

1 Fundamentals

1.1 Dielectrics

Nonmetal materials which are insulators, or weakly conducting, with commonly fixed charge carriers are considered dielectric materials. A dielectric polarization can be observed in an applied electric field. This is because the electrons can not move like in conductors, but slightly shift out of their neutral position, as a reaction to the field. For the non-insulating dielectrics the conductivity is very low and the band gap is large. In general a material is called an insulator when the band gap is larger than 3 or 5 eV (depending on the source)[9].

The valence band is completely full, and the conduction band completely empty at 0 K. As the temperature rises some electrons can reach the conduction band due to thermal excitation and contribute to the current transport through the dielectric. Those electrons come either directly from the valence band or from donor impurity levels. Similarly holes accumulate in the valence band as excited electrons leave vacancies behind, or acceptor impurities generate some. However, if a large enough electric field is applied a conduction current through the dielectric can be measured.

1.1.1 Amorphous Silicon Nitride

Stoichiometric silicon nitride consists of the elements silicon and nitrogen and belongs to the group of non-oxide ceramics. The thermodynamic most stable compound of the silicon nitrides has the chemical formula Si_3N_4. It is almost as light as silicon carbide ($\rho \approx 3.3\,\mathrm{g/cm^3}$), shows good corrosion resistance, and provides a high fracture toughness ($K_{Ic} \approx 7\,\mathrm{MPa\,m^{1/2}}$) which makes it resistant to impacts and shocks. As its hardness is higher than the one from metals and high temperatures can be endured, it is a widespread engineering material. Due to the tribological properties it is used for example in wear-resistant precision bearings, molten metal handling applications or for cutting tools, when produced in bulk/monolithic form. To obtain a bulk/monolithic form, silicon powder compacts are generally nitrided and sintered, respectively[13].

A silicon nitride coating on the other hand is normally produced via a chemical vapor deposition (CVD) process (sec. 1.2.2). Reacting silane (SiH_4) with ammonia (NH_3)

at 700-900 °C at atmospheric pressure causes for instance a deposition of stoichiometric Si_3N_4[11].

$$3SiH_4 + 4NH_3 \xrightarrow{700\text{-}900°C} Si_3N_4 + 12H_2 \tag{1.1}$$
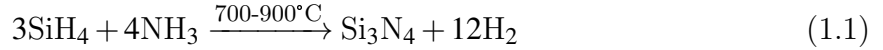
Low-Pressure CVD (LPCVD), which utilizes the following reaction chemistry, yields high quality nitride but has a low deposition rate[24]

$$3SiCl_2H_2(g) + 4NH_3(g) \xrightarrow{700\text{-}800°C} Si_3N_4(s) + 6HCl(g) + 6H_2(g) \tag{1.2}$$
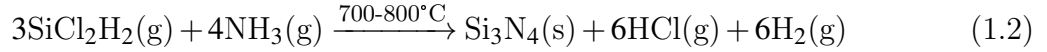
For silicon nitride produced by a conventional chemical or physical vapor deposition technique the stoichiometry (Si/N ratio) is virtually assured to be Si_3N_4. When the deposition technique is Plasma-Enhanced CVD (PECVD) however, the stoichiometry can be controllably varied with the process parameters[11, 38]. During plasma deposition up to 35 at% hydrogen can be incorporated into the compound, which then yields hydrogenated amorphous silicon nitride layers (a-$SiN_x:H_y$)[11, 25]. To keep the impurity level as low as possible SiH_4 chemistry is adopted and the overall reaction is as follows[24]

$$SiH_4(g) + NH_3(g) + N_2(g) \xrightarrow[\text{RF plasma}]{200\text{-}500°C} Si_xN_yH_z(s) + \text{byproducts} \tag{1.3}$$
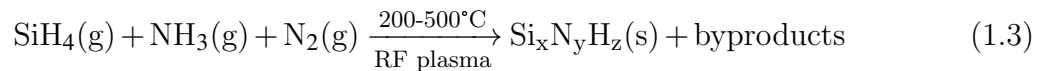
Amorphous solids in general do not possess a long-range crystalline order, instead they show a short-range order which is characterized by an average number of nearest neighbors, the coordination number and the mean separation of atoms. In [16], however, also the formation of small crystalline areas within the amorphous bulk material is reported.

Almost stoichiometric LPCVD Si_3N_4 contains less (up to 8 at%) hydrogen and has a higher resistivity and dielectric strength than PECVC silicon nitride but it also experiences strong tensile stress, causing film cracking in thick (> 2000 Å) films[11, 24]. PECVD films in contrast can even have compressive stress and they are deposited at a higher rate. Therefore, LPCVD Si_3N_4 is a good material for a capacitor dielectric (low leakage current and high breakdown voltage), whereas PECVD nitride is mainly used as diffusion barrier or final passivation layer.

1.1.2 Importance of Dielectrics in Semiconductor Devices

Dielectric films are of high importance in lots of applications, especially in integrated circuits (ICs). For example the concept of metal-oxide-semiconductor field effect transistors (MOSFETs) is based on the modulation of channel carriers by an applied voltage at the gate-contact across a thin dielectric. Furthermore neither dynamic random access memories would exist without the capacitor dielectric, nor flash memories without the built-in tunneling dielectric. That is why especially the semiconductor industry is interested in

knowing the properties of dielectrics, with focus on the electric properties.

PECVD Silicon nitride is used in the semiconductor industry mainly as an insulation or passivation layer on the devices as they can serve as diffusion barriers against moisture and mobile ions (sodium)[20]. Ultrathin Si_3N_4 films ($d < 100\,Å$) are also known to be capable of replacing ultrathin SiO_2 films in very-large-scale integration (VLSI) applications as they have a higher dielectric constant than SiO_2. Further on their characteristics do not degrade during high-energy processes (e.g., ion implantation, plasma etching)[28]. General requirements for such dielectric layers are a high uniformity across the wafer, low internal stresses and an adjustable refractive index (RI) to just name a few. For $SiN_x:H_y$ films also the concentration of hydrogen should be kept low as it has been reported to be responsible for degrading MOSFET device lifetimes[7].

1.1.3 Characterization of Electrical Properties

To be able to measure conduction mechanisms in a dielectric, it is necessary to prepare samples. The metal-insulator-metal (MIM) and the metal-insulator-semiconductor (MIS) structures are the ones generally used for sample testing purposes. By applying an electric field and measuring the current conduction, the voltage-current (U-I) characteristic of the dielectric is recorded. In MIM structures the electric field shows an asymmetry when for top and bottom electrode different materials are used. This is because different metals generally lead to distinct work functions which are connected with different metal-dielectric interface barriers. MIS structures have this kind of asymmetry by nature, nevertheless the MIS capacitor is a convenient device for studying semiconductor surfaces and investigating electrical properties of dielectric to semiconductor interfaces.[9]

To ensure that for the tests the semiconductor has a good electrical contact, the substrate silicon wafers in this work are highly doped (n+ type, ρ=0.008-0.030 Ωcm). Because of this very high doping it is appropriate to consider the structure used in this work as a MIM-structure.

1.1.4 Conduction Mechanisms in Dielectrics

For dielectrics two general types of conduction mechanisms exist, that is, electrode-limited conduction mechanism and bulk-limited conduction mechanism. When the electrical properties at the electrode-dielectric interface are dominating the electric behavior, electrode-limited conduction mechanism is present. It is also called injection-limited conduction. In that case it is possible to extract physical properties of the barrier height at the interface as well as the effective mass of the conduction carriers in the dielectric film. In case of the bulk-limited conduction mechanism, which is also called transport-limited conduction mechanism, only the electric properties of the dielectric itself are dominating. Among

other important properties trap level, trap spacing and trap density can be obtained from an analysis[9]. Trap spacing and density are not necessarily directly related as, e.g. in case of crystalline areas inside the silicon nitride bulk material, an inhomogeneous trap distribution is possible.

Within those two general types of conduction, multiple individual conduction mechanisms exist. It is essential to know methods of how to distinguish between them, as several can be active and contribute to the net current conduction through the dielectric at the same time. Figure 1.1 gives a short overview over the conduction mechanisms.
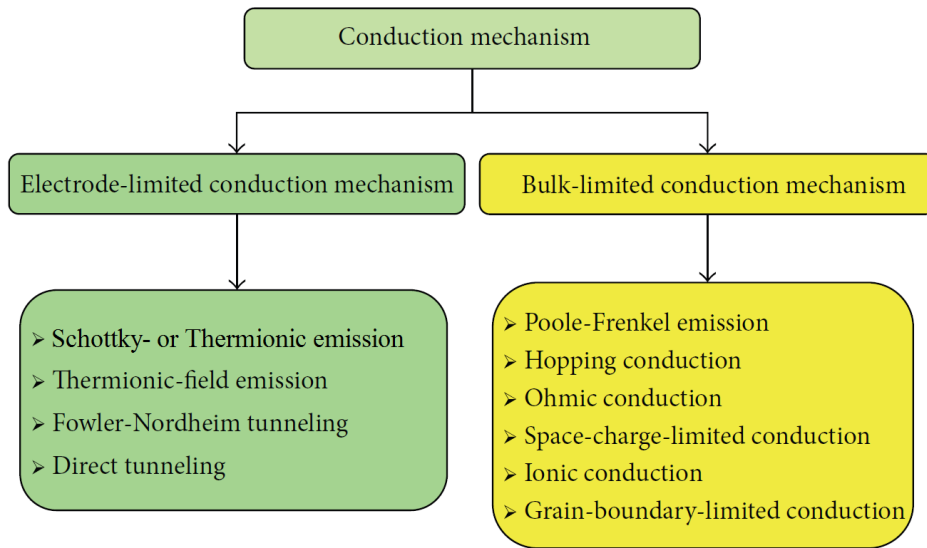
Figure 1.1: Summary of conduction mechanisms in dielectrics within the two general types, electrode-limited and bulk-limited conduction mechanism (after [9]).

To better understand the differences it is informative to put the conduction mechanisms side by side into schematic energy band diagrams (fig. 1.2). It is worthy to point out that there is a difference between Hopping conduction and Poole-Frenkel emission. The latter corresponds to the thermionic effect which helps the charge carriers to overcome the trap barrier. However, in Hopping conduction the tunneling effect is active and the trapped electrons are 'hopping' from one trap site to another, it is a trap-assisted tunneling effect.

As said before, more than just one mechanism can be responsible for the conduction at the same time. In addition to that in general lots of factors affect the electric properties within dielectric materials: temperature, electric field, stress within the film, electrode material, MIM or MIS sample structure, film thickness and film stoichiometry amongst others. Especially for an unknown dielectric it is thus important to test regarding all conduction mechanisms to be considered possible.

Due to the importance of silicon nitride for the semiconductor industry, it has been ex-

(a)

Thermionic emission
(Schottky emission)

$q\phi_B$

Thermionic-field emission

Field emission
(F-N tunneling)

Metal   Insulator   Semiconductor

E_C

E_F
E_V

(a)

(b)

$q\phi_B$

Direct tunneling

Metal   Insulator   Semiconductor

E_C

E_F
E_V

(b)

(c)

$q\phi_T$

Poole-Frenkel emission

Hopping conduction

a

Metal   Insulator   Semiconductor

E_C

E_F
E_V

(c)

(d)

$q\phi_B$

Ohmic conduction

Metal   Insulator   Semiconductor

E_C

E_F
E_V

(d)
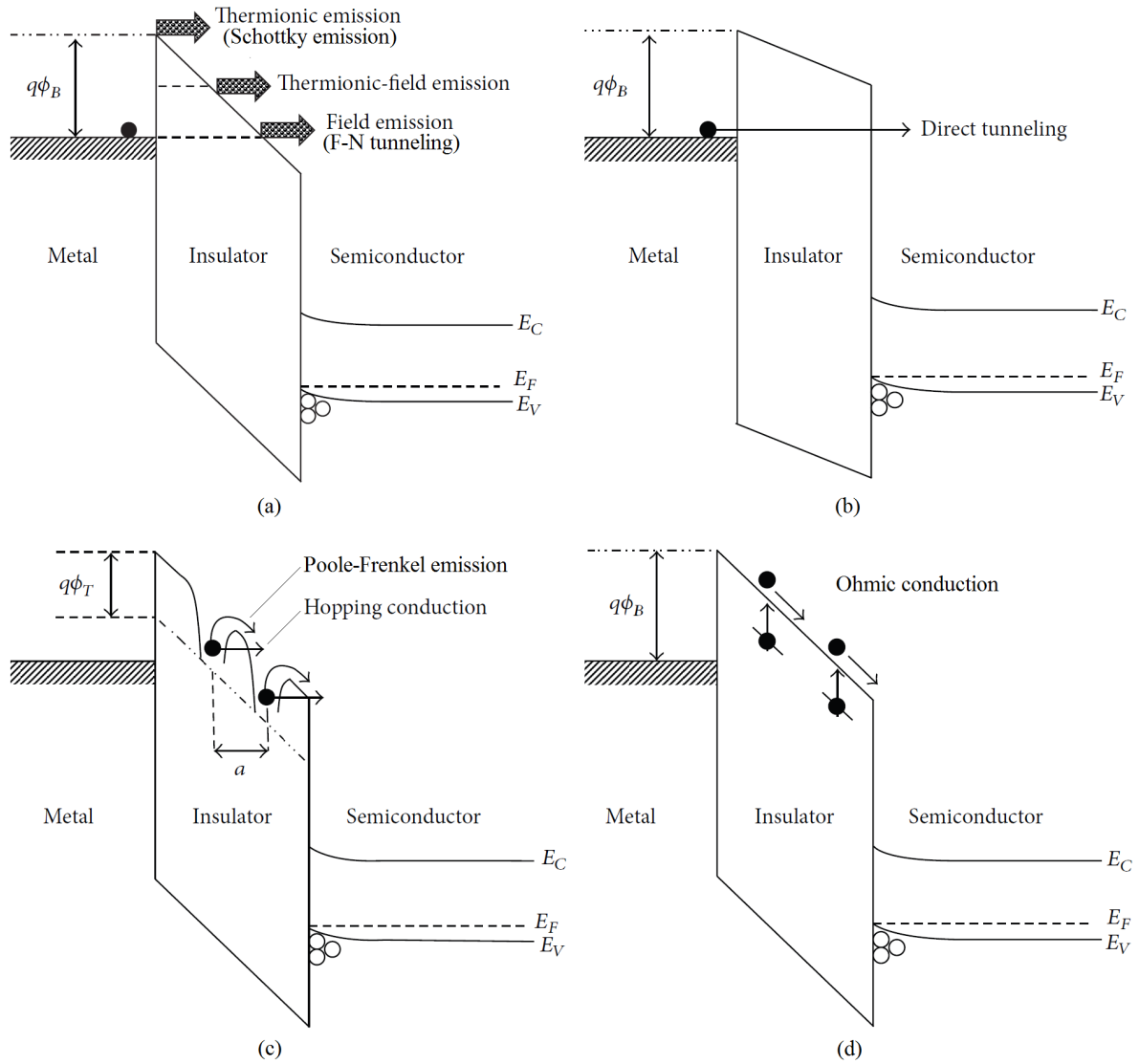
Figure 1.2: Schematic energy band diagrams for comparison of (a) Thermionic emission (Schottky), Thermionic-field emission, Field emission (Fowler-Nordheim tunneling) (b) Direct tunneling (c) Poole-Frenkel emission, Hopping conduction (d) Ohmic conduction.
With $q\phi_B$ $(=\Phi_B)$... barrier height, $q\phi_T$ $(=\Phi_T)$... trap height, a... mean hopping distance, $E_{C/V}$... energy level of conduction/valence band, E_F... Fermi energy (after [9]).

tensively studied in the past and numerous reports are available. Nevertheless as CVD reactors have improved since then, it is advisable to see how material properties changed. Research suggests, depending on the film thickness, the Poole-Frenkel emission and/or the Fowler-Nordheim tunneling as the dominant conduction mechanisms through silicon nitride[28, 26], hence the emphasis is on these two within this work. They are described in chapter 1.1.5 and 1.1.6.

The characteristic expressions for the other conduction methods can be found in the equations 1.4 - 1.11, which are taken from [9] and where more detailed information can be found. The used variables and constants are further explained in the appendix in section 7.5.

Schottky- or Thermionic emission

When the electrons obtain enough energy by thermal activation, they can overcome the potential barrier at the metal-insulator interface. This thermionic emission, or Schottky emission, is the most often observed conduction mechanism in dielectric films, especially at high temperatures.

$$J_{SE} = A^* T^2 \exp\left[\frac{-q(\phi_B - \sqrt{qE/4\pi\varepsilon_r\varepsilon_0})}{kT}\right] , \tag{1.4}$$

$$A^* = \frac{4\pi q k^2 m^*}{h^3} \tag{1.5}$$

Thermionic-field emission

As the tunneling electrons have an energy between the Fermi level of the metal and the conduction band edge of the metal it takes place intermediately between field emission and Schottky emission as shown in figure 1.2 (a).

$$J_{TFE} = \frac{q^2\sqrt{m}(kT)^{1/2}E}{8\hbar^2\pi^{5/2}} \exp\left(-\frac{q\phi_B}{kT}\right) \exp\left[\frac{\hbar^2 q^2 E^2}{24m(kT)^3}\right] \tag{1.6}$$

Direct tunneling

When the electrons face an energy barrier of the full dielectric thickness, the conduction mechanism is called direct tunneling. In case of Fowler-Nordheim tunneling the electrons only 'see' a triangular barrier.

$$J_{DT} = \frac{q^2}{8\pi h\varepsilon\phi_B}C(V_G,V,t,\phi_B) \exp\left\{-\frac{8\pi\sqrt{2m^*}(q\phi_B)^{3/2}}{3hq|E|} \cdot \left[1 - \left(1 - \frac{|V|}{\phi_B}\right)^{3/2}\right]\right\} \tag{1.7}$$

Hopping conduction

The hopping conduction corresponds to the tunnel effect and the trapped electrons can 'hop' from one trap site to another. The energy of the charge carrier is lower than the height of the potential barrier between two trapping sites.

$$J_{HC} = qaN_c\nu \, \exp\left[\frac{qaE}{kT} - \frac{E_a}{kT}\right] \tag{1.8}$$

Ohmic conduction

Due to thermal excitation, mobile electrons can move into the conduction band and holes into the valence band, respectively. In dielectric materials the band gap is large and thus the number of excited charge carriers very small but not zero.

$$J_{OC} = \sigma E = nq\mu E \, , \qquad n = N_C \, \exp\left[\frac{-(E_C - E_F)}{kT}\right] \tag{1.9}$$

Ionic conduction

In an applied electric field ions may move as lattice defects exist in dielectric films. When the external field influences the defect energy level it is possible that the ions overcome a potential barrier and jump from one defect site to another.

$$J_{IC} = J_0 \, \exp\left[-\left(\frac{q\phi_B}{kT} - \frac{Eqd}{2kT}\right)\right] \tag{1.10}$$

Grain-boundary-limited (GBL) conduction

A grain boundary potential energy barrier ($\mathbf{\Phi}_B$) characterizes the GBL conduction. This is because in a polycrystalline dielectric material the resistivity of the grain boundaries can be much higher than the one of the grains and thus the conduction current is limited by the electrical properties of the grain boundaries.

$$\Phi_B = q\phi_B = \frac{q^2 n_b^2}{2\varepsilon N} \tag{1.11}$$

1.1.5 Fowler-Nordheim Tunneling

In classical physics when an electron reaches a potential barrier with a certain height it will either be able to overcome it, or, when the electron's energy is too low, it will be deflected. However, according to quantum mechanics there is also a probability that the electron can penetrate the barrier directly as long as the barrier is thin enough. Electrons can thus also

break through high barriers because of the tunneling effect. For conduction mechanisms through dielectrics with a triangular barrier this behavior is called field emission or Fowler-Nordheim (FN) tunneling. If a trapezoidal barrier is tunneled through, then it is called direct tunneling. A schematic energy band diagram for FN tunneling is shown in figure 1.3.

The FN tunneling current density can be expressed as[12]

$$J_{FN} = \frac{q^3 \; m_{eff}}{8 \; \pi \; h \; m_{diel} \; q \; \phi_B} \; E^2 \cdot \exp\left[-\frac{4 \; \sqrt{2 \; m_{diel} \; (q\phi_B)^3}}{3 \; \hbar \; q \; E}\right] \tag{1.12}$$

Here J_{FN} is the current density attributed to Fowler-Nordheim tunneling, E the electric field across the dielectric, q the elementary (electronic) charge, h $(=2\pi\hbar)$ is Planck's constant and $q\phi_B (\equiv \Phi_B)$ the barrier height. For the mass of the electron it has to be distinguished between the effective electron mass in the electrode m_{eff} and the effective electron mass in the dielectric m_{diel}.
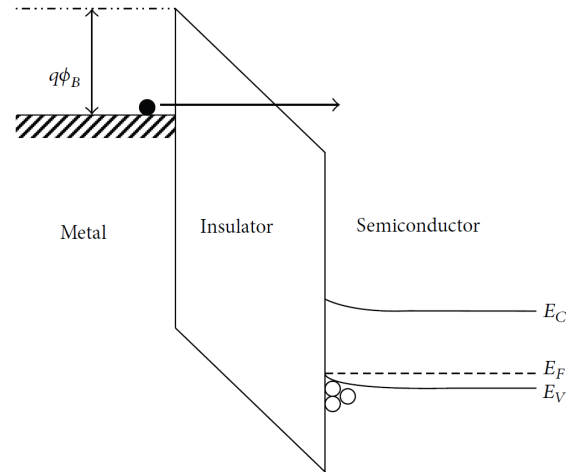
Figure 1.3: Schematic energy band diagram of Fowler-Nordheim Tunneling in a MIS structure[9].

A method to identify FN tunneling is to plot $ln(J/E^2)$ versus $1/E$. When the measured data can be fitted linearly in the described way of plotting, the theory of FN tunneling can be applied to the dielectric.

Then, with known value for the slope of the linear fit, it is also possible to extract the barrier height Φ_B. Starting from equation 1.12, dividing it by E^2 and applying the logarithm yields:

$$\underbrace{ln\left(\frac{J_{FN}}{E^2}\right)}_{y} = \underbrace{ln\left(\frac{q^3 \; m_{eff}}{8 \; \pi \; h \; m_{diel} \; q \; \phi_B}\right)}_{d} - \underbrace{\frac{4 \; \sqrt{2 \; m_{diel} \; (q\phi_B)^3}}{3 \; \hbar \; q}}_{s} \cdot \underbrace{\frac{1}{E}}_{x} \tag{1.13}$$

Equation 1.13 can be interpreted as a linear equation which is given in the slope-intercept

form, where s is the slope and d the value of the intercept:

$$y = s \cdot x + d \tag{1.14}$$

If the effective electron mass in the dielectric m_{diel} is known, the barrier height can be extracted by rearranging the term for the slope:

$$s = -\frac{4\sqrt{2\,m_{diel}\,(q\phi_B)^3}}{3\,\hbar\,q} \,\,\widehat{=}\,\, -\frac{4\sqrt{2\,m_{diel}\,\Phi_B^3}}{3\,\hbar\,q} \qquad \left|\cdot(-\frac{3\hbar q}{4})\right. \tag{1.15}$$

$$-\frac{3\,\hbar\,q\,s}{4} = \sqrt{2\,m_{diel}\,\Phi_B^3} \qquad \left|\,\hat{}\,2\,;\,\cdot\frac{1}{2m_{diel}}\,;\,\sqrt[3]{}\right. \tag{1.16}$$

$$\longrightarrow \Phi_B = \sqrt[3]{\frac{9\,\hbar^2\,q^2\,s^2}{32\,m_{diel}}} \tag{1.17}$$

Experimental values for the effective mass of electrons and holes in amorphous silicon nitride lie in the range of $m_e^* \approx m_h^* \approx (0.4 - 0.5)m_e$, according to [29].

Once Φ_B is known, the effective electron mass in the electrode can be calculated from the term 'd' for the intercept with the y-axis.

When the current-voltage characteristics of the device are measured at very low temperature, the thermionic emission is suppressed and the tunneling current can be extracted[9].

1.1.6 Poole-Frenkel Emission

Unlike the FN tunneling, the Poole-Frenkel (PF) emission belongs to the bulk limited conduction mechanisms. Electrons located in traps, due to a Coulombic attraction potential, are thermally excited and can reach the conduction band of the dielectric. As this procedure is similar to the Schottky emission, the P-F emission is sometimes also called the internal Schottky emission.

Due to an applied electric field across the dielectric, the barrier height of the trap, in which the electrons are located, is reduced. Hence the probability that a thermally excited electron can escape the trap and reach the conduction band rises. In short, the PF emission is a field-assisted thermal de-trapping of a carrier from the bulk into the conduction band[8]. A schematic energy band diagram for PF emission is shown in figure 1.4.

According to the PF emission theory the current density for a Coulombic attraction trap

potential can be written as

$$J_{PF} = q \; \mu \; N_C \; E \cdot \exp\left(\frac{-q\left(\phi_T - \sqrt{\frac{q\,E}{\pi\,\varepsilon_d\,\varepsilon_0}}\right)}{k_B\,T}\right) \tag{1.18}$$

The μ is the electronic drift mobility, N_C the density of states in the conduction band, $q\phi_T$ ($=\Phi_T$) the trap energy level, k_B is Boltzmann's constant, T the absolute Temperature, ε_d is the dynamic (high frequency) relative permittivity (i.e., the dynamic dielectric constant) and ε_0 the vacuum permittivity.
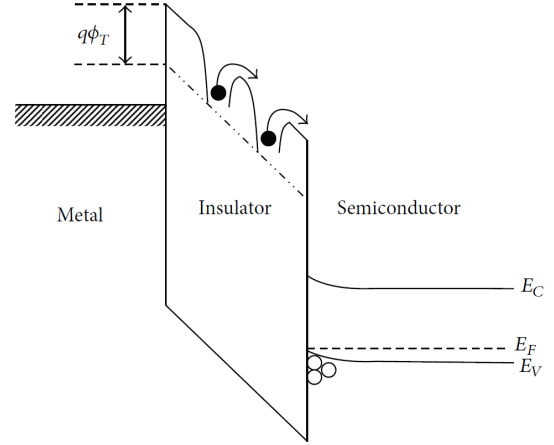
Figure 1.4: Schematic energy band diagram of Poole-Frenkel Emission in a MIS structure[9].

Like for the FN tunneling there is a graphic approach to test whether or not PF emission is present. When a plot of $ln(J/E)$ versus $E^{1/2}$ shows a linear behavior, the PF theory is valid and parameters can be extracted. The calculation is similar to the one from FN tunneling. Equation 1.18 divided by E and logarithmized yielding:

$$ln\left(\frac{J_{PF}}{E}\right) = ln(q\,\mu\,N_C) + \left(\frac{-q\left(\phi_T - \sqrt{\frac{q\,E}{\pi\,\varepsilon_d\,\varepsilon_0}}\right)}{k_B\,T}\right) \tag{1.19}$$

$$\underbrace{ln\left(\frac{J_{PF}}{E}\right)}_{y} = \underbrace{ln(q\,\mu\,N_C) - \frac{q\,\phi_T}{k_B\,T}}_{d} + \underbrace{\frac{\sqrt{\frac{q^3}{\pi\,\varepsilon_d\,\varepsilon_0}}}{k_B\,T}}_{s} \cdot \underbrace{\sqrt{E}}_{x} \tag{1.20}$$

Rearranging the term of the slope allows the calculation of the dynamic relative permittivity ε_d:

$$\longrightarrow \varepsilon_d = \frac{q^3}{s^2\,k_B^2\,T^2\,\pi\varepsilon_0} \tag{1.21}$$

To be able to extract the trap depth Φ_T (or the electron drift mobility μ) from the

interception term, the value for N_C needs to be known.

$$d \quad = \quad ln(q \ \mu \ N_C) - \frac{q \ \phi_T}{k_B \ T} \quad \hat{=} \quad ln(q \ \mu \ N_C) - \frac{\Phi_T}{k_B \ T} \tag{1.22}$$

$$\longrightarrow \Phi_T \quad = \quad (ln(q \ \mu \ N_C) - d) \cdot k_B \ T \tag{1.23}$$

The variables are explained in connection with equation 1.18 earlier.

Another way to extract the depth of the trap is by using the Arrhenius plot. In this case $ln(J_{PF}/E)$ versus $1/T$ is plotted, and again the slope of the fitted line is needed for the calculation. Starting point is a reshaped equation 1.20.

$$\underbrace{ln\left(\frac{J_{PF}}{E}\right)}_{y} \quad = \quad \underbrace{ln(q \ \mu \ N_C)}_{d} + \underbrace{\left(-\frac{q \ \phi_T}{k_B} + \frac{q\sqrt{\frac{q \ E}{\pi \ \varepsilon_d \ \varepsilon_0}}}{k_B}\right)}_{s} \cdot \underbrace{\frac{1}{T}}_{x} \tag{1.24}$$

$$s \quad = \quad -\frac{q \ \phi_T}{k_B} + q\sqrt{\frac{q \ E}{\pi \ \varepsilon_d \ \varepsilon_0}} \cdot \frac{1}{k_B} \quad \left| \ \cdot k_B; \ \cdot\frac{1}{q}; \ \ldots \right. \tag{1.25}$$

$$\longrightarrow \phi_T \quad = \quad -\frac{s \ k_B}{q} + \sqrt{\frac{q \ E}{\pi \ \varepsilon_d \ \varepsilon_0}} \tag{1.26}$$

The relative permittivity is in general a complex-valued, dimensionless value, which is dependent on the frequency.

$$\varepsilon_r(\omega) = \varepsilon_r'(\omega) + i\varepsilon_r''(\omega) \tag{1.27}$$

It is worthy of note that for nonferromagnetic materials, where the relative permeability is approximately 1 ($\mu_r \approx 1$), the real and the imaginary part of the square root of the dynamic (high frequency) relative permittivity is the complex refractive index $\mathbf{n}$[23, 31, 3, 15].

$$\sqrt{\varepsilon_r} = \sqrt{\varepsilon_r' + i\varepsilon_r''} = \mathbf{n} = n + ik \tag{1.28}$$

Here n is the index of refraction and k the extinction coefficient. That this formula is valid is based on the fact that only the electrons are mobile enough to follow a forced change of direction at high frequencies ($>10^{15}$ Hz).

The frequency dependent relative permittivity of water with its real and imaginary part is shown in figure 1.5. For clarity ε_r' is plotted on a log-scale. According to formula 1.28 it is also possible to show the change of the optical properties of silicon nitride in terms of refractive index and extinction coefficient.

The electrical current in formula 1.18 refers to electrons which are first trapped, but then manage to escape due to the field-lowering PF effect. The de-trapping happens so fast, at such a high frequency, that the relation between electric high frequency relative

permittivity and optical refractive index is valid.
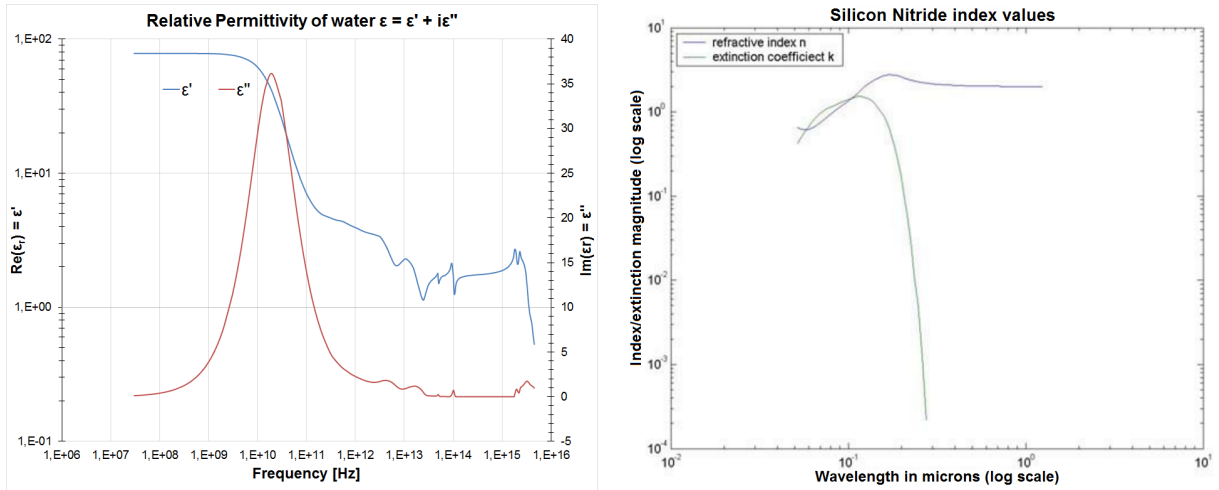
Figure 1.5: Dielectric response of water depending on the frequency (left)[1] and optical properties of silicon nitride (right)[2]

1.1.7 Dangling Bonds in Silicon Nitride

The dominant trap in silicon-rich a-SiN$_x$:H$_y$ is the Si dangling bond, termed the **K** center, while the other 3 bonds of silicon are formed with nitrogen (N$_3 \equiv$ **Si·**). Three charge states are known as K$^+$ (N$_3 \equiv$ **Si$^+$**), K^0 (N$_3 \equiv$ **Si·**) and K$^-$ (N$_3 \equiv$ **Si$^-$**).

Either holes or electrons can be trapped by such an Si dangling bond. In stoichiometric and nitrogen-rich a-SiN$_x$:H$_y$ the K^0 center is metastable. Furthermore also the amount of Si dangling bonds is greatly reduced when nitrogen-rich silicon nitrogen is deposited. Then the dominant residual traps are hole traps[20, 40].

Hydrogen is supposed to reduce the amount of dangling bonds by connecting to either silicon or nitrogen and hence forming Si-H and N-H, respectively. Furthermore nitrogen-rich films are reported to have less charge trapping problems than silicon-rich films.[20].

An exposure to ultraviolet (UV) illumination can irreversible annihilate the K^0 center, supposedly as hydrogen interacts and forms a Si-H bond.[41]

1.2 Deposition Methods

The two main methods used by the semiconductor industry for depositing thin films on a substrate such as a silicon wafer are physical vapor deposition (PVD) the chemical vapor deposition (CVD).

---

[1]Handbook of Optical Constants of Solids II, Edward D. Palik, Academic Press, London, 1991
[2]Handbook of Optical Constants of Solids, Edward D. Palik

1.2.1 Physical Vapor Deposition (PVD)

PVD stands for various vacuum coating techniques which deposit thin films onto a surface by purely physical means. This means that the vaporized form of the desired material condenses on the surface of the sample without any chemical reaction.

The **sputter deposition** plays an important role for thin film depositions among the PVD variants.

Ions from a sputtering gas (e.g. from argon) are accelerated towards a target and the kinetic energy is high enough to knock atoms out of the target. These free atoms then spread out with a moderate energy distribution and impact on the substrate on their own and cause deposition. To ensure that the atoms can reach the substrate without collisions with the sputtering gas, the pressure needs to be low enough that the mean free path is equal, or higher, than the distance from target to the substrate.

The adhesion of the so deposited film is typically very good and even materials with a high melting point, where other evaporation methods are difficult or impossible, can easily be sputter-deposited. The composition of the films is close to that of the source material. Another benefit is that no elevated temperatures are needed and sensitive substrates can be coated.

1.2.2 Chemical Vapor Deposition (CVD)

CVD on the contrary is a chemical process. The surface is exposed to one or more volatile precursors, which then react and decompose and grow the desired film on the substrate. By changing the deposition time, the thickness of the film can be modified. A variety of techniques belong to the group of CVDs and the classification is either done by pressure or by stimulation of the chemical reactions[14].

Especially **Low Pressure CVD (LPCVD)** and **Plasma-Enhanced CVD (PECVD)** are used as methods for producing silicon nitride layers onto silicon wafers[20, 28, 23, 1, 5].

LPCVD

The Low Pressure CVD is, as the name suggests, a process that takes place at sub-atmospheric pressures (1 - 10 mtorr)[25]. This low pressure environment reduces unwanted gas-phase reactions, and also a better uniformity of the layer can be expected across the wafer. However, the deposition rate is rather low compared to other deposition techniques. To start the chemical reaction between the process gases and the surface, high temperatures (around 800 °C) are needed. Especially for multilayer structures, which include materials with a low melting point, e.g., aluminium, this is a serious downside.

PECVD

A way to reduce high substrate temperatures is to use the Plasma-Enhanced CVD. To create a plasma, a gas with a significant percentage of ionized atoms or molecules, a RF frequency is applied between two electrodes, between which the precursors are flowing. As the electrons are very light compared to atoms or molecules, the energy exchange is not efficient. This is important because now the electrons can be kept at high equivalent temperatures inside the RF frequency or the DC discharge and deliver several electronvolts of energy upon impact while the comparable big atoms remain at the ambient temperature. In this work an industrial standard RF generator at 13.56 MHz was used for the plasma creation.

The ions and radicals created in the plasma then spread inside the deposition chamber and also adhere on the substrate surface. They are able to rearrange themselves on the surface until they meet other reaction partners and the chemical deposition reaction starts. Another effect of the plasma is that it is electrically positively charged in respect to the environment. This is again because of the agility of the electrons, which can leave a site quickly, while the heavier and positively charged ions in the plasma are still present. This potential between plasma and a material in contact with it occurs across a thin sheath region. An ion entering that region feels an electrostatic force, which guides the ion to the wafer surface.

Compared to LPCVD, PECVD yields a higher deposition rate with a still good uniformity of the layer. Due to the higher deposition rate usually also more hydrogen gets incorporated into the deposited film, if hydrogen is a part of the precursors. The pressure in PECVD processes typically ranges from a few millitorr up to a few torr.

1.3 Deposition of Silicon Nitride

1.3.1 Substrate Wafers

Silicon wafers are used as substrate material for all depositions. The ones used within this thesis are produced with the Czochralski process and the diameters are either 6 inch (150 mm), or 8 inch (200 mm). It is also possible to use wafers with other sizes, but as not all tools can work with all wafer sizes, this determines the choice of substrates. For the characterization of the so called CuNit 6 inch wafers were selected, due to the geometry of the deposition chamber. For all other characterizations 8 inch wafers were used.

Besides the diameter, the wafers can also vary in other parameters, such as thickness, doping or crystal orientation. All wafers had polished surfaces.

M118 - 8 inch, monitor wafers

When a process is monitored, the so-called M118 monitor wafers are used.

M118 monitor wafer		
Diameter:	200	mm
Production process:	Czochralski	
Crystal orientation:	<100>	
Doping with:	Boron	
Type:	P	
Resistivity:	$1.000 - 1000.000$	Ω cm
Thickness:	$700.00 - 750.00$	μm

Table 1.1: Specifications of the M118 monitor wafers.

The thickness of the native oxide of new monitor wafers is less than $2\,\text{nm}$. If those wafers, however, are stored for some time, a chemical surface clean prior to the usage is recommended. For the characterization of the films within this work always fresh material is used.

C037 - 6 inch, polished wafers

For the experiments on 6 inch tools the C037 wafers are used as monitor wafers. Their specifications are similar to those from the M118 wafers:

C037 polished wafers		
Diameter:	150	mm
Production process:	Czochralski	
Crystal orientation:	<100>	
Doping with:	Boron	
Type:	P	
Resistivity:	$1.000 - 1000.000$	Ω cm
Thickness:	$650.00 - 700.00$	μm

Table 1.2: Specifications of the C037 polished wafers.

P082 – 8 inch, highly doped wafers

As obvious from the specs of the M118 and C037 wafers in table 1.1 and 1.2, those wafers do not have good electrical conducting features. For the electrical characterization of the dielectrics on the point probe station, the chuck acts as bottom contact for the wafer. To ensure a good electrical contact, the P082 wafers are the substrate wafers for this purpose. Their specs can be found in table 1.3:

	P082 wafer	
Diameter:	200	mm
Production process:	Czochralski	
Crystal orientation:	<100>	
Doping with:	Antimony	
Type:	N+	
Resistivity:	0.008 − 0.030	Ω cm
Thickness:	710.00 − 740.00	μm

Table 1.3: Specifications of the P082 polished wafers which were used for the electrical characterization.

Doping materials

The process of intentionally inducing impurities into an extremely pure material is called doping. Main purpose of this is to change the electrical properties and customize it for the intended purpose. Each silicon atom inside a silicon crystal has 4 valence electrons. As long as only Si atoms are in the lattice, the overall charge is zero. When Boron, which only has 3 valence electrons, takes the place of a silicon atom the overall charge will be positive because of the missing electron. Then the material is said to be p-doped and boron is the acceptor.

Antimony on the other hand has 5 valence electrons and thus acts as donator, it inserts one additional electron. Because of this the silicon is then n-doped.[36, 25]

1.3.2 Design of a PECVD Reactor

Generally many different CVD reactor designs are known but in this thesis the CVD systems Producer® and Precision 5000® from Applied Materials® are used. It is convenient to start with the P5000 (Precision 5000), which is the older platform, and then step up to the Producer, as both are working with the same principles and just differ in technical details.

Wafers to be coated are stored in cassettes with 25 wafers inside each of them. Such a cassette is placed onto the loadport and a recipe of the desired process is selected. Then an automatic handler first places the wafers inside a storage elevator before placing them inside the deposition chamber. According to the recipe the heater brings the wafer up to temperature while the valves and flow controllers of the gases are opened to establish a certain flow through the chamber. A pump and a control throttle valve adjust the pressure inside the chamber and once all parameters are okay, the RF generator initiates the plasma. After completed deposition, the handler places the wafer back into the rack while the chamber undergoes a cleaning step. This is necessary to maintain a good wafer-to-wafer uniformity, because deposit can be found everywhere inside the chamber and thus

influence the deposition onto the next wafer if not removed properly.
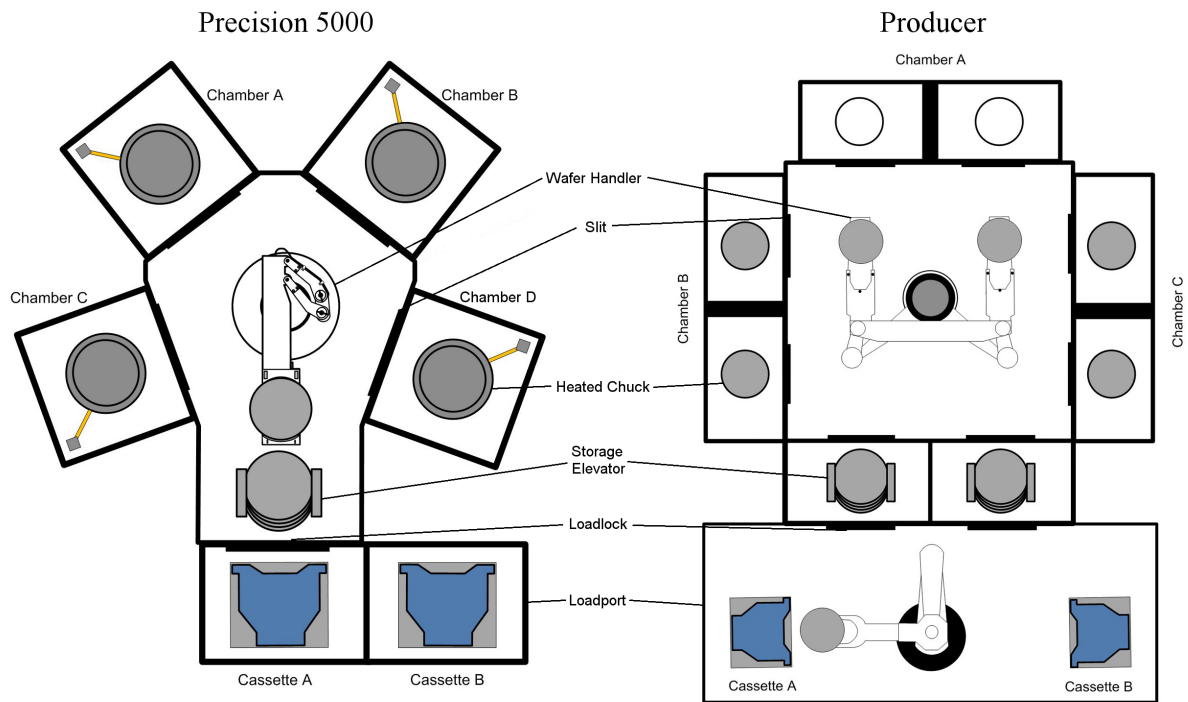
Figure 1.6: Schematic layout of the P5000 and the Producer CVD systems.

Figure 1.6 shows a schematic layout of the CVD systems used for this thesis. The individual parts shall be explained a bit more detailed based on the P5000 and differences compared to the Producer shall be pointed out.

Loadport

Depending on the setup either 6 or 8 inch wafers can be processed in the machine. For a better efficiency it is possible to place two cassettes inside the loadport. When the first cassette is fully processed, the complete loadport moves and the handler picks up wafers from the second cassette.

In the Producer the cassettes are placed further away from each other and a secondary handler transports the wafers into the storage elevator.

Handler

Biggest obvious difference between the P5000 and the Producer system is that the Producer can handle 2 wafers at once, while the P5000 handles the wafers one-by-one. This makes the Producer a more efficient tool for production, hence the name.

Storage Elevator and Buffer Chamber

After the wafers are placed inside the storage elevator by the handler, a loadlock closes and a pump evacuates the atmosphere in the complete handling area, which is called the buffer chamber. The pressure inside this buffer chamber is higher than inside the deposition chamber. This prevents a contamination of the buffer chamber and the wafer during loading/unloading with deposition residue. Once the deposition is done the wafers are stored again in the storage elevator for cooling down from process temperature before they are moved back into their racks.

Deposition Chamber

The wafer enters the the deposition chamber through a small slit valve located at the side, and is then placed down from the handler onto the chuck, which also centers the wafer. Then a lock closes the slit towards the buffer chamber. At the very top of the chamber, clean- and deposition gases are inserted but before they can reach the wafer they need to pass the gas-distribution plate, which ensures uniform gas flow all over the wafer. This steel plate is also called showerhead because of its many small holes. The RF signal for the plasma creation is applied to it. Together with the wafer on the chuck right underneath which is put to ground potential, they form the electrodes for the electrical circuit.

Figure 1.7: Schematic setup of a PECVD deposition chamber. Moving the heater (chuck) downwards changes the electrode spacing. Clean and deposition gases are separated.
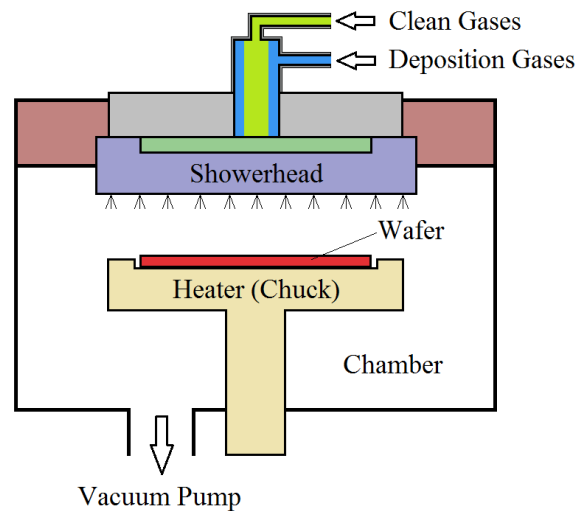
It is crucial that the spacing between showerhead and chuck can be changed, as this modifies plasma parameters which in turn drastically change the properties of the deposited film. All other parts inside the chamber are made of insulating material, because of electric insulation purposes. An exit at the bottom of the chamber enables a pump to first stabilize the desired gas flow at a certain pressure, and then remove the by-products of the reaction through the exhaust line. Over the time the inside walls of this exhaust line

are covered by various residues from deposition, which makes it necessary to exchange it on a regular basis. To ensure that there is no residue particle contamination, a permanent flow through the exhaust line is mandatory. This is also the reason why the pressure in the buffer chamber is higher than inside the deposition chamber.

Pump, Gas and Heater

A total of 5 vacuum pumps (Producer: 4) are installed in the CVD system. One for each of the deposition chambers and a smaller one for the buffer chamber. The gases arrive from different storage tanks into one gas box, located behind the system. This box contains the valves and flow controllers. From there 2 separated lines run to each deposition chamber. Separation of clean gases (Ar, CF_4, N_2O, NF_3, O_2) and deposition gases (SiH_4, NH_3, N_2, He, N_2O) eliminates the risk of strongly exothermal gas phase reactions between O_2 and SiH_4. The deposition gases however, are mixed before they pass through the showerhead. Another big difference between the setups of the 2 systems used, beside the wafer handler, is the heating mechanism. A series of lamps is mounted underneath the chuck in the Precision 5000 system. The heat is generated via radiation of the lamps, hence it is a lamp-heated (LH) system. In the newer Producer, the temperature is regulated with a resistance heating inside a ceramic chuck. This newer design is called CxZ by the manufacturer.

Deposition Recipe

In order to run a deposition process, programming is needed. This is done directly on the tool with an integrated software. The recipe contains the commands for the CVD system in order to produce a certain deposition layer onto the substrate. It needs to be distinguished between the part of programming for the handling, which contains information about where to pick up and place the wafers, and the actual deposition recipe. The latter one is build up by multiple steps and it is specific for each film.

Of course the deposition recipes for usage on the Producer system differ from the ones programed for the Precision 5000. Nevertheless the global structure is about the same and similar to the simplified version in figure 1.8.

In the *Setup* step the general gas flow is established and the pressure adjusted. The step time is big enough that the wafer on the susceptor can reach the demanded temperature. In case of the P5000 system, 4 *Dep* (deposition) steps are following, one for each chamber. They contain the information for the actual deposition process. Note that the recipe can change from chamber to chamber, even if structurally identical ones are built into the system. The last is always the *Pump* step where the chamber is purged with nitrogen, while the precursor gases are turned off and the valve towards the vacuum pump is fully

Step, Name		1, Setup	2, Dep	...	5, Dep	6, Pump
Dep. Chamber		All	A	...	D	All
Step time	[s]	20	60	...	59	10
Pressure	[mtorr]	650	650	...	650	/
RF power	[W]	/	200	...	200	/
Temperature	[°C]	400	400	...	400	400
Spacing	[mils]	550	550	...	545	900
SiH4	[sccm]	110	110	...	112	/
NH3	[sccm]	140	140	...	138	/
N2	[sccm]	9000	9000	...	9000	9000

Figure 1.8: Layout for programming a CVD system with important process parameters. Note that some factors can change from deposition chamber to chamber to ensure equal resulting films. Fine tuning of each chamber is necessary.

open. Additionally the susceptor spacing is increased (heater moves down), which gives the handler the needed space to pick up the finished wafer afterwards. The RF generator is only turned on during the deposition steps.

1.4 Measurement Equipment

For the characterization of thin film coatings (e.g., with silicon nitride) a variety of measuring tools exist.

1.4.1 Thickness and Refractive Index

Optical techniques are wide-spread as they provide high quality, rapid measurements and the equipment is relatively cheap. They are also nondestructive, which is a necessity, as the many films are measured several times during a production process[25]. Thickness and refractive index can be measured on the *OptiProbe* by KLA-Tencor (formerly Therma-Wave). Depending on which model is chosen (3000 or 5000 series available) one, or more, measurement techniques can be selected. Within this work mostly the 5240 model was used, which includes following techniques:

- Beam Profile Reflectometer (BPR)

- Beam Profile Ellipsometer (BPE)

- Visible Spectrometer (VS) (500-800 nm)

- Broad Band Spectrometer (BBS) (190-800 nm)

- Absolute Ellipsometer (AE)

- Broad Band Spectroscopic Ellipsometer (SE) (200-800 nm)

A combination of several techniques can improve the measurement, but generally the BPR only is selected, as it yields reliable data, while taking only a short time for the measurement. Although a certain range of wavelengths is involved in the measurement, the software displays the refractive index at a specific wavelength, for most recipes inside the OptiProbe this is at 670 nm.

More information for each of the techniques mentioned above can be found in chapter 10.2 of [25].

1.4.2 Stress

Thin films exhibit internal or residual stress which is present without any externally imposed forces. Too high tensile stress can cause film fracture, too high compressive stress can lead to delamination of the film from the substrate. Thus it is important to characterize the internal stress[25].

This can be done by an semi-automatic wafer geometry measuring instrument, within this work a tool from the *MX 20x* series from E+H Metrology is used. It is based on the thin film stress formula, sometimes also called Stoney's formula

$$\sigma_f = \frac{E_S \, t_S^2}{6 \, (1 - \nu_S) \, R \, t_f} \tag{1.29}$$

σ_f is the film stress, E_S the Young's modulus of the substrate, ν_S and t_S the Poisson's ratio and the thickness of the substrate,respectively, t_f is the thickness of the film and R the radius of the curvature of the wafer.

To be able to calculate the stress of the film, the thickness and shape of the wafer itself needs to be known before and after deposition to get the values for t_S and t_f. In measuring the bow of the wafer before and after deposition the curvature R can be calculated with known diameter of the sensor ring (D). Values for Young's modulus and Poisson's ratio of the substrate are taken from literature, with respect to the crystal orientation. As mentioned above the stress can either be compressive ($\sigma_f < 0$) or tensile ($\sigma_f > 0$) which can cause destructive consequences if too high.

Figure 1.9 indicates the bow of a wafer for the two types of stress, compressive and tensile. The incorporated hydrogen in plasma deposited $SiN_x{:}H_y$ is believed to be one source of compressive stress ([25],p.750), which, when not too high, results in a resistance against microcracks. Nevertheless, if the compressive stress is too high it is possible that some kind of blisters form and the deposited film delaminates from the substrate. On the contrary, a too high tensile stress causes the film to crack.

Figure 1.9: Sequence of events which lead to (a) residual tensile stress in film; (b) residual compressive stress in film.(Chapter 12.3.2 [25])
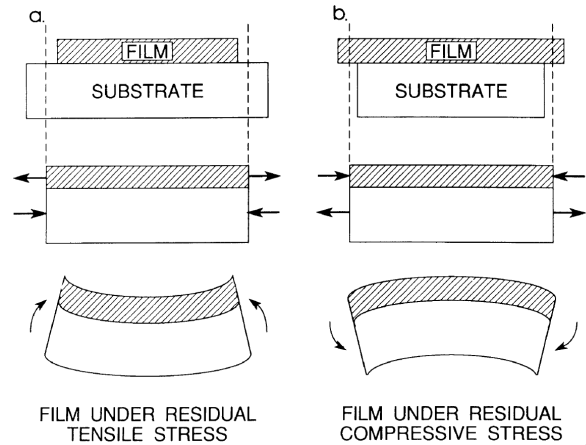
Short example for the calculation of stress

For the calculation of the internal stress by measuring the wafer bow it is convenient to use the wafer delta bow b instead of the radius of curvature R.
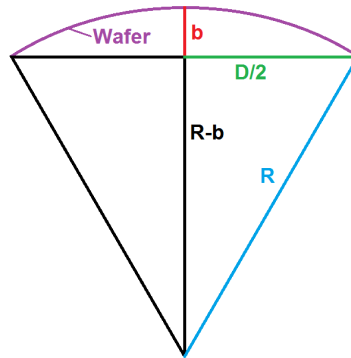
Figure 1.10: Sketch for the calculation of the film stress by measuring the wafer bow. R...radius of curvature, b...delta bow, D...diameter of the sensor ring. $R<0$ and $b>0$ by definition.

From figure 1.10 it is obvious that b can be expressed in terms of R and D by using the Pythagorean theorem.

$$
\begin{aligned}
R^2 &= (R-b)^2 + \left(\frac{D}{2}\right)^2 = R^2 - 2Rb + b^2 + \frac{D^2}{4} \\
2Rb &= b^2 + \frac{D^2}{4} \qquad \left|\text{with } b << \frac{D}{2}\right. \\
\longrightarrow b &= \frac{D^2}{8R}
\end{aligned}
$$

But as the standard sign conventions have b and R with an opposite sign, so for figure

1.10 $b>0$ and R<0, the term for b reads:

$$b = -\frac{D^2}{8R}$$

with D, the diameter of the outer sensor ring, which was 169 mm in case of the used tool. The value for the Young's modulus divided by 1-Poisson's ratio for an 8 inch (200 mm) <100> silicon wafer is

$$\frac{E_S}{1 - \nu_S} = 180.5\,\text{GPa}$$

Insertion into equation 1.29 yields a formula for the calculation of the internal stress of a film deposited on a standard 8 inch <100> silicon wafer. However, the thickness of the film and the substrate, respectively, have to be known.

$$\sigma_f = -7.11x10^{-6}\ t_S^2\ \frac{b}{t_f}$$

1.4.3 Roughness

A *JVX7300L* from Jordan Valley is used for X-ray reflectivity (XRR) measurements on 6 or 8 inch wafers. Similarly to the loadports of the CVD equipment described above, a full cassette of wafers can be placed onto the tool. It picks, measures and returns wafers fully automatic, according to the selected program.

The basic principle is that a beam of X-rays is directed onto the sample surface and the reflected part is then detected. When the angle of incidence is changed, the intensity of the detected beam changes as well. From the analysis of such an angle versus intensity graph, not only the roughness of the surface, but also the film thickness and roughness of the interlayer (in multilayer structures) is possible. This analysis is done by an internal software.

Another possibility to investigate the surface of a material is by using an Atomic Force Microscope (AFM). It yields a high resolution and belongs to the group of scanning probe microscopes. A cantilever with a sharp tip is moved across the sample, line by line. There are three AFM operating modes for the creation of images. They are all related to the behavior of the tip.

- contact or constant height mode

- tapping or vibrating mode

- non-contact mode

The similarity between the modes is that they all use a beam deflection detection. A laser beam is pointed at the cantilever and the reflection is detected by a photodiode. As the

cantilever is displaced due to the interaction with the sample surface, the photodiode too records another point of impact of the laser beam. Additional information can be found in chapter 10.3 of [25].

Information about factors that influence the measurements with XRR and AFM can be found in section 2.6.1.

1.4.4 Electrical Properties

For the recording of voltage-current (U-I) curves of dielectrics, a test structure on the wafer is necessary. The structure used in this work is described in detail in section 4.1. It can either be a MIM (Metal Insulator Metal) or a MIS (Metal Insulator Semiconductor) structure. Then the wafer is investigated using a point probe station. In general the wafer is placed onto a thermal chuck which, besides being heated and cooled, can also be moved in all 3 directions. Additionally an optical microscope is located above the chuck, which is of great help when small structures on the wafer need to be contacted. A 3-way micropositioner presses the measurement needle against the wafer surface to establish an electrical contact. It is crucial to do this carefully as with too much pressure the sample film can be damaged easily. Depending on the setup of the probe station, multiple needles can be used simultaneously. Each needle is connected to a parameter analyzer, which then applies the desired voltage and measures the current. A black box is built around the probe station which needs to be fully closed before any voltage can be applied. This is not only important for safety reasons, but also the excitation of electrons by light is suppressed.

For this thesis one parameter analyzer and three separate source monitoring units (SMUs) were used

- Agilent 4156C Precision Parameter Analyzer $2\,\mu$V - 100 V 1 fA - 100 mA
- Keithley 2400 Source Meter 200 mV - 200 V 1 μA - 1 A
- Agilent A41420A Source/Monitor Unit 40 μV - 200 V 20 fA - 1 A
- Hewlett Packard HP41420A Source/Monitor Unit 40 μV - 200 V 20 fA - 1 A

The measurement process is controlled by an computer connected to the parameter analyzers, and the recorded data is saved for further analyses.

Furthermore the *CVmap 3093-AC* from Four Dimensions is used. This capacitance-voltage (C-V) measurement tool is common to determine semiconductor parameters on wafers. For the actual measurement an DC bias is overlayed by a small AC frequency, which makes the total process nontrivial. The wafer is placed on a metal chuck, which

serves as electrical contact to the substrate. Then the wafer is flipped over and with the deposited surface first lowered onto a small pipe. This pipe is filled with mercury and thus generates a round electrical contact with known diameter. The setup then is related to the shape of a parallel-plate capacitor. With known thickness of the film, the relative dielectric constant at various frequencies (ε_r) can directly be displayed, rearranging the formula:

$$C = A\left(\frac{\varepsilon_r}{d}\right) \tag{1.30}$$

With C the capacitance, A the area of the capacitor, ε_r the dielectric constant of the insulator and d the separation of the two plates. Further information about this technique is provided by the manufacturer in [33].

1.4.5 Hydrogen Content

A frequently used method to analyze the amount of hydrogen in the deposited films, which has been suggested in several papers[5, 4, 19], is Fourier Transform Infrared (FTIR) spectroscopy. The *QS-500* from the manufacturer Bio-Rad was the FTIR spectrometer used for the spectra within this work. In case of a transmission measurement a beam of light passes through the sample and a detector records the intensity. According to the name of the spectrometer, light from the IR-region 400 - 4000 cm^{-1} (= 25 - 2.5 μm) is used and the absorption at each wavenumber (wavelength) is recorded.

Substantial amounts of hydrogen inside PECVD silicon nitride layers can be proven with the presence of the Si-H and N-H stretching frequencies at 2160 and 3350 cm^{-1} in the absorption spectrum, respectively. A method to determine the Si-H and N-H content of plasma-deposited silicon nitride was presented by Lanford & Rand[19]. This method is based on the Lambert-Beer law and uses the area underneath the absorption bands along with a calibration factor for the calculation of the H-content.
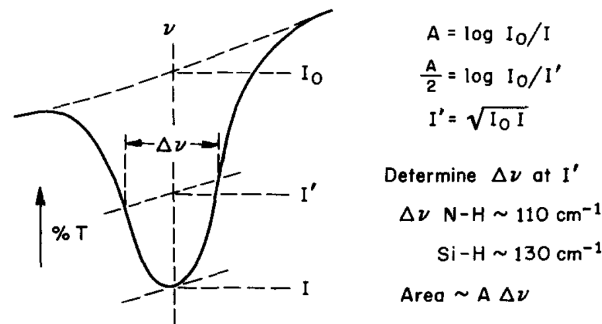
Figure 1.11: Area approximation method for IR absorption bands according to Lanford & Rand. A...absorption, I...intensity with sample, $\Delta \nu$...bandwith at half-absorbance (after [19])

By introducing a function for an effective thickness correction, the accuracy of this method

can be further improved[6]. Instead of the area it is also possible to calculate the hydrogen content from the height/ depth of the peak[32]. This is an further improvement as the CO_2 absorption bands ($2320\,cm^{-1}$) often distort the edge of the Si-H peak, and thus the value of the Si-H content, when using the area approximation method. The tricky part in this method is always to find the right location of the baseline. More details to this can be found in subsection 3.2.

A blank spectrum is recorded prior to a measurement to obtain a background spectrum which pays respect to the properties of the tool itself. It is then used for the calculation of the sample absorption spectrum. A typical film absorption spectrum of PECVD silicon nitride can be seen in figure 1.12.
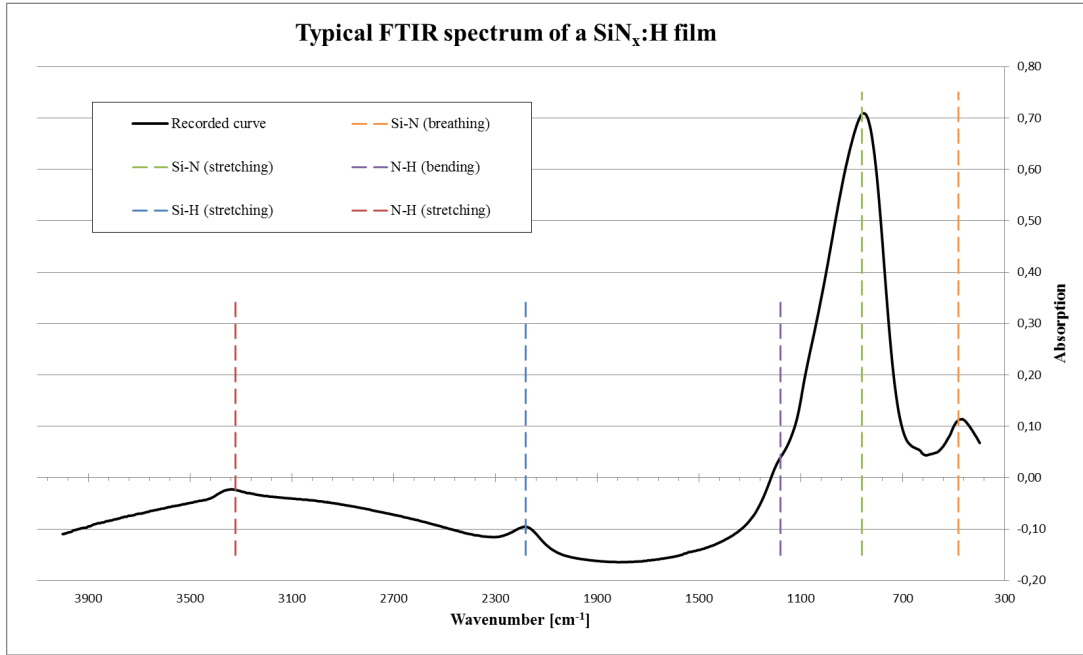
Figure 1.12: Typical sample absorbance spectrum for an $800\,nm$ α-SiN_x:H film. The Si-H and N-H peaks prove the existence of hydrogen.

The Si-H peak is reported to shift to a lower frequency, as the N/Si ratio of the film decreases[18].

When impurities are neglected, only silicon (Si), nitrogen (N) and hydrogen (H) atoms are present inside a PECVD SiN_x film. Once the chemical bond concentrations are known, it is possible to extract the atomic concentrations through the following equations, given by [4]:

$$[\text{Si}] \quad = \quad \tfrac{1}{4} \left([\text{Si-H}] + [\text{Si-N}] + 2[\text{Si-Si}] \right) \tag{1.31}$$

$$[\text{N}] \quad = \quad \tfrac{1}{3} \left([\text{Si-N}] + [\text{N-H}] \right) \tag{1.32}$$

$$[\text{H}] \quad = \quad [\text{Si-H}] + [\text{N-H}] \tag{1.33}$$

Some empirical relations between [Si]/[N]-ratio, [Si-H]/[N-H]-ratio and the refractive index allow the estimation of the stoichiometry, if [Si-H] and [N-H] content is known. Following equations are given by [10].

$$n = 0.70 \cdot \frac{[\text{Si}]}{[\text{N}]} + 1.39 \tag{1.34}$$

$$n = 0.059 \cdot \frac{[\text{Si-H}]}{[\text{N-H}]} + 1.88 \tag{1.35}$$

$$\longrightarrow \frac{[\text{Si}]}{[\text{N}]} = 0.084 \cdot \frac{[\text{Si-H}]}{[\text{N-H}]} + 0.70 \tag{1.36}$$

1.5 Design of Experiments

The measurements for this thesis were carried out inside the Infineon Technologies Austria AG, a semiconductor manufacturing company. That implies that the time for working on a machine is limited, and thus valuable, as the experiments need to be executed side by side with the productive activities, which have priority. A good planning is necessary to get as much information as possible out of a minimum number of experiments. So the design of experiments (DoE) enables the experimenter to use the available resources effectively. The following is a brief introduction and based on reference [17].

1.5.1 DoE process flow

A DoE analyzes a relation between input parameters that can be controlled and modified (factors) and the resulting output parameters (responses). In general the process from start till the end of a project can be divided into 5 phases

1. **Definition** - the problem/task is identified and the involved factors and responses are gathered, if necessary a team is set up

2. **Design** - a regression model is is chosen (e.g., linear model) and an appropriate experimental design is selected

3. **Experiment** - everything is first prepared and then executed, during the experiment the results are documented for later analysis

4. **Analysis** - the results from the experiment are evaluated and variables with the most influence on the outcome are detected, parameters are optimized

5. **Decision** - the model results are compared to the real data and it is decided whether or not confirmation experiments are necessary

1.5.2 Types of Designs

When the problem/task is set (e.g., characterization of a thin film on a Si wafer) the factors are listed apart from the responses. A simple set of factors and responses is given in table 1.4.

Factors	Responses
RF power	Film thickness
Electrode spacing	Refractive index
SiH_4-flow	Stress

Table 1.4: Examples for possible factors and parameters when characterizing a film on a Si wafer.

In the beginning it is unknown which factor influences which response, especially how strong. First a model for the regression is chosen and then a fitting design is selected. A standard type would be for example a linear regression model (2 possible settings for each factor) in combination with a full factorial experimental design.

Short example

Taken table 1.4 in combination with a linear regression model with a full factorial design, it is necessary to perform a minimum of $2^3 = 8$ experiments. This is because each factor is used at 2 different settings and all possible combinations are executed, hence the name full factorial design. Linear full factorial designs are also called 2^k-designs, where k is the number of factors that can be varied.

This yields a plan for the execution of the experiment where 0 denotes a low and 1 a high setting of the respective factor:

Number of experiment	2^3 experimental plan		
	RF power	Electrode spacing	SiH_4-flow
1	0	0	0
2	0	0	1
3	0	1	0
4	0	1	1
5	1	0	0
6	1	0	1
7	1	1	0
8	1	1	1

In a graphic visualization of speaking the settings of the factors can be viewed as corner points and the experimental space within the virtual cube is explored.
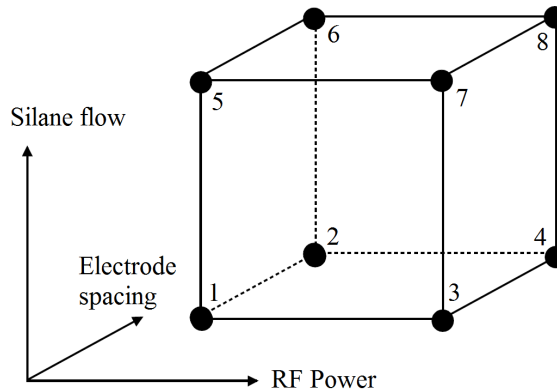
Figure 1.13: Illustration of a full factorial 2^3 experimental plan (after [17]).

According to the short example, the corner points 1,2,3,4 in figure 1.13 would be the experiments 1,3,5,7 of the experimental plan, there is always a low flow of silane. To gain more information about the experimental space, it makes sense to add more points inside the cube. A centerpoint inside the cube for example can be used to confirm or disprove the validity of a linear regression model.

Furthermore it is also necessary to repeat an experiment attributed to a point several times to gain information about the stability of the process itself.

Other Designs and Software

With additional experiments and a full factorial design, it is obvious that the number of required experiments rises quickly as more factors (k) are involved and the complete experimental design becomes uneconomical. A solution to this problem is to select a screening-design first, which identifies the important factors. When the unimportant factors are neglected, the total number of experiments decreases in the following full factorial experimental design. Another possibility is to chose for example a so called D-optimal design. Those are designs where a computer algorithm calculates the points within the space, given a number of maximum doable experiments.

Several software solutions are available on the market which help the experimenter through all phases of the optimization process. *CEDA*, based on Cornerstone by camLine, is one of them and it was used for this thesis.

2 Designed Experiments

The plasma assisted deposition of silicon nitride is a very complex process and it is influenced by lots of factors. So far there is no theoretical model available which could describe that complex system. Wafer uniformity and other film parameters must be obtained from several designed experiments by trial and error, or 'characterization'.[30] The obtained relations between factors (gas flow, etc.) and parameters (intrinsic stress, etc.) aid in the prediction of material properties when an optimization is carried out.

In the context of this work 4 different variations of PECVD a-SiN$_x$:H$_y$ were examined:

1) Std.Nit ...standard silicon nitride as described in various studies
2) LoHN ...a version with low hydrogen content
3) SiN-m ...a mixture of the LoHN and the Std. Nit
4) CuNit ...silicon nitride for deposition onto copper

Comparision between SiN$_x$ variants

The one thing that all variants have in common is that they all use nitrogen (N$_2$) as diluent gas. Further, the SiN-m recipe is close to the one for Std. Nit, both use silane (SiH$_4$) and ammonia (NH$_3$) as precursor gases. In contrary, LoHN and CuNit do not use ammonia during deposition, this helps to keep the incorporated hydrogen content low. The deposition step of LoHN and CuNit is basically the same, but for the latter an additional pre-step is used to chemically reduce the copper surface prior to the SiN$_x$ deposition and ensure good adhesion and prevent coloration of the Cu surface.

To find out which factor influences which film parameter, designed experiments for the silicon nitride films are performed. For the planning and evaluation of those DoEs the software *CEDA*, which is based on Cornerstone, is used. Some differences between the lamp heated (LH) and the resistance heated (CxZ) systems were found.

2.1 SiN-m on Producer (CxZ)

The manufacturer *Applied Materials* released some information about a silicon nitride film with the name 'SiN-m' some time ago. That recipe is designed for the coating of 12

inch (300 mm) wafers on another CVD system than the ones used within this work. The first thing to do was to scale down their published process values to fit for the processing of 8 inch wafers on the Producer system. The target was to obtain a film with an intrinsic stress of about -200 MPa, an index of refraction of 1.9, and a deposition rate as high as possible.

The power of the RF generator could be recalculated easily when considered as power per square millimeter. For the gases silane, ammonia and nitrogen, the total amount of gas flow was reduced to the capabilities of the mass flow controllers inside the Producer. For the beginning the ratio between the gases was kept as in the released recipe. Other parameters, such as pressure, spacing, temperature, were directly inherited. All those values were assumed to be the centerpoint of a full factorial DoE, where the factors SiH_4-flow, NH_3 and RF power can take a high and a low setting. The silane flow was varied from 97 to 137 sccm[1] , nitrogen from 118 to 158 sccm, and RF power from 329 to 419 W.

Number of experiment	SiN-m DoE 1		
	SiH_4-flow	NH_3-flow	RF power
1	x	x	x
2	0	0	0
3	0	0	1
4	0	1	0
5	0	1	1
6	1	0	0
7	1	0	1
8	1	1	0
9	1	1	1

Table 2.1: First DoE for SiN-m on the Producer (CxZ) system for screening purposes in deposition chamber A. x. . . centerpoint, 0. . . low state, 1. . . high state

With the results of this first DoE, CEDA could already make some predictions about factor-parameter-relations. So this first screening DoE was used to create a recipe, where the film parameters already came close to the desired ones. This point was assumed to be the new centerpoint of another, more detailed DoE. A D-optimal design with 21 recipes (42 wafers) provided more information about the SiN-m silicon nitride to be able to refine the regression model in CEDA.

At this point the schematic setup of the Producer system (figure 1.6) shall be mentioned again. The depositions were made inside the deposition chamber A, which offered space for 2 wafers (A1 and A2). This means that with each recipe 2 wafers were coated. Although the recipes were identical for both wafers, slight differences in the measured film properties

---

[1]Abbreviation for: standard cubic centimeters per minute. This counts for standard conditions for temperature (273.15 K) and pressure (101.325 kPa).

were observed.

Now the deviations of the factors around the centerpoint were smaller, and the electrode spacing was added as another factor in the design of the experiment. Silane was varied from 84 to 110 sccm, ammonia from 139 to 181 sccm, RF generator power from 375 to 423 W, and the electrode spacing from 510 to 570 mils[2].

Number of experiment	SiN-m DoE 2			
	SiH$_4$-flow	NH$_3$-flow	RF power	Spacing
1	0	0	0	0
2	1	0	0	0
3	x	1	0	0
4	0	x	x	0
5	0	0	1	0
6	1	0	1	0
7	0	1	1	0
8	1	1	1	0
9	0	1	0	x
10	1	1	0	x
11	0	0	x	x
12	x	x	1	x
13	x	0	0	1
14	0	x	0	1
15	1	x	0	1
16	x	1	x	1
17	0	0	1	1
18	1	0	1	1
19	0	1	1	1
20	1	1	1	1
21	x	x	x	x

Table 2.2: Second DoE for SiN-m on the Producer system to refine the regression model. x...centerpoint, 0...low state, 1...high state

With the additional data the regression model in CEDA could be further improved and a derivation of an adjusted response graph was possible for each deposition chamber. For chamber A1 this is figure 7.1 and for chamber A2 figure 7.2, the confidence level is set to be 0.95. As the measured data did not allow to find a significant connection between ammonia-flow and SiH-content, and electrode spacing and SiH-content, respectively, the corresponding fields in the figures are left blank.

The relative term significance of the regression model is represented in figure 7.3. Here a significance value less than 0.05 is set as a threshold for moving a term into the calculation. For moving a term out the threshold is set to be greater than 0.10, the confidence level is

---

[2]The unit mils is equal to mil, so 1 mils $\equiv$ 1 mil = 1/1000 inch = 0.0254 mm

set to be 0.95.

However, there was still a significant difference between the film properties of the wafers deposited in A1 and A2. Gas flows could just be selected for the whole chamber, that means it was impossible to correct the properties by choosing different flow rates for the two wafers. Hence the correction needed to be done by adjusting factors that affected the two stations independently. In this case different values for RF generator power and electrode spacing were chosen in the final SiN-m recipe for each wafer.

In order to check the quality of the regression model, the software-generated values which should yield the requested film parameters were programmed into a POM (proof of model) recipe. The film parameters of wafers coated with that recipe are listed below.

	Dep. Rate [nm/min]	Unif. [%]	Ref. Ind. [ ]	Intr. Stress [MPa]	Si-H * [cm^{-3}]	N-H * [cm^{-3}]
Chamb. A1	197±12	3.1±0.2	1.899±0.009	-178±27	1.3±0.1	14.0±0.9
Chamb. A2	204±12	3.1±0.2	1.900±0.012	-182±28	1.3±0.1	14.0±0.9

Table 2.3: Film parameters obtained from SiN-m POM (prove of model) recipe. *. . . Factor +1E21 has to be added.

2.1.1 Remarks and Discussion

As the deposition rate is different from A1 to A2 it is obvious, that the time of the deposition step is specific for each wafer in order to guarantee a similar film thickness. Due to the fact that both chambers have the same gas supply, this implies that the deposition can only be stopped by turning off the RF generator power on one side, while still coating the wafer on the other side. So there are still precursor gases flowing through the already finished chamber which are not used. Assuming a total gas flow of 4500 sccm through each chamber at 400 °C and 5 torr, 140 liter of process gases are wasted within 5 seconds.[3]

An in-wafer uniformity, as described in equation 3.1, of ≈3 % is an acceptable, yet not very good result. Including additional factors, such as substrate temperature or N$_2$-flow, into another DoE could further improve this value.

The index of refraction is measured by BPR at 630 nm wavelength on 9 different sites across the wafer, following the 8Z9PKT layout from figure 3.1. The value given above is the average value plus/minus standard deviation from those sites.

For the intrinsic stress an error of 15 % is estimated. This is because the maximum and minimum stress values across the wafer can change rapidly from wafer to wafer, as

---

[3]By using the ideal gas law $pV = nRT$.

especially the RF generator power and the silane flow show an enormous influence on the stress even when just changed a little bit (e.g. fig. 7.1).

2.2 SiN-m on Precision 5000 (LH)

As the results on the Producer were promising, the next step was to transfer the recipe to the Precision 5000 CVD system. In contrast to the Producer, here IR-lamps are used for heating up the wafer and only one wafer is inside the deposition chamber. Nevertheless, the tendencies which factors change which film parameters should be the same, just how much change they cause needed to be determined. Because of this, the recipe for depositing SiN-m on the lamp heated P5000 system was tuned without carrying out another sophisticated DoE.

The settings of the gas flows from the big Producer deposition chamber were adjusted to fit to the smaller ($5600\,cm^3$) P5000 chamber A, the ratios of the involved gases were kept the same. Likewise the values for the other factors. This base-recipe was first varied in one direction from the initial values in terms of silane flow (-5 sccm), RF power (-10 W), and electrode spacing (+20 mils). Due to that slight variations a first estimation of how strong the properties would change was gained. With the help of the SiN-m regression model from the Producer system two more recipes were created, for one of them also the nitrogen flow was reduced. The idea behind this was to raise the percentage of the precursor gases within the total gas flow and thus gain a better deposition uniformity at the edge of the wafers. This approach proved successful, only the intrinsic stress in experiment 6 from table 2.4 was still too compressive ($\approx$ -400 MPa). Due to the known influence matrix of the factors, the intrinsic stress could be shifted to the desired region by changing all influencing factors a little bit in experiments 7 and 8. The values used can be found in table 2.4, the measured film properties in table 2.5.

Number of experiment	SiN-m on Precision 5000				
	SiH_4 [sccm]	RF power [W]	Spacing [mils]	NH_3 [sccm]	N_2 [sccm]
1	43	405	520	72	4093
2	38	405	520	72	4093
3	43	395	520	72	4093
4	43	405	540	72	4093
5	43	390	555	72	4093
6	43	390	555	72	3500
7	45	385	560	70	3500
8	45	385	565	70	3500

Table 2.4: Experiments to establish the SiN-m recipe on the Precision 5000 system with lamp heating.

Exp. No.	Dep. Rate [nm/min]	Unif. [%]	Ref. Ind. [ ]	Avg. Stress [MPa]	Si-H * [cm^{-3}]	N-H * [cm^{-3}]
1	207±17	4.1±0.3	1.906±0.013	-801±121	0.9±0.1	14.9±0.9
2	185±13	3.5±0.2	1.918±0.028	-1049±158	0.8±0.1	15.1±0.9
3	203±18	4.5±0.3	1.901±0.010	-617±93	0.9±0.1	15.0±0.9
4	192±19	4.9±0.4	1.907±0.016	-612±92	0.9±0.1	15.2±0.9
5	193±17	4.4±0.3	1.901±0.006	-434±66	1.2±0.1	14.9±0.9
6	196±17	4.3±0.3	1.901±0.007	-408±62	1.2±0.1	15.2±0.9
7	203±17	4.1±0.3	1.901±0.006	-337±51	1.3±0.1	14.9±0.9
8	206±16	3.9±0.3	1.899±0.007	-209±32	1.3±0.1	14.8±0.9

Table 2.5: Film properties of the SiN-m DoE wafers on the Precision 5000. *...Factor +1E21 has to be added.

The film properties of wafer number 8, so the final result of this series of experiments, were close to the desired ones and well comparable with the films deposited on the Producer system. Due to that the recipe of experiment number 8 was further used as the one SiN-m recipe. The SiN-m wafers for the electrical characterization were coated with this recipe inside the same deposition chamber.

2.2.1 Remarks and Discussion

It is obvious from the results above, that the uniformity of the films from the lamp heated system is worse than the ones from the resistance heated CVD system. A reason for this might be that one (or several) of the lamps from the array did not deliver the same amount of heat than the others.
The LH-films also show a slightly higher concentration of N-H bonds. Reason for this is that in first priority the factors are tuned to yield the desired values of index of refraction and intrinsic stress. By a stepwise reduction of the ammonia flow, this value could also be brought closer to the result from the Producer. Nevertheless the general influences of the factors are behaving like the ones found for SiN-m on the Producer as can be seen in figure 7.4.

2.2.2 Difference CxZ and LH

It is not straight forward to draw a direct comparison between lamp heated and resistance heated chucks as they are installed in different CVD systems. The Producer has, because of the double chambers, a much bigger volume and thus needs higher gas flows than the Precision 5000 with the single chambers. Additionally also the way how the RF frequency is adjusted is different. The Producer has a 'fixed match' system, which uses the generator's fast electronics for the impedance matching to set the desired power level.

A much slower, mechanical 'variable match' is built into the P5000. This means that after the deposition process starts, the desired plasma is faster set up in the Producer system. With some fine tuning it is possible to get the same film properties out of either of the machines, nevertheless the uniformity across the wafer was in all experiments better when the deposition was done in a CxZ chamber.

2.3 LoHN on Producer (CxZ)

The gases involved in the deposition process of LoHN were only SiH_4 and N_2. This caused a lower deposition rate, but also decreased the incorporated hydrogen content. Requirements for LoHN films were an intrinsic stress of about -150$\pm$100 MPa, index of refraction of 1.87$\pm$0.03, and deposition rate as high as possible. This process was already running stably on several lamp heated (LH), 8 inch systems, and thus the influencing matrix was known Infineon internally. From the SiN-m transfer from the CxZ to the LH system it was obvious that the general influencing tendencies of the factors do not change. So the existing influencing matrix could be used to install a LoHN recipe on the Producer system without the need for a big DoE.

The gas flow was rescaled to fit for the big 13000 cm^3 double-wafer deposition chamber A of the Producer, all other settings were directly copied. As this first recipe yielded film properties outside the desired specification limits, especially for the stress, several changes in the recipe had to be made in the experiments 2-7 of table 2.6 to get the desired film properties.

Number of experiment	LoHN on Producer			
	SiH$_4$ [sccm]	N$_2$ [sccm]	RF power [W]	Spacing [mils]
1	237	9050	500/500	580/580
2	235	9050	530/530	580/580
3	235	9050	575/575	580/580
4	225	9050	530/530	580/580
5	235	9050	575/575	570/570
6	225	9050	581/583	580/578
7	225	9050	598/604	585/575

Table 2.6: Experiments to establish the LoHN recipe on the Producer system with resistance heating. The values for the RF generator power and the spacing correspond to the values for chamber A1/A2, the gas flows are valid for the whole deposition chamber.

As can be seen from table 2.6 in the recipes 6 and 7 slightly different values for the RF generator power and the electrode spacing were chosen for the wafers in the A1 and the A2 chamber, respectively. Like already described above for SiN-m on the Producer, there

is just a single gas flow for the whole deposition chamber. In order to correct some offsets of the film parameters, it is necessary to counteract with the factors that only affect the two stations individually.

The obtained film properties from the final LoHN recipe can be found in table 2.7. Again, like for the SiN-m, a slight difference can be noted between the two stations inside the chamber. For the hydrogen content both Si-H and N-H bonds are reduced compared with the SiN-m results.

	Dep. Rate [nm/min]	Unif. [%]	Ref. Ind. [ ]	Intr. Stress [MPa]	Si-H * [cm^{-3}]	N-H * [cm^{-3}]
Chamb. A1	130±9	3.3±0.2	1.874±0.010	-147±22	0.4±0.1	12.9±0.8
Chamb. A2	137±8	2.7±0.1	1.875±0.013	-143±22	0.4±0.1	12.6±0.8

Table 2.7: Film parameters obtained from final LoHN recipe on Producer CVD system. *...Factor +1E21 has to be added.

The corresponding adjusted response graph from CEDA can be found in figure 7.6. For the LoHN films in the electrical characterization, however, the already existing recipe on the lamp heated Precision 5000 system was used.

2.4 CuNit on Precision 5000 (CxZ)

Despite the name, CuNit is not a silicon nitride variant with integrated copper, but the recipe intends to deposit low hydrogen silicon nitride (LoHN) onto a copper coated substrate. The series of designed experiments for CuNit was, contrary to all other DoEs, carried out on a Precision 5000 tool with a 6 inch, resistance heated (CxZ), single-wafer deposition chamber. The requirements for that variant of silicon nitride were equal to the ones for LoHN.

As a stably running version of CuNit was already installed on another 6 inch, but lamp heated system, only a few settings had to be rescaled to fit to the chamber volume. Due to the fact that the deposition step was the same as for LoHN, similar relations between factors and responses were expected. Within the first 3 experiments a variation of N$_2$ and SiH$_4$ was used to find a fitting centerpoint for the following DoE.

Number of experiment	CuNit on Precision 5000			
	SiH$_4$ [sccm]	N$_2$ [sccm]	RF power [W]	Spacing [mils]
1	112	4525	600	580
2	112	4000	600	580
3	99	4000	600	580

Table 2.8: First set of CuNit experiments to find a centerpoint for the following DoE.

As the RF generator power tended to be a significant influencing factor in the previous sets of experiments of SiN-m and LoHN, this value was varied in 5 steps this time. The extra data points were used to find out whether or not a linear regression model was realistic. Silane was changed from 90 to 120 sccm, the spacing from 555 to 595 mils, and the RF power from 560 to 620 W.

Exp. No.	CuNit DoE			Exp. No.	CuNit DoE		
	SiH_4	Spacing	RF power		SiH_4	Spacing	RF power
1	0	0	0	12	0	1	1
2	0	0	0	13	x	1	1
3	0	1	0.75	14	1	0	1
4	0	1	0	15	1	x	1
5	x	x	0	16	1	1	1
6	1	0	0	17	x	x	0.25
7	1	1	0	18	x	x	0.75
8	0	x	x	19	x	x	x
9	x	0	x	20	x	x	1
10	1	1	x	21	0	1	x
11	0	0	1				

Table 2.9: Experimental design for CuNit on Precision 5000 with resistance heated deposition chamber. 0,x,1 correspond to low,middle,high settings, 0.25 and 0.75 describe the extra settings for the RF generator power.

The resulting adjusted response graph and corresponding significant terms can be found in figures 7.8 and 7.9. These graphs were used to program an optimized recipe onto the CVD system. Film properties with the last recipe are listed below. The deposition rate, as

	Dep. Rate [nm/min]	Unif. [%]	Ref. Ind. [ ]	Intr. Stress [MPa]
CuNit	134±4	1.2±0.05	1.876±0.010	-51±8

Table 2.10: Film parameters obtained from final CuNit recipe on the Precision 5000 with an CxZ chamber.

well as the index of refraction (RI) are well comparable to the LoHN results and match the target values. The intrinsic stress, however, is close to the upper limit of the desired range (-150±100 MPa). The reason for this offset is a mistake in handling the prediction tool of the CEDA software. Erroneously this recipe was not corrected afterwards. But as the responses of the material properties were the same as for LoHN, no further investigations were done with this CuNit silicon nitride variant in the later stages of this work.

In this set of experiments 6 inch wafers were used. This is the reason why it was easier to establish an uniform gas flow all over the wafer surface and thus yield the much better uniformity, compared to the values from the SiN_x variants above.

2.4.1 Remarks and Discussion

For the deposition rate clearly a linear regression model is sufficient regarding the factors RF generator power, silane flow and electrode spacing. Concerning the internal stress the tendencies are the same as for LoHN and SiN-m and a quadratic interaction model yields the best results. The RI, which is again measured by BPR at a wavelength of 630 nm, shows a nonlinear behavior in terms of RF generator power. This is also found true for the LoHN, but not for the SiN-m. With increasing silane flow also the RI is rising. This is again consistent with the results for LoHN, but not for SiN-m, where a nonlinear behavior can be observed.

2.5 Std. Nit on Precision 5000 (LH)

For the standard recipe of silicon nitride it was not necessary to perform a DoE regarding the factors and parameters mentioned above, because it has been studied extensively before, and optimized recipes were already available on every CVD system in Infineon. Within the electrical characterization, however, a small 3 factor DoE, in a full factorial design plus centerpoint was carried out. The main focus there was to find relations between the incorporated hydrogen and the conductivity of the material. Detailed values about that can be found in chapter 4.

2.6 Roughness of Films

Another interesting parameter for the film characterization is the surface roughness. SiN-m, Std. Nit and LoHN were deposited in different thicknesses onto 9 wafers and then examined. The roughness was determined by AFM (atomic force microscope) and XRR (X-ray reflectometry). As the XRR method requires thin films, each SiN_x variant was deposited in 40, 80 and 120 nm onto 8 inch M118 monitoring wafers.

The XRR measurement on the *JVX7300L* from Jordan Valley was carried out first, as it could be done inside the cleanroom and the wafers did not have to be cut to smaller sizes. Three spots on each wafer were examined, the exact locations on the wafer (x [mm] / y [mm]) being:

- 0.00 / 0.00
- 60.00 / -60.00
- -60.00 / 60.00

This method not only yielded the surface roughness, but also returned a value for the interlayer roughness between silicon nitride and substrate silicon wafer.

For the AFM measurements the wafers were sent to the 'Failure Analysis' department within Infineon. There the wafers had to be cut to a smaller size and then $10 \times 10 \, \mu$m spots from the center were examined in 512 scan lines. 2D and 3D images were also generated and the mean roughness was calculated not only from the full $10 \times 10 \, \mu$m area, but also from a smaller box within. Underlying idea was to select an area where it could be assured that the surface is not contaminated with particles. This approach was reasonable, because the AFM was not located inside the cleanroom, and additionally the breaking of the wafers to smaller pieces also generated particles, which adhere on the surface and can not be cleaned off completely. By comparing the roughness values from the full sample area with the area inside the box, it was possible to draw conclusions about the homogeneity of the film surface.

Figure 7.10 in the appendix for example shows that the 40 nm LoHN wafer has a highly uniform surface, while the 120 nm Std. Nit (figure 7.11) appears to be much coarser. The values from the AFM measurement compared with the data from the XRR can be found in table 2.11. Instead of the mean roughness (R_a) the root mean square (Rms = R_q) value is given[4].

SiN$_x$ variant	SiN-m			Std. Nit			LoHN		
Thickness [nm]	40	80	120	40	80	120	40	80	120
XRR-interlayer (R_q) [Å]	4.7	3.1	3.0	1.3	1.8	1.6	8.3	3.0	4.0
XRR-surface (R_q) [Å]	7.2	14.3	18.1	10.0	13.0	14.2	5.6	19.6	26.4
AFM-surface (R_q) [Å]	8.1	15.4	15.5	11.1	24.5	19.7	4.8	9.1	9.2

Table 2.11: Comparison of the roughness from the silicon nitride variants SiN-m, Std. Nit and LoHN. Measurements performed by XRR and AFM. The XRR values are the average values from 3 different sites across the wafer.

2.6.1 Remarks and Discussion

From the table above it is obvious that both, the XRR and the AFM results, show an generally increasing roughness with the thickness. But also significant differences between those 2 measurement techniques are visible. One of the reasons for this is that the investigated sample area as well as the spatial wavelength are not the same for the two techniques. The AFM examines a $10 \times 10 \, \mu$m spot in 512 lines. This means that the roughness can be resolved from 19.53 to $10 \, \mu$m.[5] The tip size can smear out the high frequency information so that the surface looks smoother.

In the XRR measurement on the other hand, the Cu K$_\alpha$ spectral line, which has a

---

[4] $R_q = \sqrt{\frac{1}{n} \sum_{i=1}^{n} y_i^2}$ ...Root Mean Square value

$R_a = \frac{1}{n} \sum_{i=1}^{n} |y_i|$ ...Arithmetic average of absolute values

[5] $\frac{10 \, \mu m}{512} = 19.531 \, nm$

wavelength of 0.15406 nm, is used. The lowest spatial wavelength is about $\lambda/2$. The X-ray beam itself has a width of 1 mm and due to the angle of incidence a 1 cm long part is investigated on the sample surface. So the XRR measurement gives information about a much bigger area.

Knowing this, the results from table 2.11 can be interpreted differently. LoHN has the smoothest surface compared to SiN-m and Std. Nit when looking at a small area, but it shows more roughness variations at a larger area as indicated by the XRR result. Literature roughness values for a 45.9 nm thick Si_3N_4 film on a Si(100) substrate wafer are 4.4 nm for GIXR (XRR) and 2.4 nm for AFM measurements.[42] The difference here can be ascribed to the different production process of the film.

Besides the difference in the spatial wavelength there are other factors that also influence the result of an AFM measurement, such as length of the AFM arm, environmental noise and cleanliness of the sample surface.[34] Latter could be important for the Std. Nit and SiN-m films, as white points (height peaks) in figure 7.11 are indicative for a particle contaminated surface. These particles most likely come from the process of breaking the wafer to smaller samples. According to [16] this white spots could also indicate very small crystalline areas but this was not investigated further.

A change in thickness does not affect the interlayer roughness, however SiN-m and LoHN apparently have a coarser interlayer structure than Std. Nit. As the difference is only in the region of approximately 2 Å this can also be a result of not optimized fitting of the SiN-m and LoHN data in the XRR measurement.

3 Tuning In-Line Measurements

During the measurements of the film properties from the DoE wafers some discrepancies were noted. Because of this not only the production of the SiN_x films, but also the measurement tools with their recipes and softwares were reviewed. In some cases it was necessary to adapt the recipe to the film to receive plausible results.

3.1 Refractive Index & Thickness

As described in the previous chapter, the tool OptiProbe was used for the measurement of thickness and index of refraction (RI). There are, however, different model versions of this tool and furthermore a variety of measuring techniques inside each tool can be selected. For the calculation of the thickness and the RI, the integrated software needed to be adapted to the material, to ensure a good fit of the data with the underlying mathematical model. A set of 9 samples, similar to those from the roughness measurement, was used to find out which model with which technique and fitting software is best suited for the a-SiN_x:H_y layers. The thicknesses of the films were 200, 400, and 800 nm for each of the three silicon nitride variants, SiN-m, Std. Nit and LoHN. The respective recipes stayed unchanged, just the deposition time was altered to get the different thicknesses.

To be able to compare the obtained results with each other, it was necessary to examine the same spots on every wafer.

3.1.1 Measurement Layout

For a standardized measurement a total of 9 measurement sites were placed in a certain pattern across the 8 inch wafer. It is called the '8Z9PKT' layout and it is the standard measurement pattern throughout this thesis. The 9 sites can be considered as elements of an imaginary spiral from the wafer center outwards. This layout ensures data acquisition from various distances from the center of the wafer, in all directions. The only important thing to ensure is that the general orientation of the wafer is always the same. Within this layout the notch (8 inch wafers) is pointing downwards, but inside all the OptiProbes this alignment is done automatically.

For the 6 inch wafers, which are in the context of this work only important for the

examination of CuNit, a less sophisticated pattern exists. There only 5 sites are scattered across the wafer but given the smaller size this pattern is sufficient. Due to wafer size and amount of sites this layout is called '6Z5PKT'. Instead of the notch a flat side of the wafer makes the proper alignment possible. A schematic sketch of those two layouts is presented in figure 3.1.
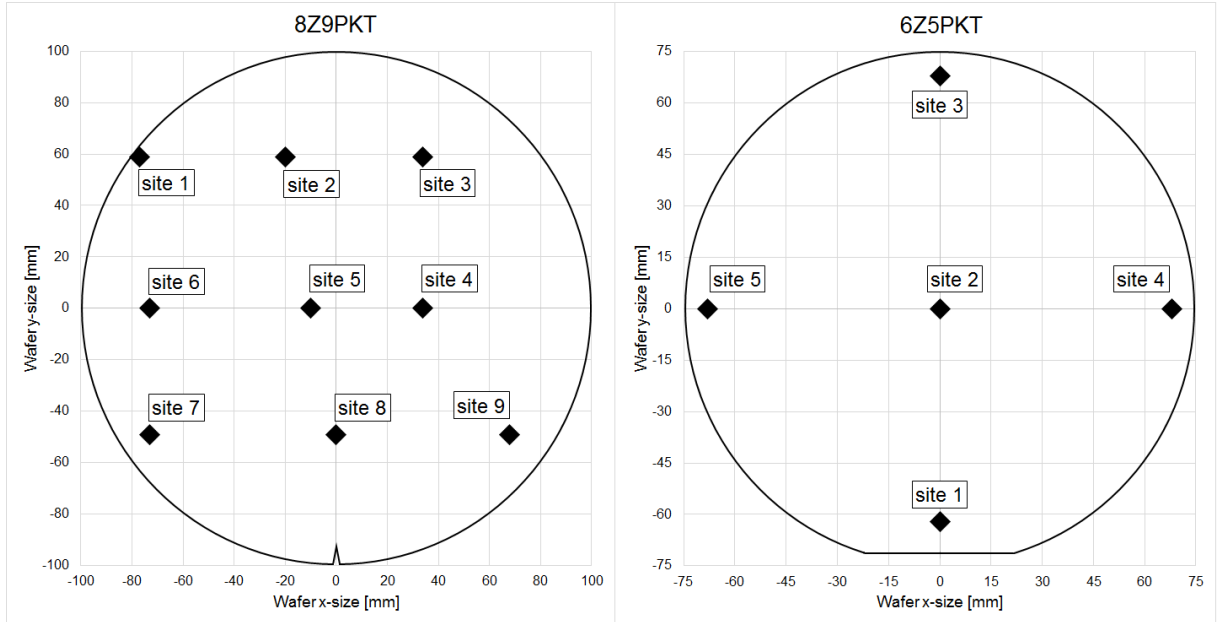
Figure 3.1: Patterns for the measurement of thickness and index of refraction on the OptiProbe tools. For the 8 inch wafers the 9 sites follow a spiral-pattern. Site 5 (8Z9PKT) and site 2 (6Z5PKT) are considered as center points of the wafer within the calculations of the hydrogen content.

The exact location of each site is given in table 3.1.

	8Z9PKT			6Z5PKT	
Site	x [mm]	y [mm]	Site	x [mm]	y [mm]
1	-77	59	1	0	-62
2	-20	59	2	0	0
3	34	59	3	0	68
4	34	0	4	68	0
5	-10	0	5	-68	0
6	-73	0			
7	-73	-49			
8	0	-49			
9	68	-49			

Table 3.1: Positions of the sites within the 6 and 8 inch measurement pattern.

After the thickness and RI values from all sites were measured, the range and the average

of those values from a single wafer (sw) was used to calculate the in-wafer (iw) uniformity.

$$\text{Unif}_{\text{iw}} = \frac{\text{Range}_{\text{sw}}}{2 \cdot \text{Average}_{\text{sw}}} \cdot 100 \tag{3.1}$$

Together with the iw-uniformity, the standard deviation between the measurement sites is determined as well. Those 2 values indicate how evenly produced a single wafer is and what deviations can be expected. To further find out if a process is running stably, the wafer-to-wafer (w2w) uniformity was calculated. Here the range and the average values from multiple films (mw), deposited with the same recipe, is needed.

$$\text{Unif}_{\text{w2w}} = \frac{\text{Range}_{\text{mw}}}{2 \cdot \text{Average}_{\text{mw}}} \cdot 100 \tag{3.2}$$

3.1.2 Testing the Tools

The 9 sample wafers were measured on 4 different OptiProbe model versions with the BPR (Beam Profile Reflectometer). Each of the 9 spots on the wafer was scanned along a $30\,\mu$m long line, which consisted of 36 separate $1\,\mu$m-diameter points. A 670 nm laser was used for the illumination and a high-magnification lens ensured incidence angles from 0 to 64 degrees simultaneously. The polarized reflected light was then detected by two (A and B) diode arrays and evaluated by the internal software. The used measurement layout and fitting model is the same on all tools.
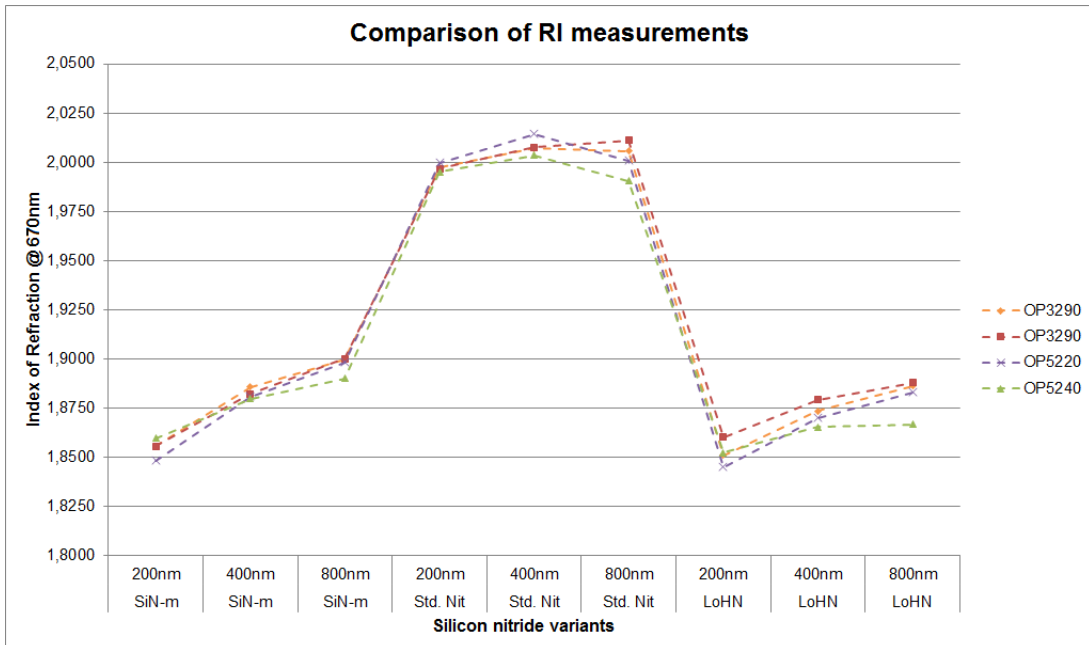
Figure 3.2: Comparison of the RI values measured on different OptiProbe machines. In all cases the same measurement recipe and layout was used.

A comparison of the values shows that in tendency the deviation between the models increases with the film thickness of the samples. However, for both, thickness and RI, the deviation was always smaller than 0.45 %. Interestingly the RI value increases with the film thickness for SiN-m and LoHN, but not for Std. Nit (figure 3.2). The measured thickness and RI values with the deviations between the measurement tools are listed in table 3.2.

| SiN_x variant	SiN-m			Std. Nit			LoHN		
Avg. thickness [nm]	203.9	395.9	778.5	207.5	406.5	818.0	214.8	409.5	819.7
Std. deviation [nm]	0.37	0.37	1.55	0.21	0.79	3.18	0.53	0.94	3.38
Rel. deviation [%]	0.18	0.09	0.20	0.10	0.19	0.39	0.25	0.23	0.41
Avg. RI [ ]	1.855	1.882	1.897	1.997	2.008	2.002	1.852	1.872	1.881
Std. deviation [ ]	0.004	0.002	0.004	0.002	0.004	0.008	0.005	0.005	0.008
Rel. deviation [%]	0.22	0.12	0.22	0.08	0.19	0.38	0.29	0.27	0.45

Table 3.2: Average RI values measured on different OptiProbe machines and their deviation. The deviation increases with the film thickness of the sample.

An increasing refractive index can indicate a higher film density. This would be true if the very first atomic layers of the film do not form a good structure on the substrate wafer but the following ones form the bulk crystal structure of the deposited film. Unfortunately no scale was available to measure and verify an increasing film density. Nevertheless, as the RI for SiN-m and LoHN went up quickly while the one of the Std. Nit films first rose and then declined with the thickness, another more sophisticated measurement recipe was created.

3.1.3 Fitting Model

Instead of only using the BPR, now also the broad band spectroscopic ellipsometer (SE; 200-800 nm) was used for the data acquisition. To find a suitable fitting model, the thickness of the deposited films was also measured via a XRR measurement for reference purposes. A new set of samples with thinner (40-80-120 nm) SiN_x films was prepared to make an investigation via XRR possible.

After recording of the data a further improvement of the fitting model was done with the software *Global Optimizer* from Therma-Wave. A so-called Cauchy model was used for the fitting process, the selected Cauchy parameters can be found in table 3.3.

This optimized fitting model was then used to re-evaluate the set of films used in the beginning. Of course it was necessary to measure all samples again to get the additional information from the spectrometric ellipsometer as well. As can be seen in figure 3.3, the combination of BPR and SE with the optimized Cauchy fitting model yields better results, where obviously the deposited film thickness does not influence the index of refraction that

Cauchy Parameters			
NW0:	0.000106	KW0:	0.063931
N1:	-5.379181	K1:	1.353781
N2:	0.007932	K2:	-0.000121
N3:	-0.000105	K3:	-0.000041
N4:	0.000023	K4:	0.000001

Table 3.3: Cauchy parameters of the optimized fitting model.

much, yet a slight rise can be noted. For the Std. Nit film a more linear behavior can be observed.
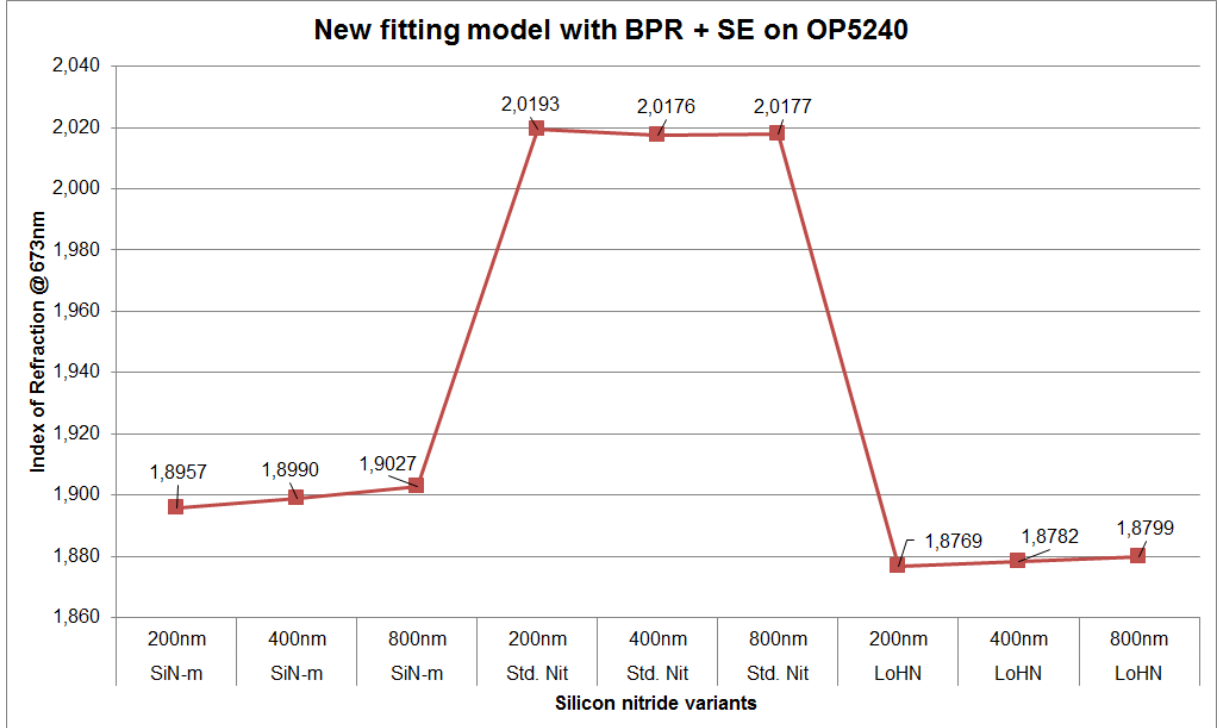
Figure 3.3: With the optimized fitting model re-evaluated set of wafers.

Along with the RI and the thickness, the extinction coefficient k was determined from the fitting model as well. This coefficient describes the attenuation of light when passing through the medium. The complex index of refraction can thus be written as

$$\boldsymbol{n} = n + ik \tag{3.3}$$

At long wavelengths ($>400\,\mathrm{nm}$) the extinction coefficient is close to zero for all silicon nitride variants. Below $390\,\mathrm{nm}$, however, the k-value of the Std. Nit already starts to rise, while the light absorption starts only at shorter wavelengths for SiN-m ($250\,\mathrm{nm}$) and LoHN ($290\,\mathrm{nm}$). The corresponding figures for SiN-m and LoHN can be found in the

appendix on page 91.

The reason why the k value of Std. Nit already rises at longer wavelengths is the, compared to the SiN-m and LoHN films, much higher amount of Si-H bonds. They absorb waves from the ultraviolet (UV) region. Also Si dangling bonds can be annihilated when exposed to UV illumination[41]. Due to that UV absorbance also special UV-transparent silicon nitride films (with low Si-H content) are used e.g., for the coating of EPROMs (Erasable Programmable Read-Only Memorys) as the erasing procedure needs UV illumination and an UV absorbing film would impede that.
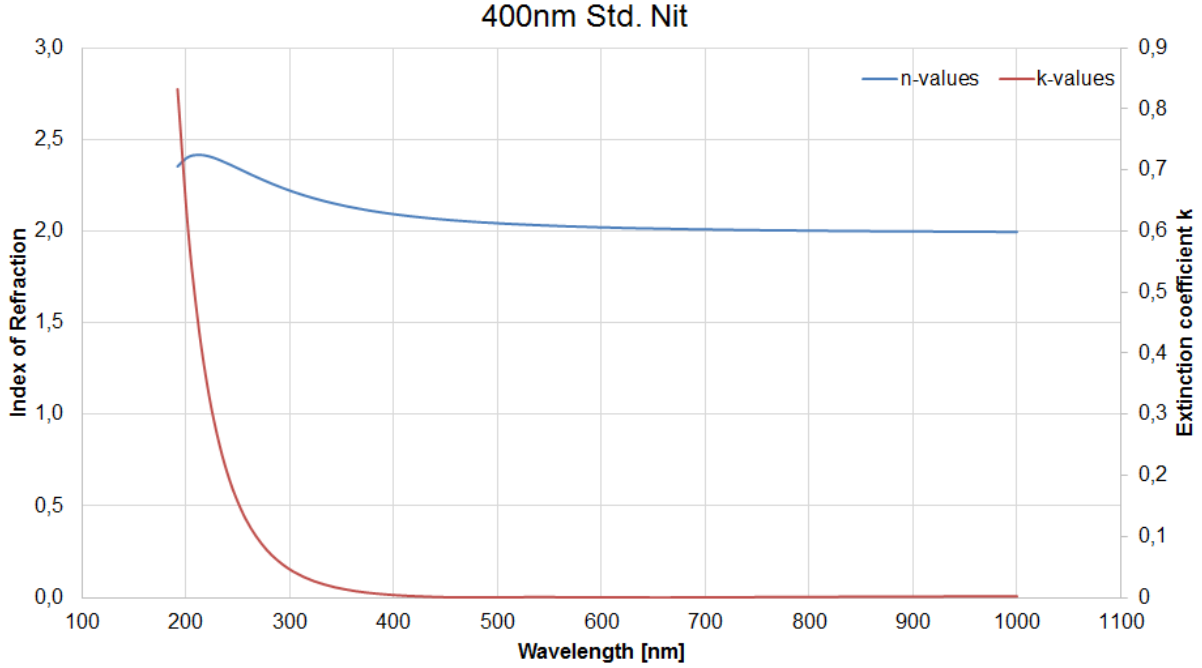
Figure 3.4: Refractive index and extinction coefficient for a 400 nm Std. Nit film. The n-peak is at 212 nm.

Furthermore it is possible to deduce the absorption coefficient α from the extinction coefficient k from the ellipsometry measurement by using the following relation

$$\frac{\alpha c}{2\omega} \quad = \quad n'' = k = n'\kappa \qquad \left| \quad \omega = 2\pi f \;\; ; \; f = \frac{c}{\lambda} \right. \tag{3.4}$$

$$\alpha \quad = \quad \frac{4\pi k}{\lambda} \tag{3.5}$$

An idea for a further investigation is to compare the α from the ellipsometry measurement with the one from the FTIR spectra. But as the examined wavenumber (wavelength) regions do not overlap this is not possible. The FTIR spectrum covers the range from 25000-2500 nm (400-4000 cm^{-1}), the ellipsometry measurement on the other hand only goes from 190-1000 nm. For a comparison the data from an UV/VIS spectroscopy would

be needed.

3.1.4 External Measurements

Some samples were sent to Graz University of Technology for an additional analysis. Here the measurements were carried out on a spectral ellipsometer. The result for a 70 nm Std. Nit sample is shown in figure 3.5.
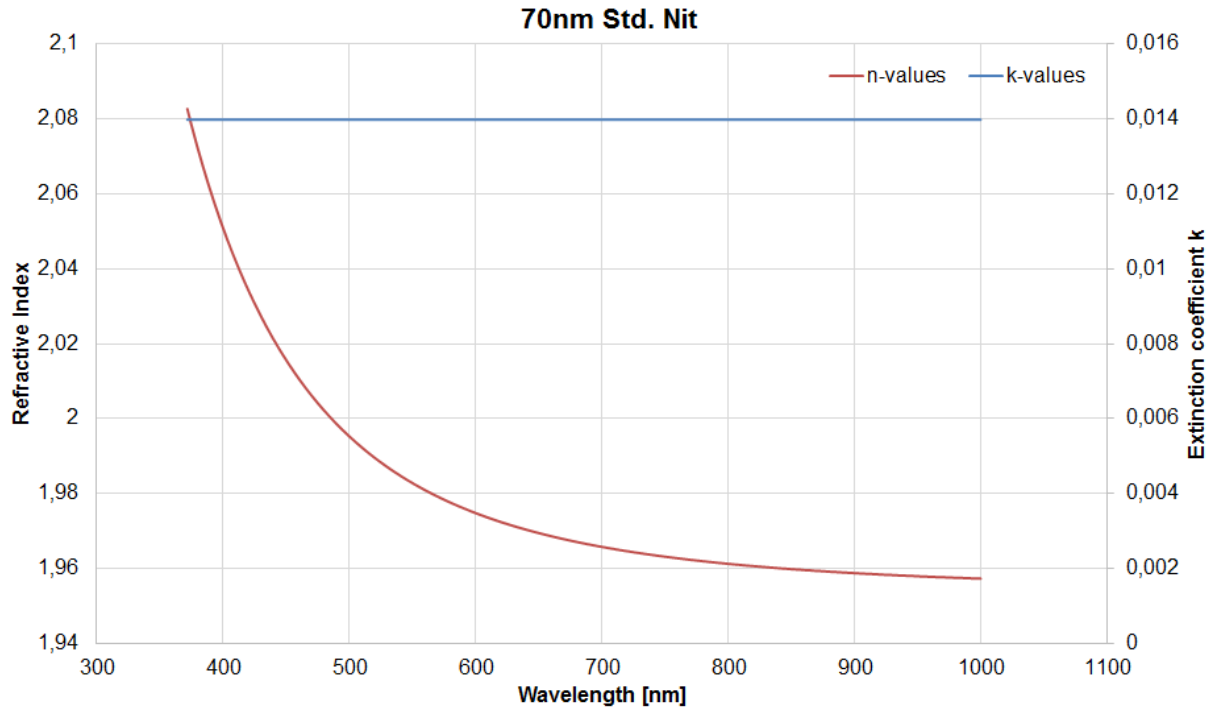
Figure 3.5: Refractive index and extinction coefficient for a 70 nm Std. Nit film. The measurement was performed at Graz University of Technology on a spectral ellipsometer.

It is obvious that the n- and k-values are different from the ones recorded within Infineon. Reason for this could be that a much thinner Std. Nit film was examined in Graz, or, more likely, different fitting models were used for the data evaluation. The Infineon model uses the BPR and the SE to calculate the 3 unknown parameters thickness, n and k. Furthermore it was optimized for the non stoichiometric silicon nitride variants obtained from PECVD processes. In Graz the fitting of only the SE data had to calculate 3 film parameters without specific knowledge about the material.

3.2 Hydrogen Content

For the determination of the hydrogen content the *QS-500* FTIR spectrometer was used. The underlying principles can be found in section 1.4.5.

The test site is in the wafer center and the absorption in the infrared (IR) region after transmission through the wafer and the film is recorded. This process is repeated 32 times at the same spot for a good signal-noise ratio. The IR spectrum of a bare wafer is gathered prior to the measurement of the coated wafer. This spectrum not only contains the absorption lines of the substrate wafer, but also information about influences specific for the tool (e.g., CO_2 and H_2O inside). It is used as the background (I_0) spectrum.

The actual sample absorbance (SA) is obtained after taking the logarithm to the base 10 of the sample spectrum divided by the background spectrum, so

$$SA = \log_{10}\left(\frac{I}{I_0}\right) \tag{3.6}$$

Together with the thickness of the deposited film on the related site, the hydrogen content was calculated by the software installed on the FTIR spectrometer. For 8 inch wafers the thickness values from the OptiProbe measuring site 5 (see fig. 3.1) was used, for 6 inch wafers site 2.

Due to the importance of knowing the incorporated hydrogen content in the silicon nitride variants within this thesis, a closer investigation of the determination process was
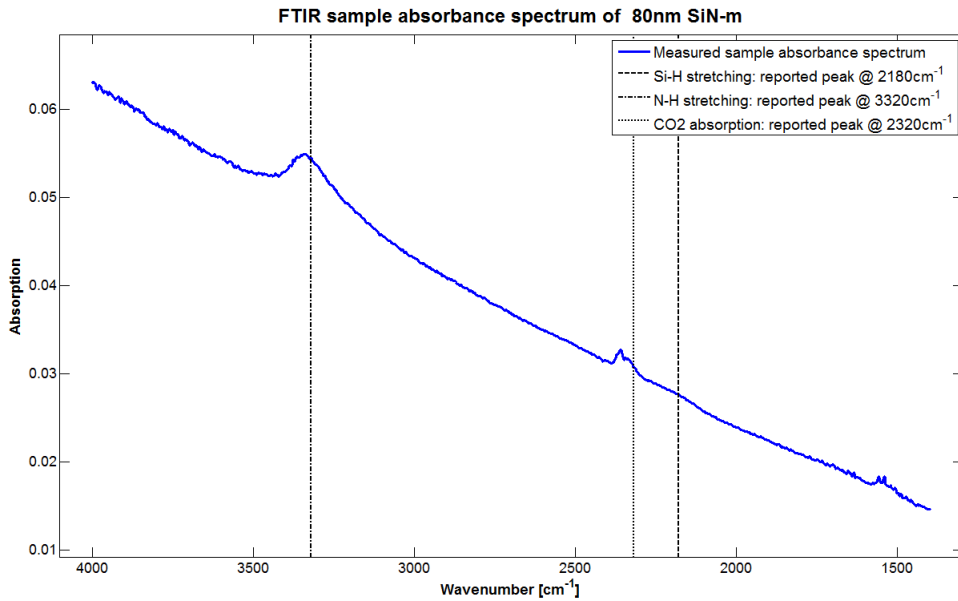
Figure 3.6: Sample absorbance spectrum of an 80 nm SiN-m film. Installed software reports the Si-H absorption peak to be at 2359 nm and a Si-H content of $4.4\text{e+}21\,\text{cm}^{-3}$.

initiated. The bone of contention was that in some cases disagreements between the shape of the spectrum and the output for the hydrogen content were noted, especially when CO_2 peaks distort the sample absorbance spectrum. Such a case can be seen in figure 3.6. The

installed software reports the Si-H absorption peak to be at 2359 nm and a Si-H content of $4.4e+21\,cm^{-3}$, although no Si-H peak is visible at the wavelength reported in literature.This led to the conclusion that the CO_2 peak is misinterpreted for Si-H.

Thus a Matlab script was created to evaluate the FTIR spectra and determine the hydrogen content.

3.2.1 Baseline Fit

Either the area underneath, or the height of the peaks themselves is needed to calculate the hydrogen content. In both ways a well fitted baseline (BL) is crucial. To avoid the distorting influences of possible CO_2 or H_2O impurities inside the spectrometer, certain wavelength regions had to be excluded from the fit. Furthermore, instead of fitting the full BL at once, 6 smaller areas were fitted separately. It also needs to be taken into consideration that the shape of the sample absorbance spectrum can change with the film thickness. Because of this the fitting parameters may change with the thickness as well. Polynomial fits of different degrees turned out to be best suited for this task. The wavelength ranges for each area, the excluded areas, and the fit degrees are presented in table 3.4.

Area	Fit from/to $[cm^{-1}]$	Excluded from/to $[cm^{-1}]$	Fit degree
1	1400 / 1800	1485 / 1700	3
2	1610 / 1995	-	2
3	1925 / 2475	2020 / 2400	2
4	2430 / 2900	-	3
5	2700 / 3750	3000 / 3540	4 (3 for d<350 nm)
6	3600 / 4000	3700 / 3850	3

Table 3.4: Parameters for the baseline fitting procedure.

To obtain the final baseline, the 6 separate fitting areas were merged together. It is obvious that the areas overlap on their edges. For a smooth transition from one region to the next, the values inside the overlapping area of the ending region were weighted from 100 to 0 %, the values of the starting area from 0 to 100 %.

3.2.2 Effective Thickness

For the calculation of the hydrogen content, the film thickness needs to be known. According to Brendel it is necessary to introduce a function for an effective thickness correction for SiN_x films, as simply using the Lambert-Beer law can lead to errors of up to 80 %[6]. The appropriate effective thickness of a given real film thickness can be interpolated from a numerically calculated curve. For a fast and easy thickness correction, the numerically

calculated curve was approximated by a trapezoidal function. This trapezoidal function, shown as red line in figure 3.7, fits very well to the sine-like numerical curves.
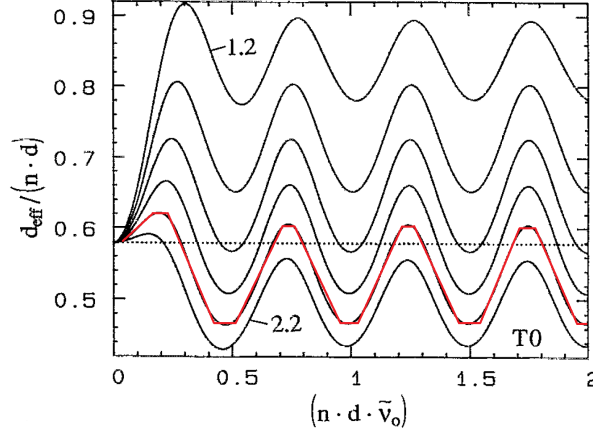
Figure 3.7: Trapezoidal approximation (red line) of the numerically calculated effective thickness curves. The refractive index increases from top to bottom in steps of 0.2. After [6].

The values of the dimensionless but thickness dependent function $f(d)$ for the effective thickness correction used within this work are given below. They are not the ones presented from Brendel, but they were deduced empirically from experiments by Stadtmüller. Due to the wavelength difference of the corresponding peaks, two different equations were used for the calculation of the Si-H and N-H concentration. The real thickness d needs to be inserted in terms of nanometers.

$$
\text{N-H correction:} \quad f(d)_{NH} =
\begin{cases}
1.03 + \frac{d}{300} \cdot 0.12 & ; \quad\;\; 0 < d \leq\;\; 300 \\
1.15 & ; \;\; 300 > d \leq\;\; 460 \\
1.15 - \frac{d-460}{280} \cdot 0.29 & ; \;\; 460 > d \leq\;\; 740 \\
0.86 & ; \;\; 740 > d \leq\;\; 860 \\
0.86 + \frac{d-860}{270} \cdot 0.28 & ; \;\; 860 > d \leq 1130 \\
1.14 & ; \; 1130 > d \leq 1250
\end{cases}
$$

$$
\text{Si-H correction:} \quad f(d)_{SiH} =
\begin{cases}
1.00 + \frac{d}{480} \cdot 0.17 & ; \quad\;\; 0 < d \leq\;\; 480 \\
1.17 & ; \quad 480 > d \leq\;\; 680 \\
1.17 - \frac{d-680}{420} \cdot 0.32 & ; \quad 680 > d \leq 1100 \\
0.85 & ; \; 1100 > d \leq 1300 \\
0.85 + \frac{d-1300}{400} \cdot 0.30 & ; \; 1300 > d \leq 1700
\end{cases}
$$

Once the function for the effective thickness is known, only the peak height is missing for

the calculation of the H-concentration.

3.2.3 Peak Height

As influences of CO_2 distort the Si-H peak, the area underneath the peak changes as well and falsifies the resulting H-content. Due to that the height of the peak was used instead, but there are also 2 different ways of measuring it. The height can either be measured directly within the original sample absorbance spectrum where the calculated baseline is included, or, as done within this work, the baseline can be subtracted from the measured values in order to get a flattened (BL corrected) spectrum prior the height evaluation. In figure 3.8 the 6 different areas for the baseline fit are included as well but they are shifted vertically for clarity.
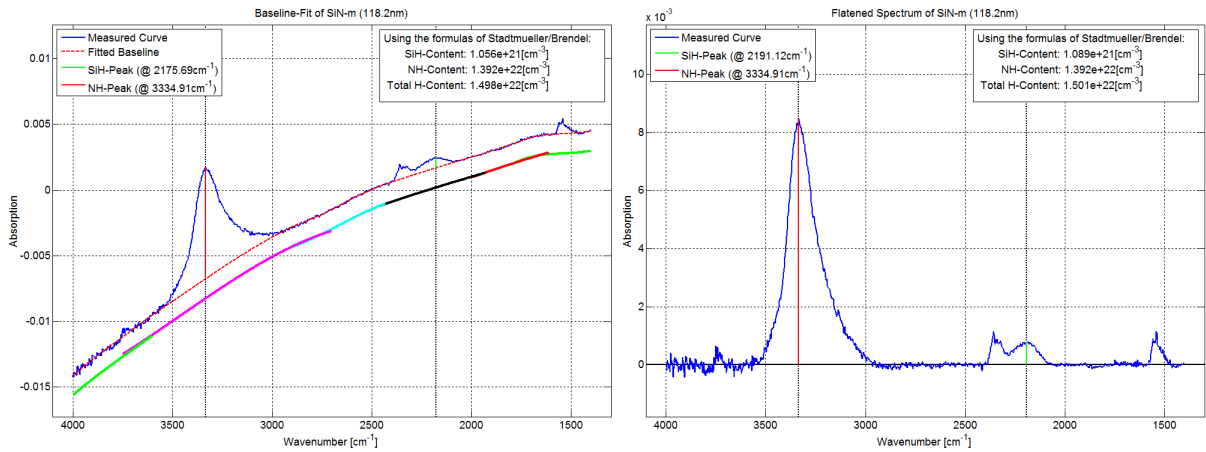
Figure 3.8: FTIR spectra for a 120 nm SiN-m film. The colorful 6 separate areas for the baseline fit are shifted vertically for clarity.

The influence of CO_2 is excluded from the BL fit, but it is obvious that it would have a great impact on the H-content if the area is used for the calculation instead of the height. When the BL is subtracted from the sample absorbance spectrum, the peaks shift and also the height of the peak changes slightly. The change in the values for the Si-H and N-H concentrations, however, is very small and can thus be neglected.

Within the Matlab script the peak height was obtained by simply searching for the biggest value around the respective wavelength ± 40 nm. So for SiH it is 2180 ± 40 nm, for NH 3320 ± 40 nm. Especially for the SiH peak this flexibility is necessary, as it is reported to shift to lower frequencies when the N/Si ratio of the film decreases.[18] This lower frequency is caused by a decrease in the Si-H bond strength which is because the Si neighbors are replaced by more electronegative N-atoms.[22] This peak shifting is also explained as sign of an amorphous to crystalline transition in [37].

In case that the possible area for the peak offset is set too large, there is the risk that,

like in figure 3.6, a wrong height is used inside the calculation. The spectra of all 3 silicon nitride variants side by side can be found in the appendix on page 92.

The area can also be calculated by fitting a double gaussian curve to the corresponding area and again excluding possible CO_2 influences. Nevertheless, the approach with the peak height is used inside this work as it can be performed more easily and yields satisfying results.

3.2.4 Calculation of Hydrogen Content

Starting point for the calculation of the hydrogen content in plasma-deposited silicon nitride is the method presented by Lanford & Rand.[19] They determined calibration factors for Si-H ($2160\,\mathrm{cm}^{-1}$) and N-H ($3350\,\mathrm{cm}^{-1}$) which enable FTIR spectra to be used for a H-content analysis. Also the fact that the Si-H bonds within SiN_x films have about 1.4 times the specific absorption of N-H bonds is considered in that calibration factors. With those factors the area underneath the peaks attributed to Si-H or N-H bond absorptions can directly be used to calculate the hydrogen content once the film thickness d_{real} is known.

As this approach can still yield errors of up to $80\,\%$ the effective thickness correction from Brendel, as explained in subsection 3.2.2 was included to obtain better results. Furthermore the peak height was used instead of the peak area to avoid mistakes from CO_2 distorted peaks. The formulas used within this work for calculating the Si-H and N-H concentration are given below.

$$\mathrm{SiH\ [atoms/cm^3]} \quad = \quad \frac{h_{Peak}}{d_{real}[\mathrm{cm}]} \cdot \frac{1}{f(d)_{SiH}} \cdot 0.95 \cdot \frac{\ln(10)}{1.3 \cdot 10^{-19}[\mathrm{cm^2}]} \tag{3.7}$$

$$\mathrm{NH\ [atoms/cm^3]} \quad = \quad \frac{h_{Peak}}{d_{real}[\mathrm{cm}]} \cdot \frac{1}{f(d)_{NH}} \cdot \frac{\ln(10)}{1.1 \cdot 10^{-19}[\mathrm{cm^2}]} \tag{3.8}$$

The real film thickness d_{real} was measured with the OptiProbe, the corresponding sites of the layout (fig. 3.1) were spot 5 for 8 inch wafers and spot 2 for 6 inch wafers. For the effective thickness correction the function $f(d)$ as described in subsection 3.2.2 was used for the SiH and NH content. The factors for the conversion of IR-absorption bands to H-content are based on the Lanford & Rand gauging, but adapted by Michael Stadtmüller to fit for the usage of the peak height instead of the area.

The total amount of incorporated hydrogen is the sum of the SiH and NH concentrations[4]. According to Claassen et al.[10], when the SiH and NH concentration is known, not only the total hydrogen concentration but the stoichiometry of the film is known as well by using equation 1.36.

By comparing the results calculated with the Matlab script with the results from the tool, an average relative error of $6\,\%$ can be estimated. When the peak is very small and addi-

tionally CO_2 impurities distort the measurement, the error is likely to be higher though. This is because then the estimation of a fitting baseline to the FTIR spectra is difficult, as explained in subsection 3.2.3.

3.2.5 Comparison with QS-3300 Spectrometer

In a last step the Matlab results were compared with the results from another, newer FTIR spectrometer (*QS-3300*), which scans 9 positions on the wafers, following the 8Z9PKT pattern. Instead of using a polynomial fit for the creation of the baseline, here a linear fit

SiN_x variant	SiN-m			Std. Nit			LoHN			Tool
d [nm]	40	80	120	40	80	120	40	80	120	
SiH [1/cm^{-3}]	-0,76	1,03	-0,05	7,26	7,75	7,95	-1,94	-1,23	0,45	A
SiH [1/cm^{-3}]	1,37	1,26	1,07	8,37	7,95	8,01	1,21	0,78	0,66	B
NH [1/cm^{-3}]	11,46	11,81	12,16	4,16	4,20	4,53	8,99	9,37	9,71	A
NH [1/cm^{-3}]	13,00	13,43	13,71	5,31	4,85	5,01	10,11	10,34	10,86	B

Table 3.5: SiH and NH values +1E21. Tool A... *QS-3300*, B... Matlab script.

was applied underneath the SiH or NH peak. This is the reason why the software has problems evaluating spectra from films with either CO_2 distortions, and/or low hydrogen concentrations. Especially LoHN and SiN-m films, which have a low SiH content (fig. 7.15 and 7.16), were sometimes even evaluated to a negative result. A baseline which is placed above instead of underneath the the peak can cause this result. For the Std. Nit wafers, which have clear SiH peaks, the results are similar. Concerning the NH content it is obvious that the software from the *QS-3300* delivers in average an 12 % lower value. This can indicate an offset error, which can be corrected with an additional factor in the data evaluation.

4 Electrical Characterization

First in chapter 2 knowledge about how to tune film parameters by changing process factors was collected, with the execution of various designed experiments. This information was used to program fitting recipes for the 3 SiN$_x$ variants Std. Nit, SiN-m, and LoHN into the CVD systems. As the stoichiometry of the films is different from standard materials, some measurement techniques were adapted to yield good results, which is described in chapter 3. Now the next step is to characterize the electric properties of those films.

4.1 General Procedure

The basic idea is to build up capacitor structures with the different silicon nitride films, and then record voltage-current (U-I) curves for the characterization. For this purpose point probe stations with connected source monitoring units (SMUs) were used. The film thickness of the samples is varied from approximately 40 to 800 nm. Additionally measurements on a capacitance-voltage tool (*CVmap 3093-AC*) were carried out, as this tool can directly output the relative permittivity for a certain frequency.

To investigate the influence of hydrogen, a DoE based on the Std. Nit SiN$_x$ variant was performed. This is described in section 4.4.

4.1.1 Sample Preparation

Due to their good conducting properties, P082 8 inch wafers were chosen as the substrate material for the electrical characterization. Their specifications can be found in table 1.3 on page 15. The high n+ antimony doping also affects the FTIR transmission measurements and thus prevents a calculation of the incorporated hydrogen content. Because of this, additionally M118 monitoring wafers were coated right after the finished deposition on the P082 wafers with the exact same deposition recipes. So the sample films were deposited twice. While the films on the monitoring wafers were undergoing all the parameter measurements for RI, thickness, H-content, etc., the highly doped wafers were passed along in a fabrication process to build the capacitor structures.

This process to go from the empty substrate wafer to the measurement-ready wafer full of capacitor structures took 20 separate steps. Within the first steps arsenic was implanted

into the already n+ doped substrate material at 100 keV. Due to that very high doping, the silicon wafer can rather be regarded as metallic contact instead of a semiconductor. After a chemical clean and implantation anneal, the different silicon nitride films were deposited inside a Precision 5000 CVD system. Following this, a 750 μm thick AlSiCu layer was sputtered on top of the SiN_x which served as surface electrical contact. The Si is used to prevent spiking inside the aluminum layer, the Cu ensures a low electromigration. With this, the general MIM (metal-insulator-metal) structure is completed and it can already be interpreted as capacitor structure, as shown in figure 4.1.
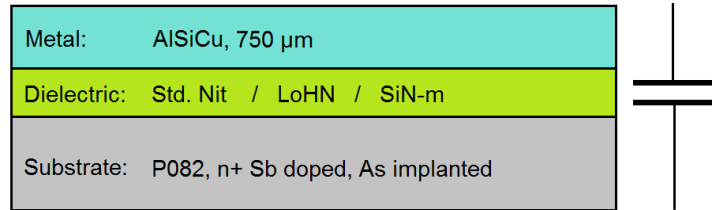
Figure 4.1: Schematic structure of the wafers for the electrical characterization. Due to the high doping it can be considered a metal-insulator-metal capacitor structure.

Then a positive photoresist was applied onto the aluminum, and the so-called G0900 mask was used for structuring. A wet-chemical etching process creates a top electrode structure with all the different electrodes, and another cleaning process removes the excess photoresist. At the end also the backside of the wafer underwent an etching process, this guaranteed a clean backside surface and a good electrical contact with the chuck later on.

4.1.2 G0900 Mask

To create a certain structure on a wafer, a mask is necessary in a lithography step. Here the G0900 was used for the structuring of the photoresist. The mask actually just shows one 'reticle', but after repeated use it is possible to project several reticles side by side onto the wafer surface. As a positive photoresist is used, the areas which lie underneath the undeveloped resist material are protected during subsequent etching.

The layout of the G0900 mask, as shown in figure 4.2, offers 24 electrodes within each reticle, their areas reach from 0.01 to 16 mm^2. The labeling does not cover all electrodes, but only the ones used for this work. Most of the U-I curves recorded are from the E, I and J spots.

It is possible to print 546 reticles onto an 8 inch wafer, which yields a total of 13104 possible capacitor structures for testing on a single wafer. This huge number makes it inevitable to use a system, which precisely defines which site is chosen for investigation. A coordinate system, as sketched in figure 4.3, was defined for this purpose. The first reticle

on the wafer, which is slightly shifted to the right of the notch, can thus be described as
$(x = 0 \mid y = 1)$.

Figure 4.2: Reticle of the G0900 mask. Electrode areas go from 16 (A) to $0.01\,\text{mm}^2$ (L).

When the standard 8Z9PKT layout (fig. 3.1) is overlayed, it is obvious that for example
the measurement site 6 corresponds with the reticles $(-8, -9, -10 \mid 14, 15, 16)$.

Figure 4.3: Definition of the coordinate system for the electrical measurements.

4.1.3 Area calculation

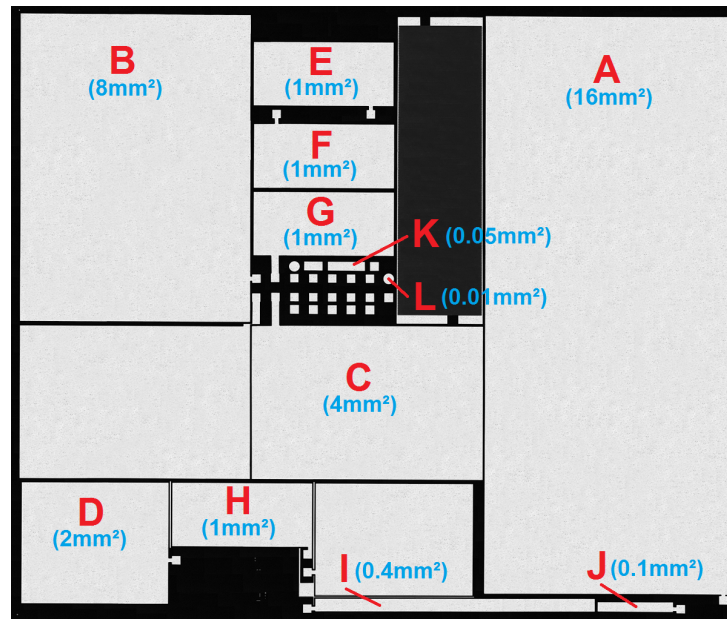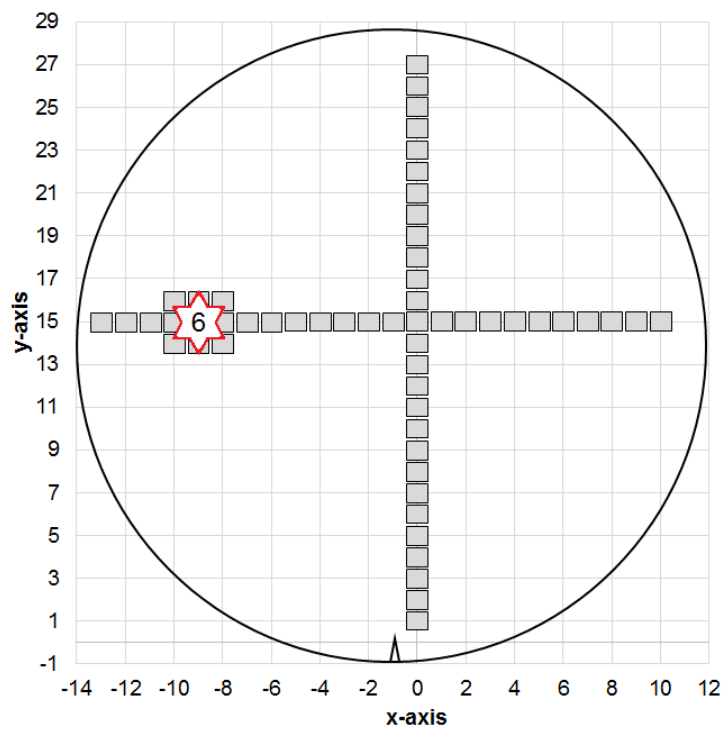To obtain the areas of the electrodes, the samples were examined under a light microscope. A built-in scale for each magnification of the lens made length, and thus area measurements as well, possible. The calculated sizes of the spots, as defined in figure 4.2, are:

Spot	Area [mm^2]	Error [%]	Spot	Area [mm^2]	Error [%]
A	16.89	± 0.31	G	1.08	± 0.27
B	8.42	± 0.19	H	1.06	± 0.27
C	4.23	± 0.17	I	0.44	± 1.52
D	2.13	± 0.45	J	0.10	± 0.82
E	1.06	± 0.45	K	0.05	± 0.55
F	1.06	± 0.30	L	0.01	± 0.37

Table 4.1: Measured areas of the G0900 electrodes as defined in figure 4.2.

4.1.4 Point Probe Station

Due to access reasons three different point probe stations were used for the electrical characterizations. Their setups, however, were similar.

The wafer was placed on a movable hot chuck, which holds it in position using vacuum. Temperatures between 15-200 °C could be selected. Furthermore the chuck acted as the bottom electrical contact throughout the measurements. The top contact to close the electric circuit was formed by a needle which is placed on the wafer with the help of a micropositioner. To be able to contact the small electrodes, a light microscope with different magnification lenses was located above the wafer. The voltage-current curves were recorded on a computer, for the actual measurement tools however, different ones were used in the stations.

The first station was called the *S-Matrix* because of its 'switching matrix' that could connect a variety of different source-monitor units (SMUs) to different measurement lines. In the setup for this work the SMUs Hewlett Packard HP41420A and Agilent 41420A were used in the way of a four-terminal sensing setup. While the former was connected to the chuck with a force and a sense wire, the latter one had the force and sense wires connected to the needle which ensured the top contact. The electrical circuit between the SMUs was closed inside the switching matrix. According to the specs of those SMUs, which are listed in section 1.4.4, each of them could go up to 200 V. When one side (e.g., the chuck) was set to constantly -200 V while the SMU on the other side performed a sweep from 0-200 V in reality a sweep range up to 400 V could be realized. This was only done for testing purposes, the actual measurement was carried out with the chuck set to 0 V to act as

ground and the voltage sweeps were performed with the SMU connected to the needle.

A black box was located around the complete probe station for two purposes. First for security reasons, as a switch inside the doors of the box prevented the start of a measurement unless the doors were closed, and second to keep light out. There is a risk that photoconductivity is measured if light hits the sample, but as in the case of the tested devices the SiN_x film was shielded by the electrodes, this effect was not so relevant.

A parameter analyzer Agilent 4156C was used in the second setup. It was called the *Phemos-1000*. Voltage sweeps were again performed on top of the wafer with the needle contact and the chuck served as ground.

Unlike the two previous probe stations, the third one was not located inside a black box, and 3 Keithley 2400 source meters allowed the usage of 3 measurement needles simultaneously. But again the chuck was put to the common ground together with the source meters.

4.2 Initial Measurements

The films for the sample wafers were produced on a Precision 5000 CVD system and the thickness for each SiN_x variant was varied from approximately 40 - 800 nm. Information about the thickness steps are listed in table 4.2. Additionally two wafers were left blank intentionally to see if a short circuit is formed when the probe needle is placed onto the Al surface of the test structure. This test proved that the electrical contact between substrate wafer and sputtered aluminum is good.

Wafer	$1 - 18$	19 & 20
Variant	SiN-m / Std. Nit / LoHN	blank
d [nm]	$40 - 80 - 120 - 200 - 400 - 800$	0

Table 4.2: Set of sample wafers for the initial electrical measurements.

After the confirmation that a short circuit can be formed, the first sweeps up to 200 V with the real sample wafers were performed.

4.2.1 Charging Effect

A rather strong charging effect could be observed on all silicon nitride variants after the initial voltage sweep. This was noticeable because of the lower leakage current in the following sweeps as presented in figure 4.4.

Several measurement parameters were adjusted for a further investigation. Small steps in the voltage sweep along with a long data acquisition time yielded smoother curves. Further a delay of maximum 1 second between applying the voltage and measuring the

current was set to ensure that the material has enough time to react to the applied electric field. But also with shorter delay times the curves did not change their shape. As these settings took too much time for the measurement, the voltage steps were set to 0.5 V and the delay time to 10 ms.
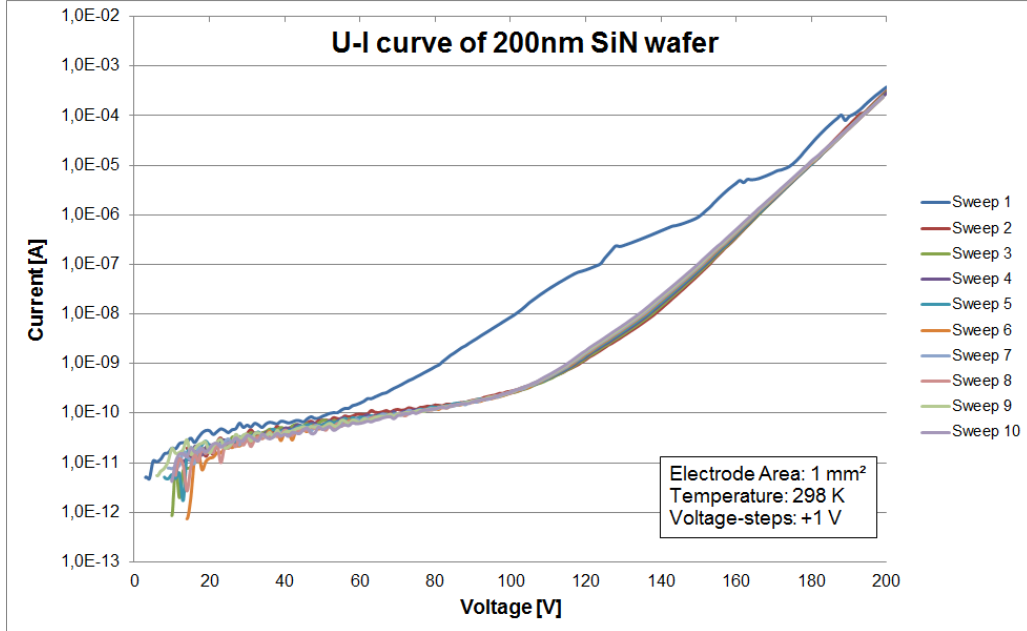
Figure 4.4: Charging effect of 200 nm SiN-m film.

An explanation for this charging effect could be that charges from traps, following the Poole-Frenkel theory, contribute to the current on the first sweep, but then these traps are not filled up with charges anymore. While the PF emission (see fundamentals section 1.1.6) only talks about charges from traps that reach the conduction band, it is necessary that charges reappear in the emptied traps to establish an actual current through the dielectric film. This refilling of empty traps is likely to be caused by a tunneling processes when the distances between the traps are not too big, so the trap density is high enough. In [16] the presence of small platelet-type crystalline areas are reported for RF glow discharge deposited silicon nitride. Stacking faults in those transition areas from amorphous bulk to a crystalline area are the cause for traps inside the nitride. When a high electric field is applied to the film, the distribution, density and occupation of the traps are changed. It is conceivable that the first voltage sweep moves the charges out of the traps but the high electric fields also change the trap density and distribution in such a way that not all of them can be filled up again in the second sweep by tunneling and thus a lower leakage current is observed.

More U-I curves were recorded with up to 48 hours idle time between 3 initial conditioning sweeps, and 3 more reference sweeps. Even after the longest waiting time, the charging

effect could not be observed again. This supports the contention that the locations of the traps are changed with the electric field of the conditioning sweeps and they do not form back over time.

After a heat treatment, however, the charging effect could be found again. Furthermore the heat treatment also improved the insulating properties of the PECVD silicon nitride. For a 55 nm SiN-m film, a heat treatment of 190 °C for approximately 15 minutes causes the charging effect to re-occur, but it also lowers the leakage current density by one decade. Figure 7.17 in the appendix shows that behavior graphically.

This leads to the conclusion that a material conditioning with a heat treatment plus an initial voltage sweeps is advisable. Doing so yields a material which not only exhibits predictable voltage-current behavior, but also the overall leakage current can be reduced versus the standard virgin films. The reduction of the overall leakage current can be described that the trap density is further reduced by the heat treatment.

4.2.2 Breakthrough and Insulation Properties

When the applied electric field became too high during the voltage sweep, the silicon nitride film failed and a breakthrough occurred. The breakdown field strength (E_{BR}) is another parameter that is used to characterize a dielectric material. To protect the measurement equipment from possible damage, a compliance level for the current has to be set along with a maximum voltage range for the sweeps. As sweeps up to 200 V were planned, a compliance level of 20 mA was set. This limited the power in case of a breakthrough to a maximum of 4 W.

It turned out that for the films thicker than 200 nm the breakthrough voltage could not be measured due to the equipment limits. So additionally samples with 60 and 100 nm thick films for the 3 silicon nitride variants were produced. Because of some problems with the LoHN samples, which are explained in subsection 4.2.3, only the E_{BR} values from the 80-120 nm SiN_x films could be recorded. For the Std. Nit films the point where the SMUs went into compliance (20 mA current) is considered as E_{BR}. The average breakdown field strength values are given in table 4.3.

	Std. Nit	SiN-m	LoHN
E_{BR} [MV/cm]	9.07 ± 0.44	9.04 ± 0.72	5.73 ± 0.55

Table 4.3: Average breakdown field strength of the 3 silicon nitride variants. For Std. Nit films the E_{BR} is set to be the point when the compliance level is reached.

When the measurements were carried out it was noticeable that the electrodes with a bigger area (e.g., spot A or B) tended to fail earlier. A possible explanation for this is the defect density within the films. On a bigger area there is a higher probability that a

defect which causes failure is present.

Another observation was that the films have clearly different curves for the leakage current. To investigate this, the films were first conditioned with 3 short voltage sweeps that did not destroy them. Then a voltage sweep to cause device failure was started and the corresponding U-I curve was recorded. For comparable results, in figure 4.5, all films have a thickness of about $100\,\mathrm{nm}$ and the recorded curves arise from measurements performed at spot I in reticle $(-9 \mid 15)$. Current density variations up to $65\,\%$ occurred when various sites all across the wafer were investigated and the average film thickness was used for the calculation of the electric field. The values of the breakdown field strength, however, were modeled to graphically display the average film behavior.
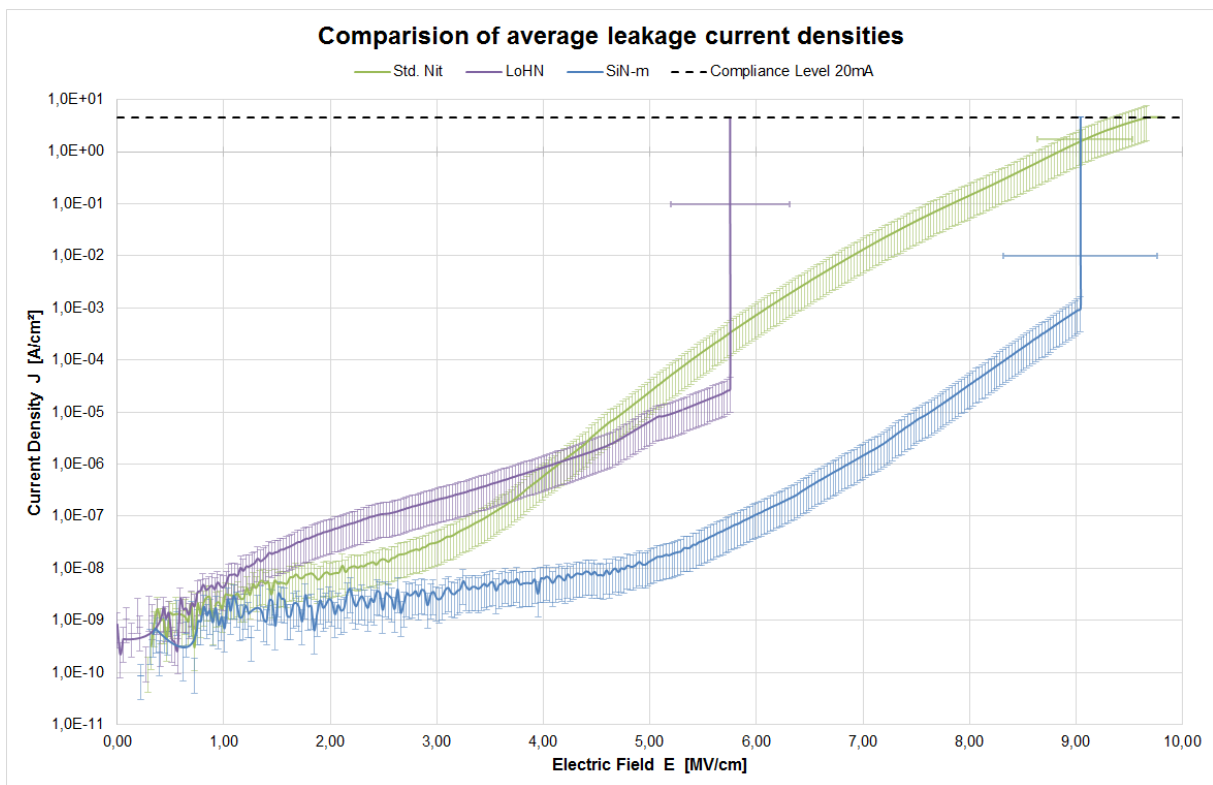
Figure 4.5: Leakage current density comparison for $100\,\mathrm{nm}$ silicon nitride films. Films were conditioned with 3 sweeps before the actual curve was recorded. The breakdown field strengths for SiN-m and LoHN were modeled to display the average film behavior as displayed in table 4.3.

4.2.3 LoHN Delamination

As mentioned above, the examination of the LoHN wafers turned out to be tricky as most of the capacitor structures failed already at very low voltages $(<4\,\mathrm{V})$. Due to that unpredictable behavior not as many U-I curves as for the other two films were recorded. The conditioning sweeps already destroyed most sample structures. Additionally some

stains, like in figure 4.6, could be seen on the surface of the LoHN samples.

(a) Magnification 5x

(b) Magnification 20x
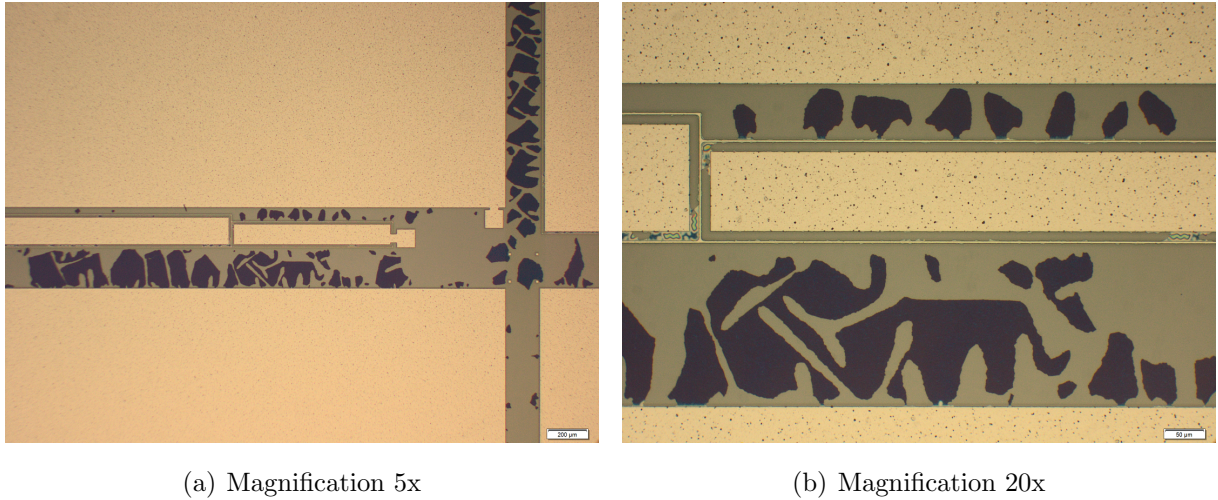
Figure 4.6: Stains on the surface of a 80 nm LoHN sample. Those stains were identified by an EDX analysis as residues of the LoHN film. This delamination was also observed on the other LoHN samples.

With the help of a light microscope it was possible to only pick electrodes for the measurements with no, or just a few of those stains touching them. Yet lots of early breakthroughs were recorded. To confirm the first guess that those stains might be aluminum residues, an EDX analysis was performed.

It turned out that the spots were not aluminum residues, but remains of the LoHN silicon nitride film (fig. 7.18). A too high compressive intrinsic stress could have caused delamination. But as for LoHN a stress of only -150 MPa was recorded, SiN-m for comparison has -200 MPa, this reason is unrealistic. A general bad adhesion between film and substrate, combined with vibrations in the wet chemical cleaning step of the production process seems more likely.

Howsoever, if the SiN_x film delaminates between the Al electrodes it is quite reasonable that it also blisters formed underneath the electrode which then distorted the electrical measurements.

4.2.4 Relative Permittivity Measurements

While the P082 wafers for the electrical measurements were passed on in the process chain, the reference films on the M118 monitoring wafers were tested on the C-V tool *CVmap 3093-AC*. This tool allows a direct measurement of the relative permittivity ε_r at a certain frequency. The wafer is held in position by a chuck, which serves as bottom contact. Then wafer and chuck are flipped over and lowered towards a small tube, which

is filled with mercury. As the wafer touches the mercury, the electric circuit is closed. Due to the dimensions of the tube, the mercury electrode is a round spot with a defined diameter. After a material is selected from a list and film thickness and desired measurement frequency are inserted, the software automatically returns the calculated ε_r value. Nine separate measurement spots, according to the 8Z9PKT layout, were evaluated for this measurement with a silicon nitride circuit model. The frequency was set to 1 MHz. For LoHN an increasing relative permittivity with film thickness was observed.

Variant	SiN-m				
Thickness [nm]	40	60	80	100	120
Avg. ε_r	7.28±0.08	6.08±0.11	7.08±0.03	6.59±0.06	7.05±0.02

Variant	Std. Nit				
Thickness [nm]	40	60	80	100	120
Avg. ε_r	6.13±0.04	5.60±0.06	6.46±0.10	3.43±0.35	4.62±0.06

Variant	LoHN				
Thickness [nm]	40	80	100	120	150
Avg. ε_r	4.44±0.33	5.60±0.28	5.80±0.26	6.38±0.07	6.60±0.13

Table 4.4: Average relative permittivity ε_r measured for the silicon nitride films, deposited in various thicknesses.

The complete dataset of this measurement can be found in the appendix subsection 7.4.3. A reason for the thickness dependence in case of the LoHN films could be that a certain film thickness is necessary before the material exhibits its bulk properties. The fluctuations of the measured values, especially for the 100 nm Std. Nit film, could be caused by a bad electrical contact of the substrate wafer during the measurement. The M118 monitoring wafer is well suited for measurements of film properties like RI, stress or thickness, but not well suited for electrical investigations, especially when the backside is not polished as in this case.

Another crucial factor is certainly also the used electrical circuit model, which was not optimized for the non-stoichiometric PECVD SiN$_x$ films on the CVmap yet.

4.3 Conduction Mechanisms

From figure 4.5 it is obvious that there is a current flowing through the material. The next thing to find out was which mechanism is responsible for conduction. Various mechanisms for dielectric films are listed in figure 1.2 in the fundamentals chapter.

As for PECVD a-SiN$_x$:H the Poole-Frenkel (PF) emission, Fowler-Nordheim (FN) tunneling and Ohmic conduction are reported, they were investigated more closely.

4.3.1 Mechanism Comparison

A graphic approach was used to determine whether or not a mechanism is active. The formulas describing the current density for each mechanism can be transformed to yield the form of a linear equation. For the FN tunneling this is shown in subsection 1.1.5, for the PF emission in subsection 1.1.6. The current density formula of the Ohmic conduction already has the right shape.

The procedure to obtain evaluable data and investigate the active conduction mechanisms consists of 4 separate steps:

1. Voltage sweeps until device failure were performed on several spots across the wafer. The average breakthrough voltage was noted.

2. Then, on a fresh spot three conditioning sweeps were carried out before the full U-I curve was recorded. Here it was important to choose a sweep range that was smaller than the average break through voltage to not cause a device failure. However, the range had to be chosen big enough that as much charges as possible were removed from the traps in the material.

3. A full sweep until the breakthrough occurred was carried out and the corresponding U-I curve was saved.

4. The recorded data was plotted according to the transformed formulas.

   - Current density J versus electric field E for Ohmic conduction
   - $\ln(J/E^2)$ versus $1/E$ for FN tunneling
   - $\ln(J/E)$ versus $\sqrt{E}$ for PF emission

   If it is possible to fit a straight line to the plotted curves, the respective conduction mechanism might be active. Still some further checks, depending on the mechanism, are suggested according to [9].

In case that the conditioning sweeps do not reach voltages high enough as necessary for step 2 above, the recorded U-I curves appear bent and it was difficult to see which mechanism is active. Also the slope of the linear fit may change and thus impede the data evaluation as presented in figure 7.20.

A straight line could be fitted to the curves obtained from all 100 nm silicon nitride variants, when a Poole-Frenkel plot was done. In the FN plots only the LoHN film exhibited a linear behavior, but the test structures failed already at low fields, which made the fitting area very short. An Ohmic behavior could just be found in the curves of the LoHN film. The corresponding curves can be found side by side in the appendix in figure 7.21.

As a conclusion of the graphic analysis, Poole-Frenkel emission is the dominant conduction mechanism in all films at strong electric fields. For LoHN it starts at $E > 4.4\,\mathrm{MV/cm}$, for Std. Nit $E > 3.6\,\mathrm{MV/cm}$ and for SiN-m $E > 5.7\,\mathrm{MV/cm}$. The results from studies which report Ohmic conduction at very low electric fields in PECVD silicon nitride can not be confirmed.[35, 23] Instead the LoHN films show a nearly linear behavior, with just little fluctuations, in the range from $2.3 - 4.8\,\mathrm{MV/cm}$. Fowler-Nordheim tunneling is obviously not active in Std. Nit and SiN-m but it might also contribute to the conduction through LoHN films.

However, due to the delamination of the LoHN films it is very likely that also other effects influence the conduction and thus the obtained results. Due to the early breakthrough of the LoHN test structures it was difficult to condition the material up to high enough fields prior the recording of the U-I curve. This is noticeable by a kink at about $5.5\,\mathrm{MV/cm}$ in the PF and FN plot of LoHN in figure 7.21.

4.3.2 Relative Permittivity and Refractive Index

To confirm that the dominant conduction mechanism is Poole-Frenkel emission, the dynamic relative permittivity and the refractive index were calculated from the obtained U-I curves, and then compared with the results from other measurement techniques. For a comparison of ε_r the values from the C-V tool CVmap are used, for the RI the values obtained from the OptiProbe. As both, CVmap and OptiProbe, measure the wafers according to the 8Z9PKT layout, the reticles selected for the electric testing were chosen to be close to the measurement sites. Which reticles correspond with which measurement site can be extracted from table 4.5.

Site	x	y
1	-10; -9	23; 24
2	-4; -3; -2	23; 24; 25
3	3; 4; 5	23; 24; 25
4	3; 4; 5	14; 15; 16
5	-2; -1; 0	14; 15; 16
6	-10; -9; -8	14; 15; 16
7	-10; -9; -8	6; 7; 8
8	-1; 0; 1	6; 7; 8
9	8; 9; 10	6; 7; 8

Table 4.5: Measurement sites of the 8Z9PKT layout correlated with reticle positions using the coordinate system defined in figure 4.3 as (x | y) position.

The obtained curves were then PF plotted and a linear fit was performed in the respective region. With the slope of the fitline, the dynamic relative permittivity was calculated using equation 1.21. With the simple relation $\varepsilon_r = n^2$, the (high frequency) refractive index

was calculated as described at the end of fundamentals section 1.1.6. A comparison of the results obtained from the electrical measurement with the ones from the CVMap and the OptiProbe, respectively, can be found in tables 4.6 and 4.7 .

	Std.Nit		SiN-m	
Filmthickness [nm]	60	100	60	100
ε_r (PF emission)	6.07±0.44	4.57±0.15	3.57±0.15	3.45±0.57
ε_r (CVMap)	5.60±0.06	3.43±0.35	6.08±0.11	6.59±0.06
RI (PF emission)	2.462±0.094	2.138±0.035	1.890±0.040	1.853±0.147
RI (OptiProbe)	1.970±0.005	2.037±0.009	1.867±0.002	1.930±0.003

Table 4.6: Comparison of ε_r and RI values for Std. Nit and SiN-m. As described in the text the CVMap data is likely to be inaccurate.

	LoHN		
Filmthickness [nm]	40	100	150
ε_r (PF emission)	4.04±0.99	7.02±2.15	36.49±5.18
ε_r (CVMap)	4.44±0.33	5.80±0.26	6.60±0.13
RI (PF emission)	1.998±0.225	2.623±0.391	6.029±0.433
RI (OptiProbe)	1.854±0.010	1.918±0.009	1.873±0.012

Table 4.7: Comparison of ε_r and RI values for LoHN. As described in the text the CVMap data is likely to be inaccurate.

Concerning the values for the relative permittivity a clear difference between values obtained from the PF theory and the ones from the CVMap can be seen. The reason for this is on the one hand the frequency dependence of ε_r. While the CVMap measures at $1\,\mathrm{MHz} = 10^6\,\mathrm{Hz}$, the detrapping of the charges in the PF model happens much faster, at about $10^{15}\,\mathrm{Hz}$. The other reason is that the slope of the fitline changes when the material is not conditioned properly. The resulting hump in the measurement curve then has to be compensated by adjusting the fit parameters. This causes a change of slope as the area for the fit is made bigger or smaller.

The RI values from the OptiProbe, however, are displayed at a wavelength of $670\,\mathrm{nm}$, so $\approx 4.5 \cdot 10^{14}\,\mathrm{Hz}$. For the SiN-m films the RI values show a good match and thus the PF emission can be confirmed as dominant conduction mechanism. For the Std. Nit films this is true as well, although in case of the thin films another mechanism seems to be active as well as a clear difference is noted. This is consistent with the studies that report the PF emission as the dominant process at high fields at room temperature and above[43, 22] but also mention FN-like characteristics which could result from trap-assisted tunneling[2].

Nevertheless, the LoHN films only show a RI correspondence with the thin $40\,\mathrm{nm}$ film, the others are far off. From this the conclusion can be drawn that here the PF emission is not the dominant conduction mechanism, although the PF plot shows a linear behavior at

high electric fields. The bad adhesion, however, which causes film delamination, is likely to influence the measured current and thus the slope of the line fitted to the data. As during the time of this thesis no LoHN film without any delaminations could be produced, this could not be further investigated.

4.3.3 Trap Depth

To be able to calculate the depths of the traps, which are defined in the PF theory, it was necessary to perform some measurements at elevated temperatures. A straight line was then fitted through the datapoints which were displayed in the form of an Arrhenius plot. The value of the slope was then inserted into formula 1.26 to calculate the trap depth. Due to time issues only the 60 nm films of SiN-m and Std. Nit film could be investigated like this. As temperature steps 60, 90, 130 and 190 °C were chosen.

Masaki et al.[23] found that for $SiN_x:H_y$ films the temperature dependence of the conduction at high electric fields can be divided into 3 regions: a high temperature activated region above 80 °C, another activated region between 80 and -50 °C and a weakly activated region at lower temperatures. The measurements carried out here are thus located in the high temperature region.

For the Std. Nit films the change of leakage current with increasing temperature was analyzed in the electric field region from 3.5 to 7.0 MV/cm, as for this fields the PF plot exhibits the linear behavior. The corresponding Arrhenius plot is presented in figure 7.22. Likewise for the SiN-m film but for datapoints from 4.9 to 7.7 MV/cm. The average dynamic relative permittivity ε_d from the measurements at high temperatures are 3.514 for the Std. Nit film, and 2.54 for the SiN-m film. With these values the voltage barrier, that must be overcome can be calculated, but these activation energies are dependent on the applied field. For the electric fields, where the linear region starts in the PF plot, values of 0.75 eV (@3.45 MV/cm for Std. Nit) and 1.06 eV (@4.92 MV/cm for SiN-m) were calculated.

The actual trap depth in zero applied field is then obtained by a linear fit through the activation energies at their respective electric field values, as shown in figure 7.23. Results for this are:

$$\begin{aligned} \text{Std. Nit:} \quad & 0.45 \pm 0.05\,\text{eV} \\ \text{SiN-m:} \quad & 0.59 \pm 0.07\,\text{eV} \end{aligned}$$

The error of 11 % arises as multiple spots with different electrode areas were measured across the wafer. A better approach would be to just investigate a small area on a wafer and always perform the measurements on the same spot sizes.

Referred to figure 4.5 this results make sense as it explains why the Std. Nit films already

show a leakage current at lower electric fields.

Traps with an energy between 0.50-0.90 eV below the conduction band of silicon nitride have been reported by Kendall[16]. Those traps arise due to stacking faults when also some small crystalline areas form during deposition. As the process gases are N_2, NH_3 and SiH_4, not only pure Si and N radicals are formed inside the plasma but also derivatives from that molecules. Some of those radicals still have hydrogen bonded to them and as the mobility during deposition is limited, a material with incorporated hydrogen but also silicon and nitrogen dangling bonds is created. While the H-atoms form, or more specifically stay in their bonds with Si and N, the dangling bonds can act as trapping centers.

In a first-time applied electric field the distribution, density and occupation of the traps change as suggested in section 4.2.1. During a heat treatment it is conceivable that some bonds are modified and former dangling bonds disappear and thus the overall trap density decreases.

4.4 Further Measurements

As last step of the electrical measurements some experiments were performed, to find out which of the factors from the production process affect conductivity, and if a connection to the incorporated hydrogen can be seen.

4.4.1 Std. Nit DoE

For this purpose a full factorial DoE with 2 centerpoints was carried out, based on the recipe for the Std. Nit film. To obtain meaningful results, the variations of the factors were chosen to be close to the allowed maximum offset-values in regular production: RF generator power ± 60 W, spacing ± 35 mils and silane flow ± 20 sccm.

Based on the experiences from the previous sets of experiments, the deposition time was chosen to yield thicknesses around 70 nm.

Like for the electrical measurements before, all films were deposited inside the same deposition chamber of a Precision 5000 system. Also the rest of the process to create measurable MIM structures was identical with the previous experiments (P082 substrate wafer, M118 monitor wafers with reference films, AlSiCu top electrode, G0900 reticles). The thickness and RI were results from the OptiProbe, for the hydrogen content the FTIR spectra were evaluated with the Matlab script mentioned in section 3.2.

Number of experiment	Std. Nit DoE			
	RF power [W]	Spacing [mils]	SiH$_4$ [sccm]	N$_2$ [sccm]
1	750	665	305	4000
2	750	665	265	4000
3	750	595	305	4000
4	750	595	265	4000
5	630	665	305	4000
6	630	665	265	4000
7	630	595	305	4000
8	630	595	265	4000
9	690	630	285	4000
10	690	630	285	4000

Table 4.8: Designed experiment for Std. Nit on the Precision 5000 within the electrical measurements. Thicknesses are expected to be around 70 nm.

4.4.2 Measurement Sites

The U-I curves were again recorded on the *S-Matrix* but now the temperature was held constant at 25 °C. For comparable U-I curves, the reticles attributed to the 8Z9PKT sites 5,6 and 8 were examined on pads E and I. The average leakage current between 3 and 8 MV/cm for each sample wafer is presented in figure 4.7. As the curves for DoE 9 and 10 originate from films deposited with the same recipe, they are good indicators for possible
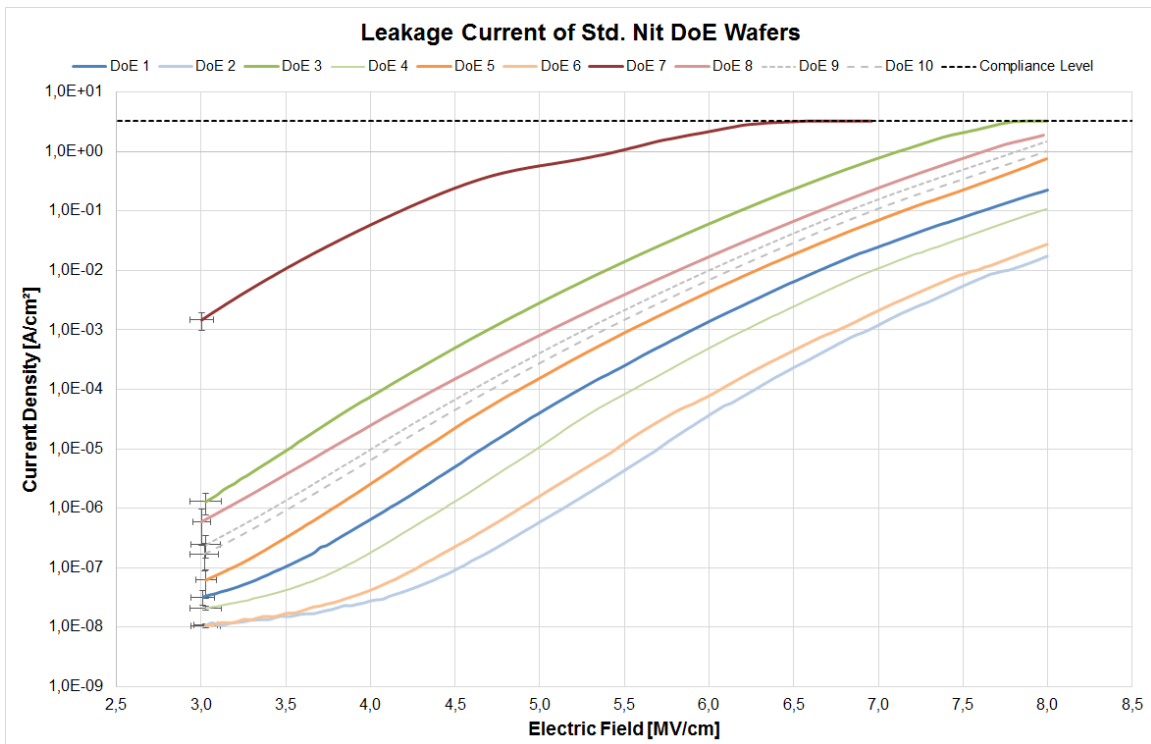

Figure 4.7: Average leakage current curves of the sample films from the Std. Nit DoE.

fluctuations in the deposition process itself.

The DoE settings are shown in the color of the respective leakage current curve and in terms of low (0) and high (1) settings on the side. This makes it easier to see that whenever the silane flow is on a high setting (bold colors), the leakage current is higher than for the film deposited with a lower silane flow rate.

Films which are deposited with a high setting for the electrode spacing yield smaller leakage currents than

	RF Pwr	Spac.	SiH4
DoE 1	1	1	1
DoE 2	1	1	0
DoE 3	1	0	1
DoE 4	1	0	0
DoE 5	0	1	1
DoE 6	0	1	0
DoE 7	0	0	1
DoE 8	0	0	0
DoE 9	x	x	x
DoE 10	x	x	x

those deposited with a low setting. Concerning the RF generator power also the films produced with a high power exhibit better insulating properties than the films with identical settings but lower RF power. This stands in contrast to [27] where for LPCVD silicon nitride films, which were created in a pure nitrogen plasma at temperatures below 300 °C, a higher leakage current is reported for films grown under high RF power.

4.4.3 Influence of Hydrogen

In the fundamentals section 1.4.5 about hydrogen content, an equation that describes a relation between the ratio of SiH/NH and the index of refraction is given (eq. 1.36).
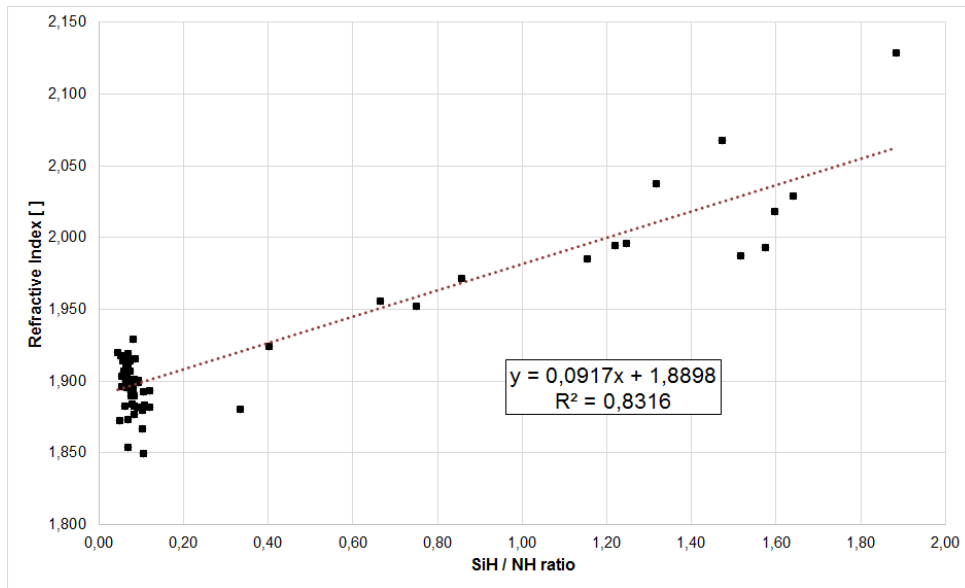
Figure 4.8: SiH/NH ratio VS. refractive index for all deposited SiN$_x$ films. Formula 1.36 to calculate SiH/NH from n (or vice versa) is obviously also applicable for the low hydrogen SiN-m and LoHN films.

The underlying research[10] however did not investigate films with intentionally low SiH content, as this is the case for the SiN-m and LoHN films within this work. To check if that formula from literature is also applicable on the low-H SiN$_x$ films, the SiH/NH ratios

from all wafers of the electrical measurements were plotted versus the RI at 670 nm.

The straight line fit through the data points in figure 4.8 correlates with the equation from literature, but big fluctuations for the films with low SiH concentrations are visible. For the Std. Nit films, which have a clear SiH peak and have thus a SiH/NH ratio > 0.2, a variance is noted as well.

A possible reason for this is certainly that in order to produce films with a varying SiH/NH ratio the process parameters have to be varied. This simultaneously also changes the stoichiometry of the film and thus hinders a good RI measurement as the underlying mathematical models are optimized for a specific film (stoichiometry). The fluctuations of the SiN-m and LoHN datapoints can occur because of problems when evaluating FTIR spectra with small peaks which are additionally distorted by CO_2 influences.

In terms of hydrogen-related leakage current, a straight forward approach is to plot the data and look for systematic correlations. As all PECVD silicon nitride films have a total hydrogen concentration of about 11-15 at% it is convenient to plot the SiH and NH bond concentrations separately. For the y-axis the leakage current density at 4.9 MV/cm was chosen as here (except for the DoE 7 wafer) all curves in figure 4.7 have comparable slopes and the PF emission is active. A connection between H-bond type and leakage current can be observed for a semilogarithmic plot shown in figure 4.9.
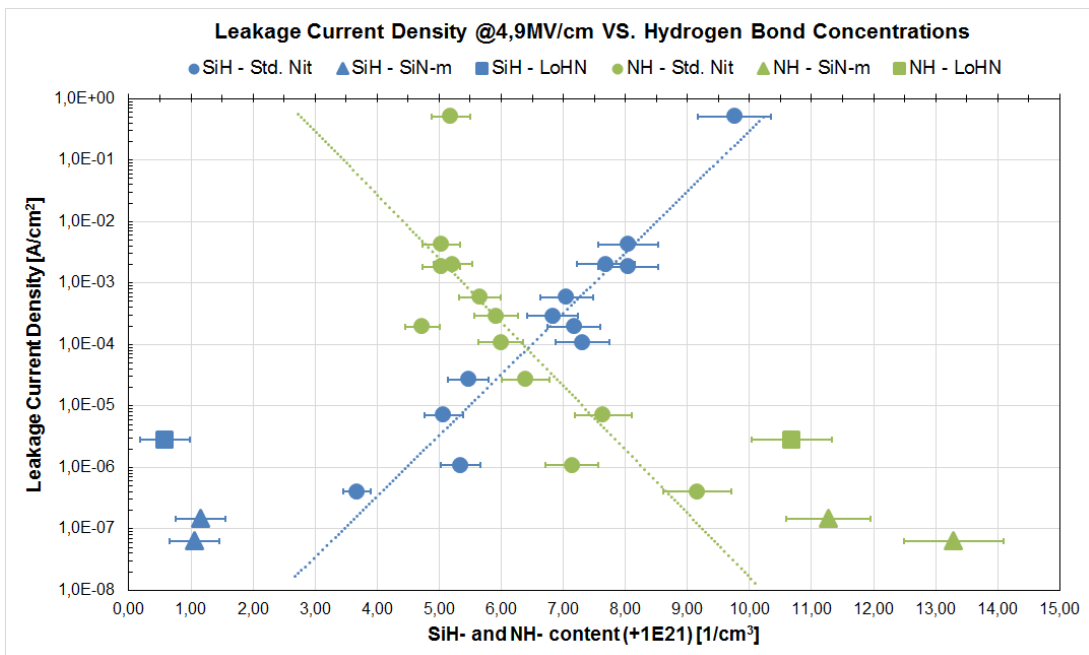

Figure 4.9: Connection between hydrogen bond type and leakage current. A higher Si-H, and thus Si content signifies more possible traps from Si dangling bonds which then contribute to the conduction.

This logarithmic relation between rise of SiH content and increase of leakage current can

be explained with an increase of the trap density when the stoichiometry shifts to Si-rich films. When SiH$_4$ splits up in the plasma not only Si radicals and 2H$_2$ molecules are formed but also other derivatives of the original molecule. Due to mobility reasons also silicon and nitrogen dangling bonds are incorporated in the silicon nitride film along with remaining Si-H bonds. Those Si dangling bonds act as traps and their number increases as more silicon is present in the stoichiometry. This additional traps not only contribute to the conduction when their height is lowered according to the PF theory in an electric field, but if located close enough to each other the charges can tunnel from trap to trap until they reach a low enough one from where they can reach the conduction band. The amount of hydrogen bonded to either Si or N shows which of them is the prevalent sort of atom in the material. A high number of Si-H bonds means a high number of Si atoms and thus more Si dangling bonds and traps, respectively. Nevertheless, according to Warren et al. it is likely that not only the simple Si dangling bond alone is the charge trapping center responsible for the current conduction[41].

When exposed to ultraviolet light, silicon dangling bonds are reported to be annihilated. Warren et al. suggest that molecular H$_2$, which they expect to be located in voids of the nitride matrix, cracks apart due to the irradiation process. The atomic hydrogen can then diffuse and passivate a K^0 center as the necessary energy to crack H$_2$ in vacuum (4.52 eV) is present in the spectrum of broad-band UV light. However, this molecular hydrogen, if not present directly in the precursor gases as diluent, needs to form first. It is thinkable that individual hydrogen atoms, which are able to diffuse through the material, recombine to form hydrogen molecules. When entrapped in voids those molecules can create pressures high enough to crack open steel where this effect is known as hydrogen induced cracking (HIC).[21] Assuming a recombined H$_2$ molecule in a void formed by several dangling bonds, the pressure could distort the nitride matrix and thus affect the charge trapping abilities of the close dangling bonds.

Already at room temperature hydrogen has a high diffusivity. The decreasing leakage current after a heat treatment at 190 °C, like in figure 7.17, could thus be explained by the annihilation of Si dangling bonds by hydrogen atoms. For a confirmation of this proposition the bonded hydrogen concentration must be measured prior and after the heat treatment but this was not done within this work.

With equation 1.36 it is furthermore possible to calculate the stoichiometry of the films once the SiH/NH ratio is known. This is done for the wafers from the Std. Nit DoE and the obtained values are plotted against the current density at 4.9 MV/cm. As Si$_3$N$_4$ is the thermodynamic most stable form, a x-value in SiN$_x$ smaller 1.33 denotes Si-rich silicon nitride. A clear connection between stoichiometry and leakage current behavior is observed.
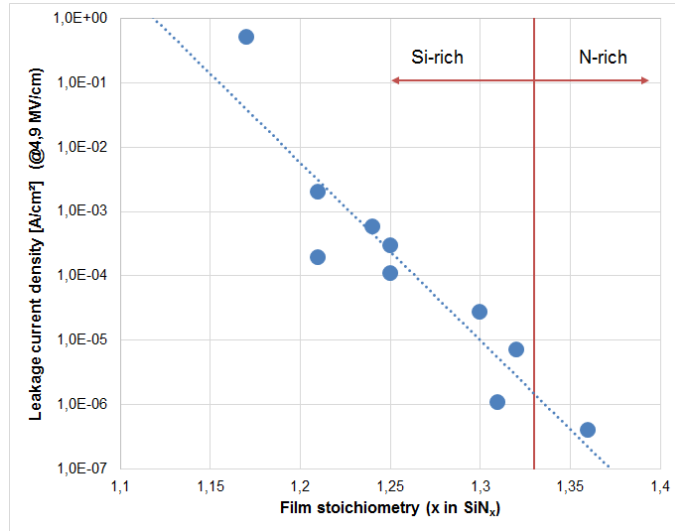
Figure 4.10: Connection between stoichiometry and leakage current density in Si-rich SiN_x films. The datapoints originate from the wafers of the Std. Nit DoE.

4.4.4 Possible Implementation for Production

The complete process, from the initial film deposition step until the finished wafer with a defined test structure on it and ready for an electrical measurement, takes several days. The measurement of the film properties on the OptiProbe on the contrary only takes a few minutes. Due to that it would be a huge benefit if from the measurement of the refractive index already information about the electric behavior could be obtained. Figure 4.11 shows a tendency that this approach works.
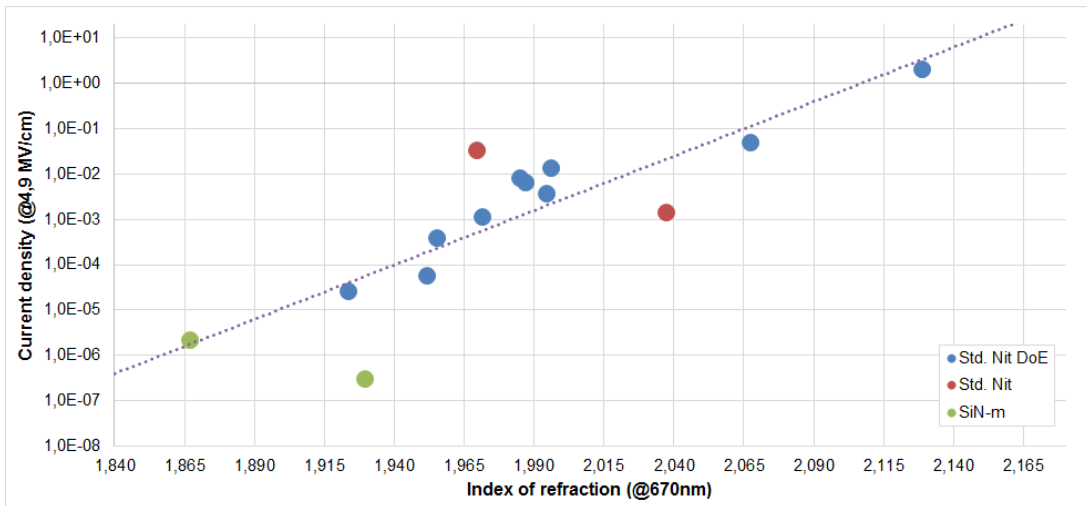

Figure 4.11: Connection between refractive index and current density for SiN_x films.

However, more samples with precisely defined test conditions have to be investigated to be able to draw a sound conclusion for this topic.

5 Conclusion and Outlook

5.1 Designed Experiments

Four silicon nitride variants, called Std. Nit, SiN-m, LoHN and CuNit, were deposited in Plasma-Enhanced Chemical Vapor Deposition (PECVD) reactors. A comparison between those variants can be found in the beginning of chapter 2, details about the used reactors in section 1.3.2.

The determination of the relations between changeable factors and measureable film parameters in the silicon nitride production process was done by performing designed experiments (DoEs). As there is not theoretical model available yet that can describe the complex PECVD system, these DoEs are the only way to gain knowledge about the deposition process and how film properties (e.g., refractive index, intrinsic stress, . . .) can be changed.

CEDA, the software used in this work for the experimental design, proved to be a valuable aid as the number of required samples could be reduced by choosing for example a D-optimized design (see section 2.1). It turned out that regarding the deposition rate a linear regression model was sufficient, for other film parameters (e.g., intrinsic stress, Si-H concentration, . . .) at least a 3-step variation of factor settings is needed to apply a quadratic regression model as presented in figure 7.1.

The optimized regression models made it possible to program deposition recipes onto both, the lamp-heated and resistance heated CVD systems, which yield hydrogenated non-stoichiometric silicon nitride layers with film properties that match the desired specifications. Nevertheless, a lower limit for the incorporated hydrogen content was found at approximately $13 \, \mathrm{at\%}$ for the low-hydrogen (LoHN) films due to the nature of the PECVD deposition process as described in section 1.1.1.

A further reduction of the H content could be achieved by varying the substrate temperature and the pressure within another DoE based on the actual optimized recipes. At elevated temperatures the hydrogen diffusivity increases and more byproducts (H_2) are removed before they can get trapped in voids at lower pressures.

With the DoEs also the maintenance of the double-chamber CVD systems (Producer) might be improved. A change of film parameters, while keeping the deposition recipe constant, can be traced back to an unequal distribution of the process gases. This in turn

is related to the clogging of the showerhead and gas pipes over time. Which of the two stations inside the Producer chamber needs maintenance can thus be detected by which wafer was coated with less process gas according to the DoE.

5.2 Tuning In-Line Measurements

Refractive index n, extinction coefficient k and film thickness d were determined from optical measurements on the so-called OptiProbe. These film properties cannot be measured directly but n, k and d are used as variables in a fitting procedure to find their values. The mathematical model, based on Cauchy's equation, needs initial fit values which alter, depending on the material of the sample. As PECVD silicon nitride is off-stoichiometric it was necessary to optimize the measurement recipe on the OptiProbe which is explained in section 3.1.2. A combination of the beam profile reflectometer (BPR) and the spectroscopic ellipsometer (SE) yielded plausible results (figure 3.3). However, if the increasing refractive index with the film thickness is caused by a changing density of the film or if the mathematical model has to be further adapted will be examined in future sets of experiments.

Initial hydrogen content measurements showed inconsistencies between shape of the FTIR spectrum and calculated H-content when CO_2 influences and only a few Si-H bonds were present (figure 3.6). Hence a Matlab program was created to correct this behavior. When more wafers were measured after each other, the CO_2 peaks became stronger and also H_2O absorption lines appeared in the spectrum. This suggests the assumption that the nitrogen purging inside the spectrometer was disturbed by the movements of the handler that transported the wafers. A higher nitrogen flow for the purging could possibly eliminate that problem.

5.3 Electrical Characterization

After the deposition recipes of the SiN_x variants were adjusted to yield films with the desired properties, highly doped Si wafers were coated with the films for the electrical characterization. AlSiCu was sputtered on top and the device structure was created in a lithography/etching process as described in section 4.1.1.

The first voltage sweep revealed a charging effect of the material (figure 4.4) which can be attributed to trapped charges which contribute to the current as a certain electric field is applied. As not all traps are filled up with charges again, a lower leakage current can be observed in the following sweeps. The Poole-Frenkel emission could be confirmed as the dominant conduction mechanism for Std. Nit and SiN-m, supposedly a trap-assisted tunneling effect is responsible for the refilling of the traps with charges. However, for

the LoHN films none of the tested mechanisms was fitting to the measured data, this is because the films were afflicted with delamination problems that caused unpredictable electrical responses (figures 4.6 and 7.18).

An increasing leakage current could be observed with a rising number of Si-H bonds. A high Si-H content in turn denotes Si-rich films which make the Si dangling bonds the most likely dominant charge trapping centers. According to Warren et al.[39] this dangling bond lies in the middle of the nitride band gap. From an Arrhenius plot a trap energy level of $0.45\pm0.05\,\text{eV}$ for Std. Nit and $0.59\pm0.07\,\text{eV}$ for SiN-m was extracted. As this indicates a level more closely to the conduction band it is reasonable to think of a not simple Si dangling bond.[41] A possible explanation might be that molecular hydrogen, entrapped in voids inside the SiN_x matrix, somewhat distorts the lattice and thus influences the energy level of the dangling bond.

As the refractive index rises with the silicon content it was furthermore possible to show a connection between leakage current and refractive index (figure 4.11). This will be further investigated as it would allow a fast estimation of the electrical characteristics already during the production process.

6 Bibliography

[1] P. Alpuim, P. Ferreira, V. Chu, and Joao P. Conde. Electronic transport in low-temperature silicon nitride. *Journal of Non-Crystalline Solids*, 299-302(PART 1):434–438, 2002.

[2] P. C. Arnett and D. J. Dimaria. Contact currents in silicon nitride. *Journal of Applied Physics*, 47(5):2092–2097, 1976.

[3] Peter W. Atkins and Ronald S. Friedmann. *Molecular Quantum Mechanics*. Oxford University Press, fifth edit edition, 2010.

[4] Daniel Benoit, Pierre Morin, and Jorge Regolini. Determination of silicon nitride film chemical composition to study hydrogen desorption mechanisms. *Thin Solid Films*, 519(19):6550–6553, 2011.

[5] Michael Blech, Abdelazize Laades, Carsten Ronning, Bernd Schröter, Christian Borschel, Daniel Rzesanke, and Alexander Lawerenz. Detailed Study of PECVD Silicon Nitride and Correlation of Various Characterization Techniques. *24th European Photovoltaic Solar Energy Conference and Exhibition*, pages 507–511, 2009.

[6] R. Brendel. The concept of effective film thickness for the determination of bond concentrations from IR spectra of weakly absorbing thin films on silicon. *Journal of Applied Physics*, 69(11):7395–7399, 1991.

[7] C.Y. Chang, F.C. Tzeng, C.T. Chen, and Y.W. Mao. Hot-carrier memory effect in an Al/SiN/SiO2/Si MNOS diode due to electrical stress. *Electron Device Letters, IEEE*, 6(9):448–449, 1985.

[8] Kuan Yew Cheong, Jeong Hyun Moon, Hyeong Joon Kim, Wook Bahng, and Nam Kyun Kim. Current conduction mechanisms in atomic-layer-deposited HfO2 /nitrided SiO2 stacked gate on 4H silicon carbide. *Journal of Applied Physics*, 103(8):1–8, 2008.

[9] Fu-Chien Chiu. A Review on Conduction Mechanisms in Dielectric Films. *Hindawi Publishing Corporation*, 2014:18, 2014.

[10] W. a. P. Claassen. Characterization of Plasma Silicon Nitride Layers. *Journal of The Electrochemical Society*, 130(12):2419, 1983.

[11] Badih El-Kareh. *Fundamentals of Semiconductor Processing Technology.* Springer Science + Business Media, 1995.

[12] Andreas Gehring. *Simulation of Tunneling in Semiconductor Devices.* PhD thesis, Vienna University of Technology, 2003.

[13] S. Hampshire. Silicon nitride ceramics – review of structure, processing and properties. *Journal of Achievements in Materials and Manufacturing Engineering*, 24(1):43–50, 2007.

[14] Matthias Haselmann. Optical Diagnostics of High Density Plasma Chemical Vapor Deposition Processes in Semiconductor Wafer Production. Master's thesis, Graz University of Technology, 2013.

[15] Samares Kar. *High Permittivity Gate Dielectric Materials.* Springer-Verlag, 2013.

[16] E. J. M. Kendall. Trapping Levels in the Silicon-Silicon Nitride System. *Physica Status Solidi (B)*, 32:763–768, 1969.

[17] Wilhelm Kleppmann. *Versuchsplanung - Produkte und Prozesse optimieren.* Carl Hanser Verlag, 8. edition, 2013.

[18] W. R. Knolle and J. W. Osenbach. The structure of plasma-deposited silicon nitride films determined by infrared spectroscopy. *Journal of Applied Physics*, 58(3):1248–1254, 1985.

[19] W. A. Lanford and M. J. Rand. The hydrogen content of plasma-deposited silicon nitride. *Journal of Applied Physics*, 49(4):2473–2477, 1978.

[20] W. S. Lau, S. J. Fonash, and J. Kanicki. Stability of electrical properties of nitrogen-rich, silicon-rich, and stoichiometric silicon nitride films. *Journal of Applied Physics*, 66(6):2765–2767, 1989.

[21] John C. Lippold. *Welding Metallurgy and Weldability.* John Wiley & Sons, Inc., 2014.

[22] A. J. Lowe, M. J. Powell, and S. R. Elliott. The electronic properties of plasma-deposited films of hydrogenated amorphous SiNx (0<x<1.2). *Journal of Applied Physics*, 59(4):1251–1258, 1986.

[23] Yuichi Masaki, Roderick A. G. Gibson, and Peter G. LeComber. Structural and electrical properties of SiNx:H films. *Journal of Applied Physics*, 73(10):5088–5094, 1993.

[24] Yoshio Nishi and Robert Doering. *Handbook of Semiconductor Manufacturing Technology*. CRC Press, 2000.

[25] Milton Ohring. *Material Science of Thin Films*. Elsevier Science, 2002.

[26] J.W. Osenbach, J.L. Zell, and L.J. Howard. Electrical, physical, and chemical characteristics of plasma-assisted chemical-vapor deposited semi-insulating a-SiN:H and their use as a resistive field shield for high voltage integrated circuits. *Journal of Applied Physics*, 67(11):6830, 1990.

[27] E. Paloura, K. Nauka, J. Lagowski, and H. C. Gatos. Silicon nitride films grown on silicon below 300 degree C in low power nitrogen plasma. *Applied Physics Letters*, 49(2):97, 1986.

[28] E. C. Paloura, J. Lagowski, and H. C. Gatos. Growth and electronic properties of thin Si3N4 films grown on Si in a nitrogen glow discharge. *Journal of Applied Physics*, 69(7):3995–4002, 1991.

[29] A. V. Shaposhnikov, I. P. Petrov, V. A. Gritsenko, and C. W. Kim. Electronic band structure and effective masses of electrons and holes in the α and β phases of silicon nitride. *Physics of the Solid State*, 49(9):1628–1632, 2007.

[30] Arthur Sherman. *Chemical vapor deposition for microelectronics: principles, technology, and applications*. Noyes Publications, New York, 1987.

[31] John G. Simmons. Poole-Frenkel effect and Schottky effect in metal-insulator-metal systems. *Physical Review*, 155(3):657–660, 1967.

[32] Michael Stadtmüller. *Charakterisierung aus der Gasphase abgeschiedener Dielektrika für die Halbleitertechnologie*. PhD thesis, Universität der Bundeswehr, 1993.

[33] Lee Stauffer. Fundamentals of Semiconductor C-V Measurements. 2009.

[34] Hui-Chia Su, Chih-Hao Lee, Ming-Zhe Lin, and Tzu-Wen Huang. A Comparison Between X-ray Reflectivity and Atomic Force Microscopy on the Characterization of a Surface Roughness. *Chinese Journal of Physics*, 50(2):291–300, 2012.

[35] S. M. Sze. Current transport and maximum dielectric strength of silicon nitride films. *Journal of Applied Physics*, 38(7):2951–2956, 1967.

[36] Simon M. Sze and K. Ng Kwok. *Physics of Semiconductor Devices*. Wiley & Sons, 3rd edition, 2006.

[37] Tran Quang Trung, Stuchlik Jiri, Ha Stuchlikova, Le Khac Binh, Nguyen Nang Dinh, Huynh Kim Khuong, Phan Thi Nhu Quynh, and Nguyen Thi Huynh Nga. The effects of hydrogen dilution on structure of Si:H thin films deposited by PECVD. *Journal of Physics: Conference Series*, 187:012035, 2009.

[38] John L. Vossen and Werner Kern. *Thin film processes*. Academic Press, New York, 1978.

[39] W. L. Warren, J. Kanicki, J. Robertson, and P. M. Lenahan. Energy level of the nitrogen dangling bond in amorphous silicon nitride. *Applied Physics Letters*, 59(14):1699–1701, 1991.

[40] W. L. Warren, J. Robertson, and J. Kanicki. Si and N dangling bond creation in silicon nitride thin films. *Applied Physics Letters*, 63(19):2685–2687, 1993.

[41] W. L. Warren, C. H. Seager, J Kanicki, M. S. Crowder, and E. Sigari. Ultraviolet light induced annihilation of silicon dangling bonds in hydrogenated amorphous silicon nitride films. *Journal of Applied Physics*, 77(11):5730–5735, 1995.

[42] Wentao Xu, Toshiyuki Fujimoto, and Isao Kojima. Preparation and characterization of smooth and dense silicon nitride thin films. *Thin Solid Films*, 394(1-2):109–114, 2001.

[43] S. Yokoyama, N. Kajihara, M. Hirose, Y. Osaka, T. Yoshihara, and H. Abe. Characterization of Plasma-Deposited Silicon Nitride Films. *Journal of Applied Physics*, 51(10):5470–5474, 1980.

7 Appendix

7.1 CEDA Results of the Designed Experiments

The adjusted response graphs and the significant terms within the regression models are directly exported from CEDA, the used DoE software.

SiN-m on Producer (CxZ)
Figure 7.1 ... Adjusted response graph for SiN-m on the Producer system, chamber A1
Figure 7.2 ... Adjusted response graph for SiN-m on the Producer system, chamber A2
Figure 7.3 ... Significant Terms for SiN-m on Producer, chambers A1 and A2

SiN-m on Precision 5000 (LH)
Figure 7.4 ... Adjusted response graph for SiN-m on Precision 5000
Figure 7.5 ... Significant Terms for SiN-m on Precision 5000

LoHN on Producer (CxZ)
Figure 7.6 ... Adjusted response graph for LoHN on Producer, chamber A1
Figure 7.7 ... Significant Terms for LoHN on Producer, chamber A1

CuNit on Precision 5000 (CxZ)
Figure 7.8 ... Adjusted response graph for CuNit on Precision 5000
Figure 7.9 ... Significant Terms for CuNit on Precision 5000

Film Roughness
Figure 7.10 ... AFM images and roughness calculation for a 40 nm LoHN film
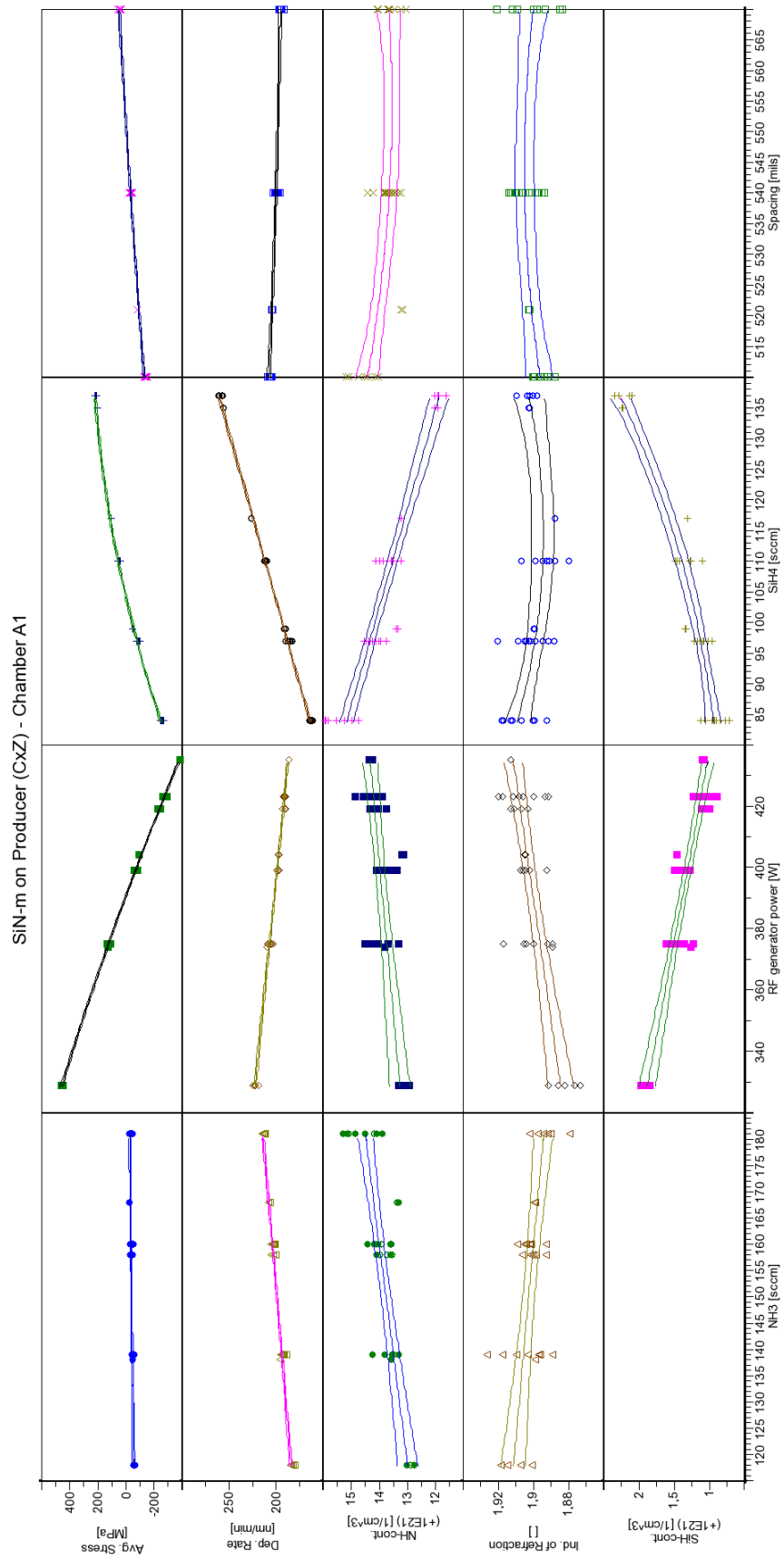Figure 7.11 ... AFM images and roughness calculation for a 120 nm Std. Nit film

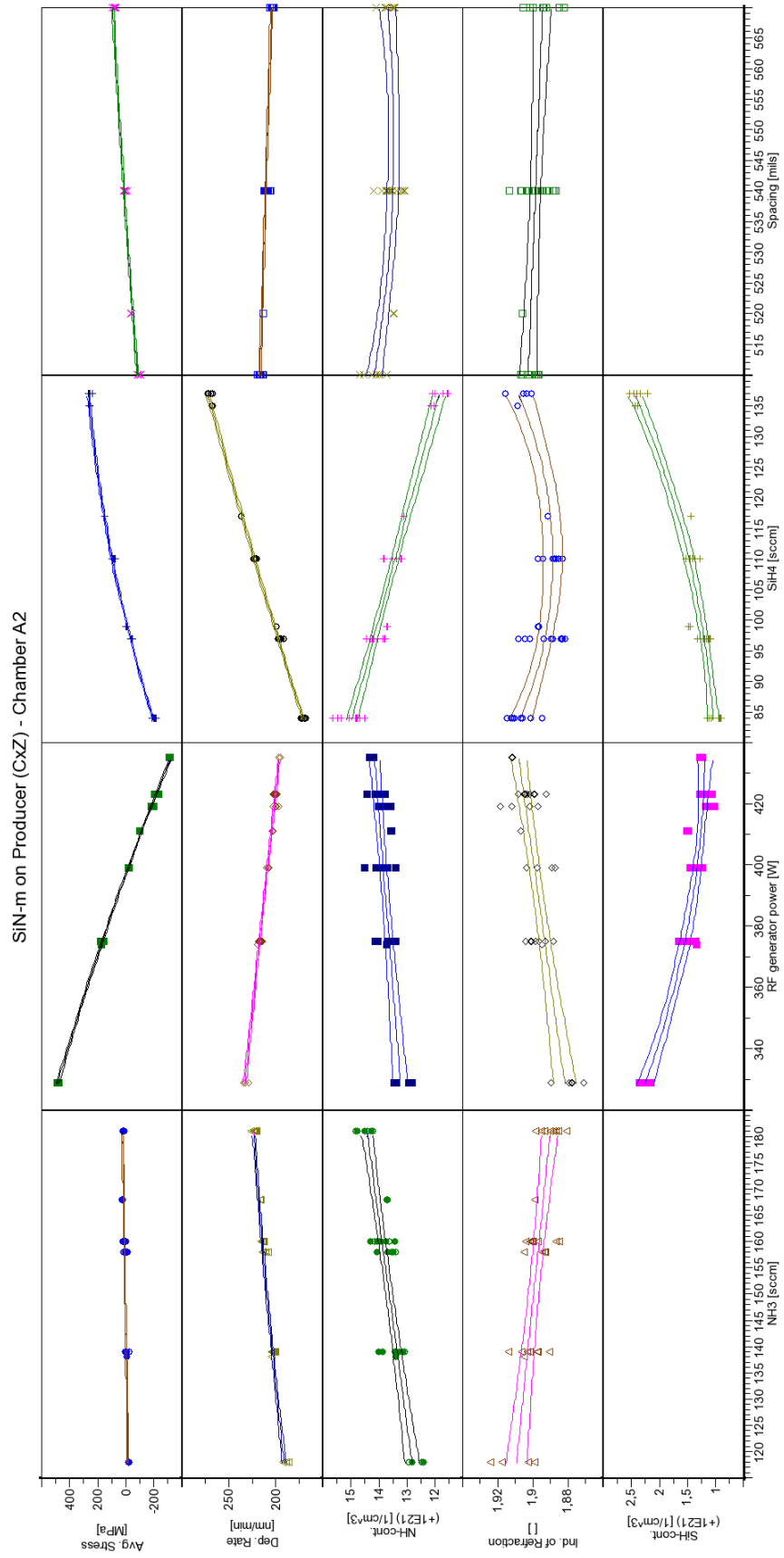Figure 7.1: Adjusted response graph for SiN-m on Producer A1. Confidence level is set to be 0.95.

Figure 7.2: Adjusted response graph for SiN-m on Producer A2. Confidence level is set to be 0.95.

SiN-m - Term Significance - Chamber A1

Term	Dep. Rate	Refr. Index	Avg. Stress	SiH	NH
Constant	0,173905 / 1 df / In	0,663357 / 1 df / In	0,0335176 / 1 df / In	6,14419e-08 / 1 df / In	0,0146712 / 1 df / In
SiH4	9,92951e-09 / 1 df / In	0,0534472 / 1 df / In	0,361357 / 1 df / In	8,18765e-07 / 1 df / In	2,71558e-05 / 1 df / In
NH3	0,623017 / 1 df / In	0,0367552 / 1 df / In	0,00111208 / 1 df / In	0,154373 / 1 df / Out	0,0103359 / 1 df / In
RF	0,148809 / 1 df / In	0,656259 / 1 df / In	0,960075 / 1 df / In	1,47685e-11 / 1 df / In	0,761904 / 1 df / In
Spacing	0,112426 / 1 df / In	0,122639 / 1 df / In	0,00282721 / 1 df / In	0,303375 / 1 df / Out	0,0274077 / 1 df / In
SiH4^2	0,500441 / 1 df / Out	0,00549822 / 1 df / In	6,43929e-15 / 1 df / In	0,000394513 / 1 df / In	0,305712 / 1 df / Out
NH3 * SiH4	6,90361e-06 / 1 df / In	0,223288 / 1 df / Out	2,24351e-05 / 1 df / In	0,150486 / 1 df / Out	0,466961 / 1 df / Out
RF * SiH4	0,00104554 / 1 df / Out	0,0192656 / 1 df / In	0,00000 / 1 df / In	7,43849e-15 / 1 df / In	0,00134745 / 1 df / In
SiH4 * Spacing	0,474011 / 1 df / Out	0,0830736 / 1 df / In	0,526359 / 1 df / Out	0,305771 / 1 df / Out	0,209977 / 1 df / Out
NH3^2	0,612588 / 1 df / Out	0,420334 / 1 df / Out	0,500548 / 1 df / Out	0,161044 / 1 df / Out	0,546881 / 1 df / Out
NH3 * RF	0,452509 / 1 df / Out	0,0696698 / 1 df / In	0,00159754 / 1 df / In	0,133662 / 1 df / Out	0,0363626 / 1 df / In
NH3 * Spacing	0,330085 / 1 df / Out	0,256651 / 1 df / Out	9,01105e-05 / 1 df / In	0,288693 / 1 df / Out	0,336750 / 1 df / Out
RF^2	0,293497 / 1 df / Out	0,187293 / 1 df / Out	1,96787e-05 / 1 df / In	0,306413 / 1 df / Out	0,584444 / 1 df / Out
RF * Spacing	0,0671334 / 1 df / In	0,299293 / 1 df / Out	0,0164288 / 1 df / In	0,345086 / 1 df / Out	0,661993 / 1 df / Out
Spacing^2	0,0467674 / 1 df / In	0,0731177 / 1 df / In	0,0124792 / 1 df / In	0,304294 / 1 df / Out	0,0313008 / 1 df / In
R-Squared	0,9980	0,6753	0,9994	0,9754	0,9485
Adj. R-Squared	0,997344	0,562886	0,999128	0,972271	0,935573
RMS Error	1,853080553	0,008822915	9,292622581	0,127500257	0,436712935
Residual DF	27	26	23	31	28

SiN-m - Term Significance - Chamber A2

Term	Dep. Rate [nm/min]	Ref. Index	Avg. Stress [MPa]	SiH	NH
Constant	0,0244968 / 1 df / In	1,2212e-14 / 1 df / In	0,088051 / 1 df / In	0,844470 / 1 df / In	0,000207678 / 1 df / In
SiH4 [sccm]	1,6266e-06 / 1 df / In	0,00158541 / 1 df / In	0,451062 / 1 df / In	3,22293e-07 / 1 df / In	3,74900e-08 / 1 df / In
NH3 [sccm]	0,0626268 / 1 df / In	0,0091968 / 1 df / In	0,0638122 / 1 df / In	0,102310 / 1 df / Out	0,574396 / 1 df / In
RF Power [W]	0,00140037 / 1 df / In	0,785967 / 1 df / In	0,560765 / 1 df / In	0,217245 / 1 df / In	0,438794 / 1 df / In
Spacing [mils]	5,66880e-13 / 1 df / In	0,0369334 / 1 df / In	0,00542782 / 1 df / In	0,224410 / 1 df / In	0,00877512 / 1 df / In
SiH4 [sccm]^2	0,0273824 / 1 df / In	9,80396e-07 / 1 df / In	3,24740e-13 / 1 df / In	1,67431e-05 / 1 df / In	0,632697 / 1 df / Out
NH3 [sccm] * SiH4 [sccm]	0,00176838 / 1 df / In	0,691856 / 1 df / Out	0,000222176 / 1 df / In	0,0851518 / 1 df / Out	0,392092 / 1 df / Out
RF Power [W] * SiH4 [sccm]	0,0113026 / 1 df / In	0,0993350 / 1 df / In	0,00000 / 1 df / In	5,5112e-16 / 1 df / In	4,54897e-06 / 1 df / In
SiH4 [sccm] * Spacing [mils]	0,914446 / 1 df / Out	0,432704 / 1 df / Out	0,945029 / 1 df / In	0,170708 / 1 df / Out	0,565879 / 1 df / Out
NH3 [sccm]^2	0,0472375 / 1 df / In	0,807652 / 1 df / Out	0,216378 / 1 df / In	0,118097 / 1 df / Out	0,816122 / 1 df / Out
NH3 [sccm] * RF Power [W]	0,715279 / 1 df / Out	0,0256378 / 1 df / In	0,013656 / 1 df / In	0,0955497 / 1 df / In	0,000316028 / 1 df / In
NH3 [sccm] * Spacing [mils]	0,477676 / 1 df / Out	0,590371 / 1 df / Out	0,000930918 / 1 df / In	0,249196 / 1 df / In	0,0124398 / 1 df / In
RF Power [W]^2	0,237727 / 1 df / Out	0,240720 / 1 df / Out	3,02733e-05 / 1 df / In	0,00124012 / 1 df / In	0,222104 / 1 df / Out
RF Power [W] * Spacing [mils]	0,124681 / 1 df / Out	0,249205 / 1 df / Out	0,00090909 / 1 df / In	0,227421 / 1 df / In	0,646232 / 1 df / In
Spacing [mils]^2	0,425799 / 1 df / Out	0,759812 / 1 df / Out	0,0309919 / 1 df / In	0,218573 / 1 df / In	0,00261264 / 1 df / In
R-Squared	0,9980	0,7858	0,9992	0,9844	0,9719
Adj. R-Squared	0,997395	0,732289	0,998827	0,981852	0,963629
RMS Error	1,932558794	0,007454779	10,39383666	0,120161501	0,320890263
Residual DF	27	28	23	30	27

Figure 7.3: Significant Terms for SiN-m on Producer A1 and A2. Significance value <0.05 moves term into calculation, a value >0.10 out.
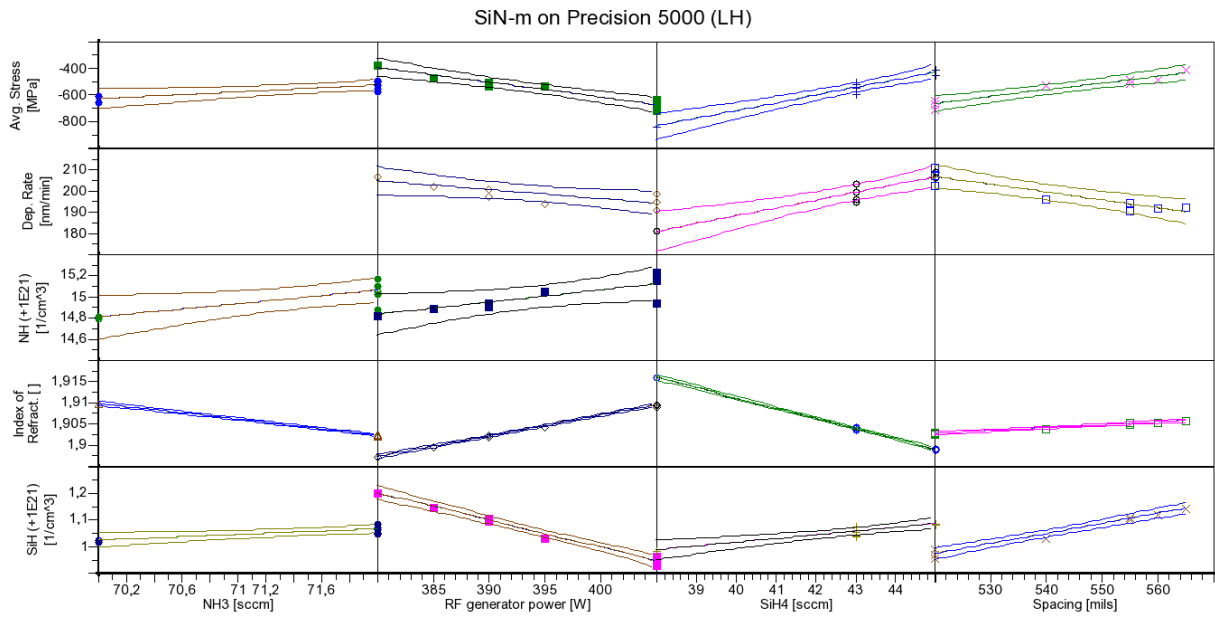
85

Figure 7.4: Adjusted response graph for SiN-m on Precision 5000. Confidence level is set to be 0.95. This graph is meant to illustrate that the influences of the factors have the same tendencies, no matter if CxZ or LH system. As no sophisticated DoE is behind this graph, only linear regressions are possible and the significance value for moving terms out is >0.30.

Term Significance

Term	Dep. Rate	Ref. Index	Avg. Stress	SiH	NH
Constant	0,0988473 1 df In	1,77994e-06 1 df In	0,144852 1 df In	0,431778 1 df In	0,468072 1 df In
SiH4	0,0178849 1 df In	8,12627e-05 1 df In	0,0138583 1 df In	0,115650 1 df In	0,708986 1 df Out
NH3	0,463509 1 df Out	0,000360162 1 df In	0,164147 1 df In	0,281499 1 df In	0,162847 1 df In
RF	0,229070 1 df In	0,000362373 1 df In	0,0579712 1 df In	0,0299432 1 df In	0,211440 1 df In
Spacing	0,0620020 1 df In	0,0110223 1 df In	0,0509516 1 df In	0,0439156 1 df In	0,756957 1 df Out
N2	0,317891 1 df Out	0,716006 1 df Out	0,994425 1 df Out	0,214976 1 df In	0,0971762 1 df In
R-Squared	0,8565	0,9988	0,9880	0,9967	0,6791
Adj. R-Squared	0,748917	0,997186	0,971934	0,988369	0,438342
RMS Error	3,926911651	0,000325408	45,45599609	0,021414603	0,111591983
Residual DF	4	3	3	2	4

Figure 7.5: Significant Terms for SiN-m on Precision 5000. Significance value <0.05 moves term into calculation, a value >0.30 out.
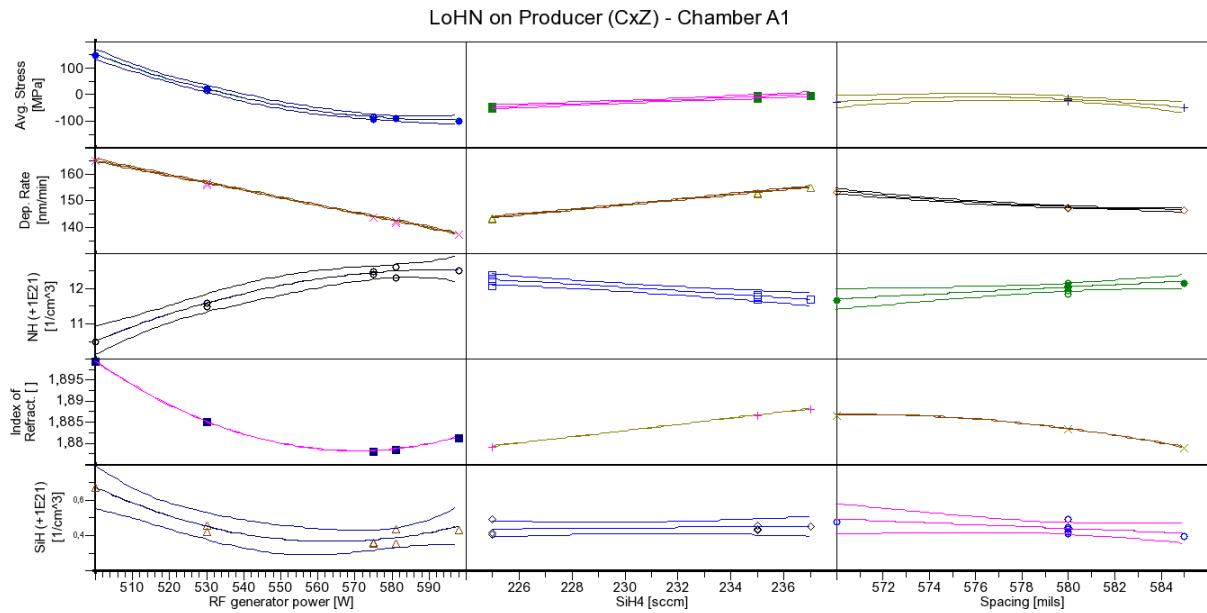
Figure 7.6: Adjusted response graph for LoHN on Producer. Confidence level is set to be 0.95.

Term Significance

Term	Dep. Rate	Ref. Index	Avg. Stress	SiH	NH
Constant	0,0678264 1 df In	0,0281579 1 df In	0,353530 1 df In	0,0488809 1 df In	0,0847709 1 df In
SiH4	0,0732115 1 df In	0,0356362 1 df In	0,152676 1 df In	0,742314 1 df Out	0,0345407 1 df In
RF Power	0,0243129 1 df In	0,0145277 1 df In	0,143166 1 df In	0,0367683 1 df In	0,0455897 1 df In
Spacing	0,0785683 1 df In	0,0224447 1 df In	0,341850 1 df In	0,365791 1 df In	0,142874 1 df In
SiH4^2	0,540793 1 df Out	0 df Out	1 df Out	0,777397 1 df In	0,804230 1 df Out
RF Power^2	0,540793 1 df Out	0,00758047 1 df In	0,156061 1 df In	0,0390684 1 df In	0,0552634 1 df In
Spacing^2	0,0809248 1 df In	0,0222259 1 df In	0,341949 1 df In	0,627271 1 df Out	0,900598 1 df Out
RF Power * SiH4	0,0359218 1 df In	0,0554294 1 df In	1 df Out	0,445192 1 df Out	0,656703 1 df Out
R-Squared	0,9998	1,0000	0,9987	0,9324	0,9901
Adj. R-Squared	0,999202	0,999980	0,992104	0,842224	0,976831
RMS Error	0,37895161	4,71407e-05	9,808443114	0,041441844	0,139163171
Residual DF	2	1	1	3	3

Figure 7.7: Significant Terms for LoHN on Producer. Significance value <0.05 moves term into calculation, a value >0.30 out.

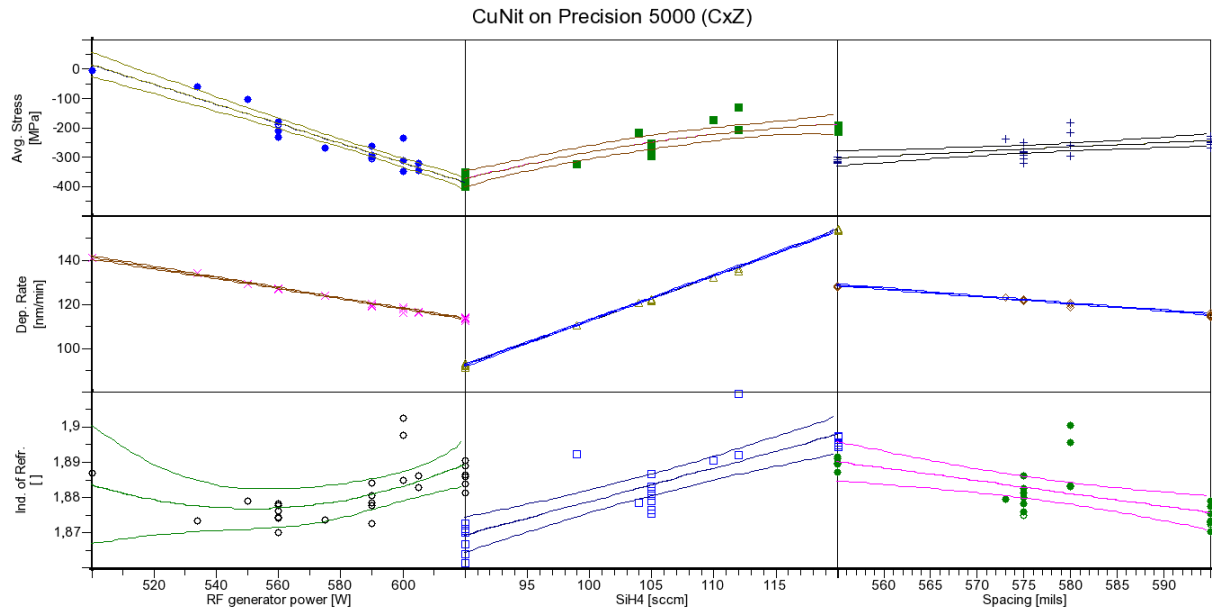Figure 7.8: Adjusted response graph for CuNit on Precision 5000. Confidence level is set to be 0.95.

Term	Dep. Rate [nm/min]	Ref. Index [ ]	Avg. Stress [MPa]
Constant	0,0275493 1 df In	0,00391443 1 df In	0,588836 1 df In
SiH4 [sccm]	0,00958316 1 df In	0,0127922 1 df In	0,152161 1 df In
RF Power [W]	0,0410799 1 df In	0,00529247 1 df In	0,000650880 1 df In
Spacing [mils]	0,0292492 1 df In	0,00609736 1 df In	0,0376075 1 df In
SiH4 [sccm]^2	0,00106502 1 df In	0,630276 1 df Out	0,0203306 1 df In
RF Power [W] * SiH4 [sccm]	0,0282506 1 df In	0,0128162 1 df In	0,0174282 1 df In
SiH4 [sccm] * Spacing [mils]	0,0173869 1 df In	0,0108309 1 df In	0,0996759 1 df In
RF Power [W]^2	0,133566 1 df Out	0,0374130 1 df In	0,890862 1 df Out
RF Power [W] * Spacing [mils]	0,0391016 1 df In	0,00653901 1 df In	0,328866 1 df Out
Spacing [mils]^2	0,247385 1 df Out	0,749251 1 df Out	0,445382 1 df Out
RF Power [W] * SiH4 [sccm] * Spacing [mils]	0,0373340 1 df In	0,0110788 1 df In	0,359824 1 df Out
R-Squared	**0,9995**	**0,8239**	**0,9570**
Adj. R-Squared	**0,999308**	**0,745564**	**0,944159**
RMS Error	**0,632306642**	**0,007143902**	**30,41408416**
Residual DF	**18**	**18**	**20**

Figure 7.9: Significant Terms for CuNit on Precision 5000. Significance value <0.05 moves term into calculation, a value >0.10 out.

Height

sample: LoHN - 40nm

Digital Instruments NanoScope
Scan size   10.00 μm
Scan rate   0.2001 Hz
Number of samples   512
Image Data   Height
Data scale   5.000 nm
Engage X Pos   -19783.4 um
Engage Y Pos   -42151.3 um

Image Statistics

Img. Z range	8.908 nm
Img. Rms (Rq)	0.502 nm
Img. Ra	0.376 nm
Img. Rmax	8.908 nm
Img. Srf. area	100.07 μm²
Img. Prj. Srf. area	100.00 μm²

Box Statistics

Z range	4.761 nm
Rms (Rq)	0.480 nm
Mean roughness (Ra)	0.366 nm
Surface area	2.597 μm²
Proj. Surf. area	2.595 μm²
Surface area diff	0.066 %
Box x dimension	1.722 μm
Box y dimension	1.507 μm

view angle
light angle

0 °

X 2.000 μm/div
Z 5.000 nm/div

Figure 7.10: AFM images and roughness calculation for a 40 nm LoHN film. The comparision between average roughness (Rms) across the whole sample (5.0 Å), and inside the small box (4.8 Å) indicates that the surface is free from particles and homogeneous.
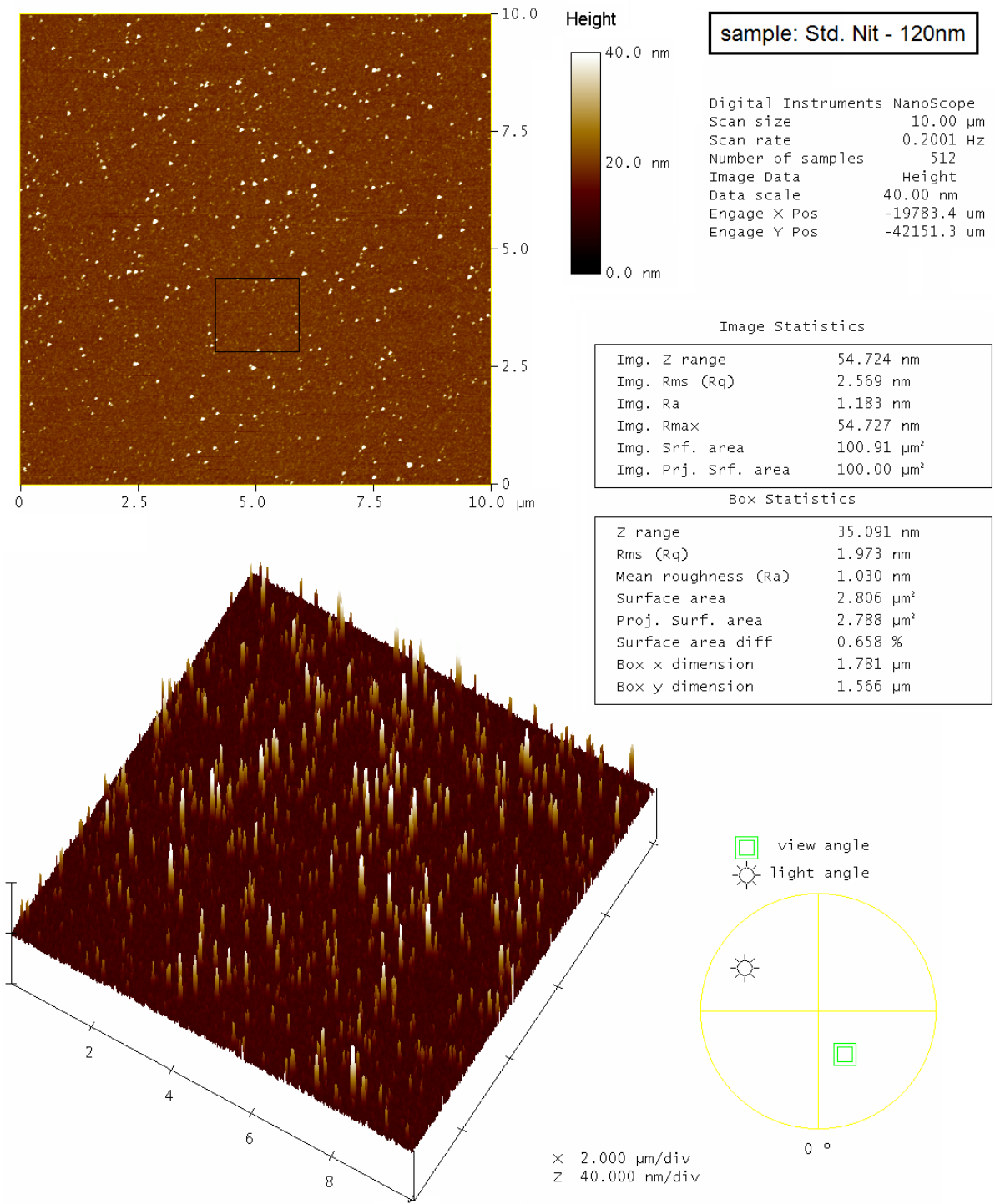
Figure 7.11: AFM images and roughness calculation for a 120 nm Std. Nit film. The high value for the Z range in both, the full area and inside the box shows, that the sample surface has strong variations on several positions. This peaks are presumably particles but they might also be small platelet-type crystalline areas that protrude out from the surface as reported in [16].

7.2 n and k for SiN-m and LoHN

Compared to figure 3.4, which shows the refractive index *n* and extinction coefficient *k* for a 400 nm Std. Nit film, the light absorption for SiN-m and LoHN films starts at shorter wavelengths. This can be explained by the lower amount of Si-H bonds which cause absorption in the UV region.
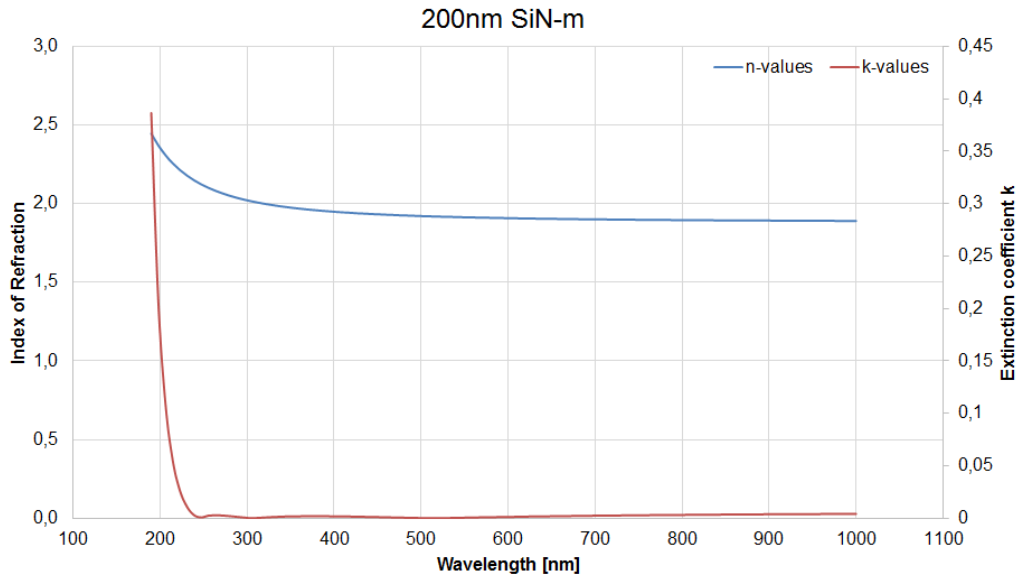
Figure 7.12: Frequency dependence of n and k of a 200 nm SiN-m film. Light absorption starts at approximately 250 nm.
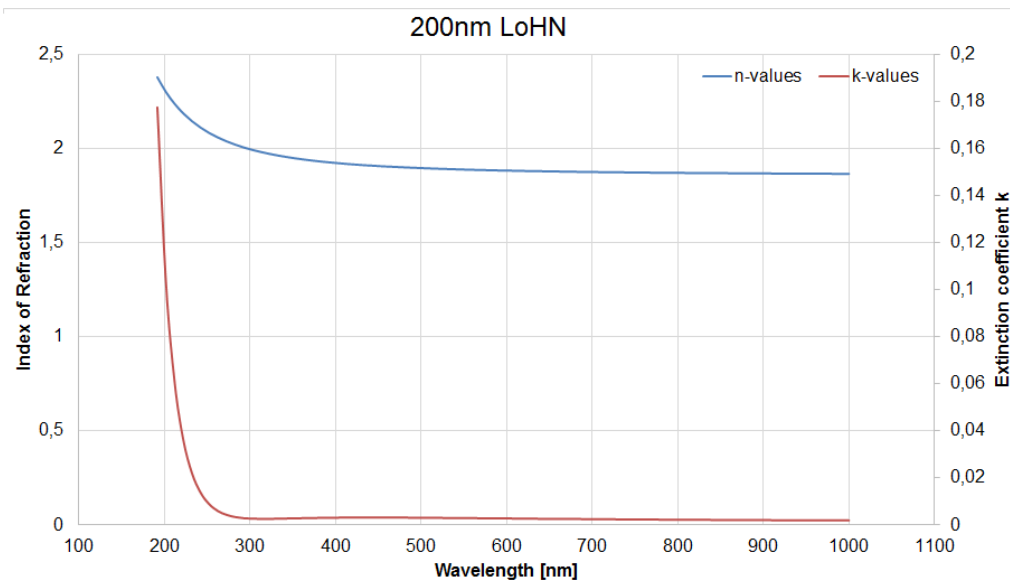
Figure 7.13: Frequency dependence of n and k of a 200 nm LoHN film. Light absorption starts at approximately 290 nm.

7.3 FTIR Spectra Comparison
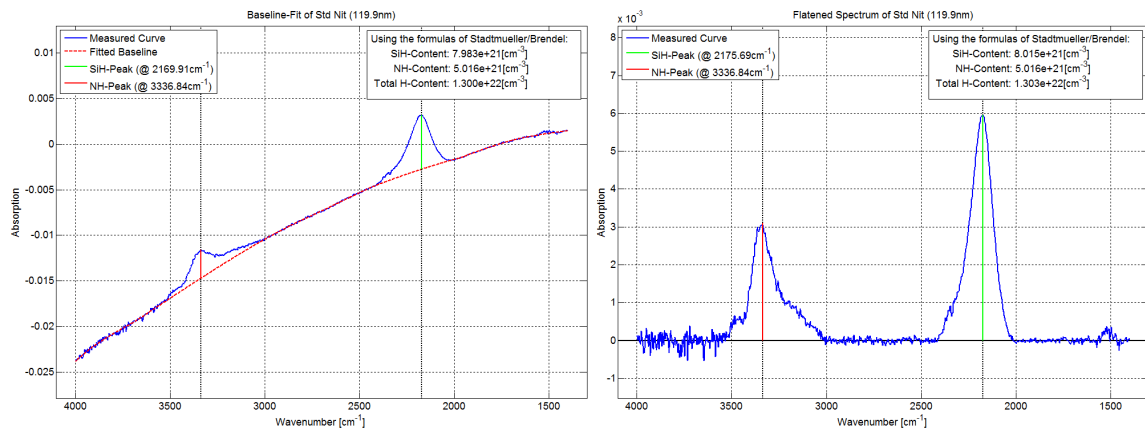
Figure 7.14: Std. Nit 120 nm, SiH/NH ratio: 1.598, Si/N ratio: 0.834, x inside SiN_x: 1.20
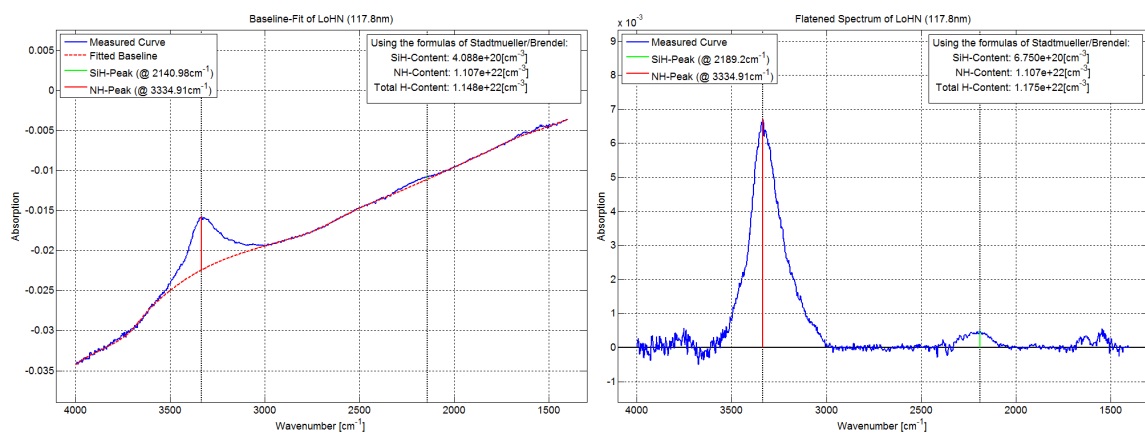
Figure 7.15: LoHN 120 nm, SiH/NH ratio: 0.061, Si/N ratio: 0.705, x inside SiN_x: 1.42
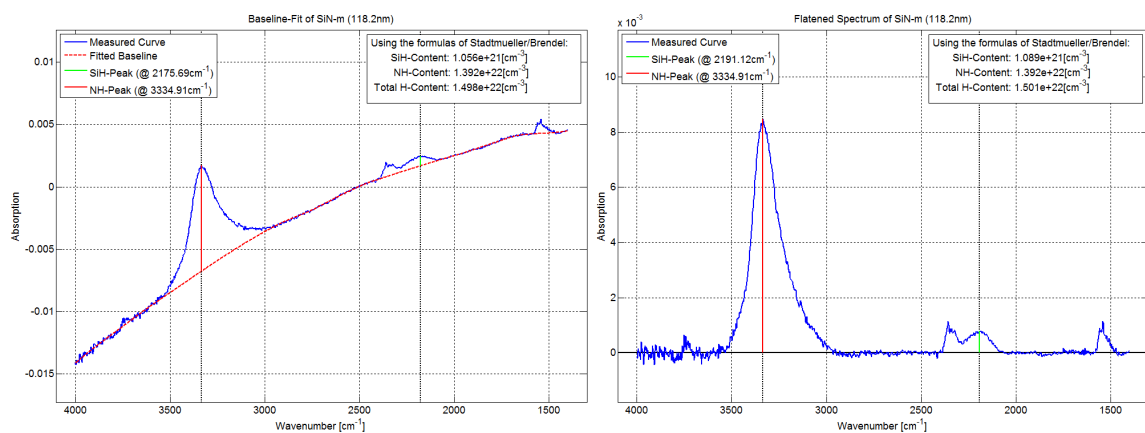
Figure 7.16: SiN-m 120 nm, SiH/NH ratio: 0.078, Si/N ratio: 0.707, x inside SiN_x: 1.42

7.4 Electric Characterization

7.4.1 Charging and Heat Treatment Effect
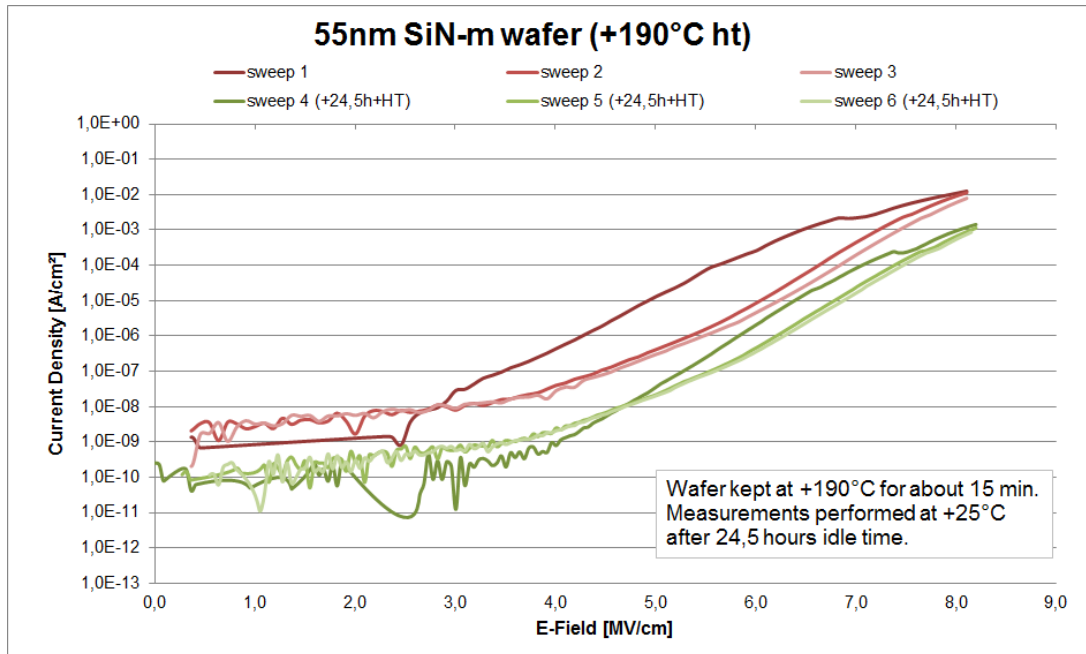
Figure 7.17: Influence of heat treatment (15min. @ 190 °C) and 3 conditioning sweeps (red) on SiN-m film. The leakage current density drops by approximately one decade compared with the virgin material without heat treatment.

7.4.2 LoHN EDX Analysis
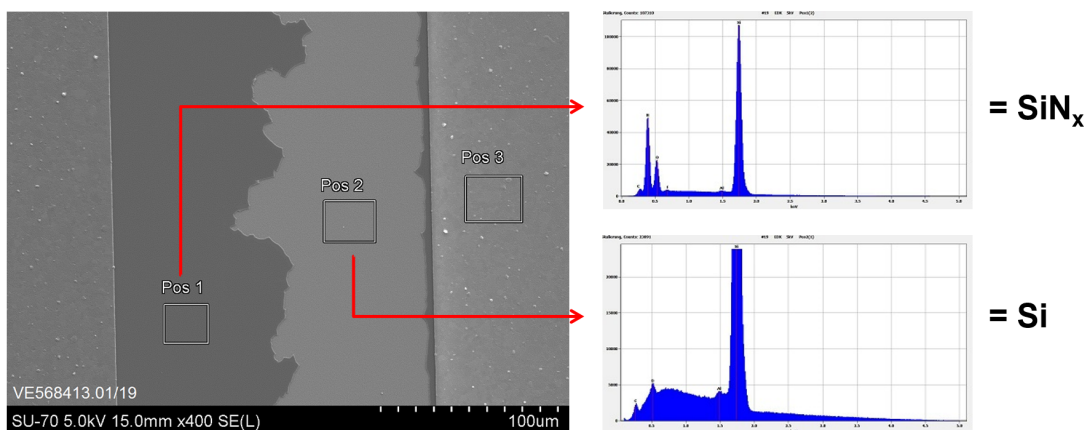
Figure 7.18: EDX analysis of the stains visible on 200 nm LoHN wafer. While position 1 is the LoHN film, position 2 exhibits the blank substrate wafer. Position 3 is the sputtered AlSiCu electrode.

7.4.3 Relative Permittivity Measurement

Site according to 8Z9PKT layout	SiN-m					Std. Nit					LoHN				
	40 [nm] film	60 [nm] film	80 [nm] film	100 [nm] film	120 [nm] film	40 [nm] film	60 [nm] film	80 [nm] film	100 [nm] film	120 [nm] film	40 [nm] film	80 [nm] film	100 [nm] film	120 [nm] film	150 [nm] film
1	7,17	5,79	7,09	6,43	7,05	6,20	5,49	6,21	2,95	4,52	4,50	5,80	5,62	6,46	6,39
2	7,32	6,09	7,12	6,59	7,05	6,11	5,60	6,45	3,46	4,58	4,53	4,98	5,41	6,30	6,57
3	7,34	6,10	7,07	6,59	7,04	6,11	5,56	6,44	3,46	4,61	4,58	5,51	5,90	6,29	6,68
4	7,34	6,16	7,08	6,63	7,06	6,16	5,66	6,48	2,87	4,60	4,50	5,45	5,73	6,36	6,54
5	7,13	6,14	7,02	6,60	7,08	6,15	5,62	6,45	3,23	4,57	3,73	5,74	5,70	6,43	6,51
6	7,31	6,12	7,07	6,61	7,04	6,08	5,58	6,49	3,59	4,64	4,15	5,72	5,88	6,28	6,62
7	7,29	6,14	7,12	6,62	7,09	6,10	5,60	6,54	3,85	4,65	4,91	5,89	6,26	6,46	6,81
8	7,32	6,10	7,11	6,62	7,07	6,14	5,67	6,55	3,63	4,67	4,64	5,51	5,59	6,40	6,52
9	7,30	6,12	7,07	6,61	7,01	6,15	5,59	6,55	3,82	4,71	4,44	5,84	6,10	6,43	6,77
Avg. ε_r	7,28	6,08	7,08	6,59	7,05	6,13	5,60	6,46	3,43	4,62	4,44	5,60	5,80	6,38	6,60
Std. Dev.	0,08	0,11	0,03	0,06	0,02	0,04	0,06	0,10	0,35	0,06	0,33	0,28	0,26	0,07	0,13
Min. ε_r	7,13	5,79	7,02	6,43	7,01	6,08	5,49	6,21	2,87	4,52	3,73	4,98	5,41	6,28	6,39
Max. ε_r	7,34	6,16	7,12	6,63	7,09	6,20	5,67	6,55	3,85	4,71	4,91	5,89	6,26	6,46	6,81

Relative permittivity ε_r for SiN$_x$ films with different thicknesses at 1MHz

Figure 7.19: Recorded values of the relative permittivity (ε_r) measurement on the different silicon nitride variants. A thickness dependence can be observed for the LoHN wafers.

7.4.4 Conduction Mechanisms

As mentioned in section 4.3.1 a too short voltage range for the conditioning sweeps can make a proper data analysis difficult. Picture 7.20 shows such a case.
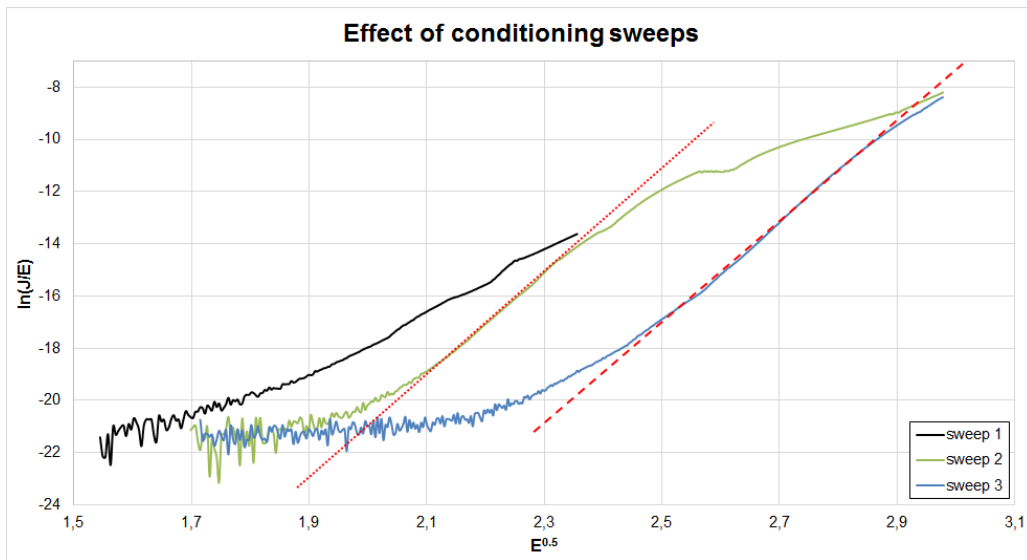

Figure 7.20: Effect of conditioning sweeps with too short range.

When the material is conditioned only till the end of the black line, the slope of the linear fit (dotted line) is likely to be different as if the material was conditioned until the end of the green line and then the fit is performed (dashed line).
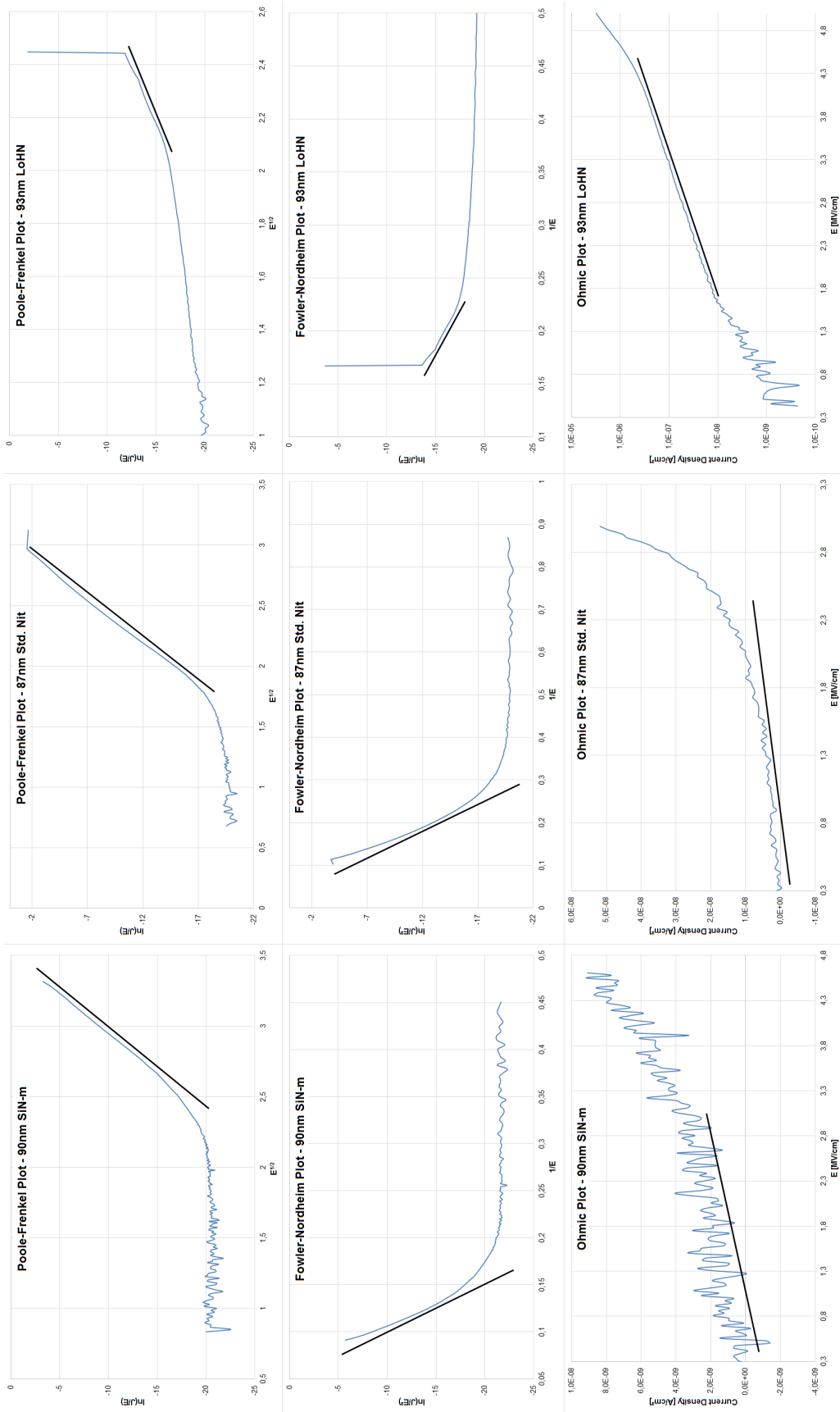
94

Figure 7.21: Graphical approach to identify the dominant conduction mechanism for 100 nm SiN$_x$ films
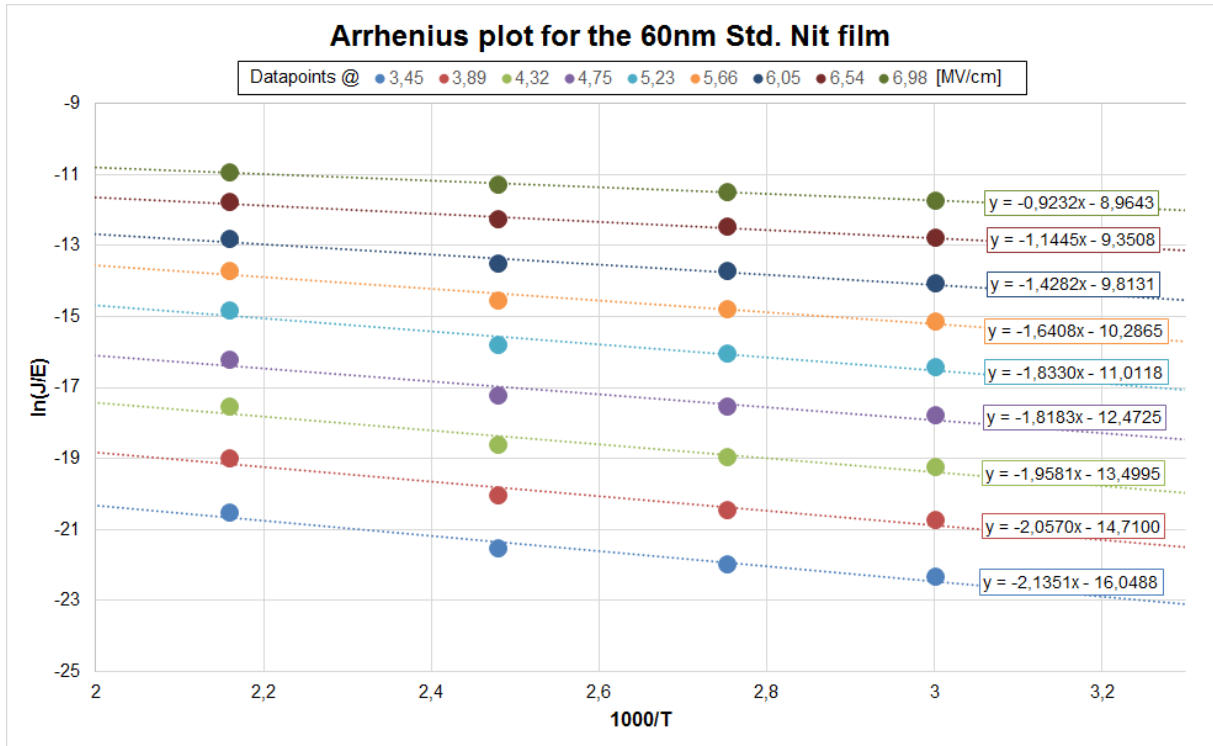
7.4.5 Extraction of Trap Depth

Figure 7.22: Change of leakage current density with temperature in shape of an Arrhenius plot for the Std. Nit film. The values of each slope is then plotted versus the respective field to extrapolate the trap depth ϕ_T.
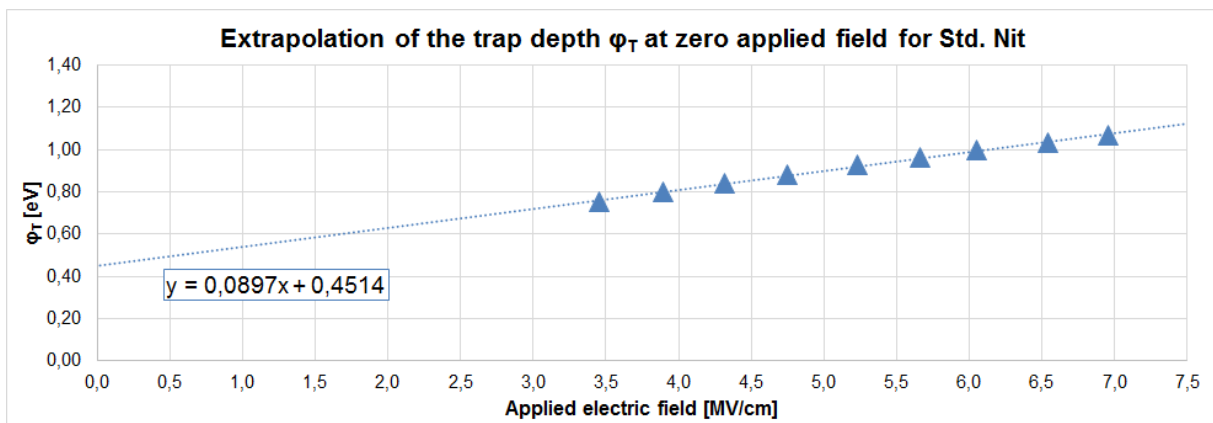

Figure 7.23: The slopes from figure 7.22 are plotted versus their electric fields to extract the trap depth ϕ_T in zero applied field for the 60 nm Std. Nit film.

7.5 Abbreviations and Symbols

Abbreviation	Meaning
AFM	Atomic Force Microscope
BL	Baseline
CVD	Chemical Vapor Deposition
db	Dangling bond
DoE	Design of Experiments
EDX	Energy Dispersive X-Ray
FN tunneling	Fowler-Nordheim tunneling
FTIR	Fourier Transform Infrared
LPCVD	Low-Pressure CVD
MIM (MIS)	Metal Insulator Metal (Semiconductor)
PECVD	Plasma-Enhanced CVD
PF emission	Poole-Frenkel emission
RI	Refractive Index
RF	Radio frequency
SMU	Source Monitor Unit

Symbol	Comment	Unit
A^*	Richardson's constant	A cm^{-2} K^{-2}
n	refractive index	dimensionless
k	extinction coefficient	dimensionless
α	absorption coefficient	cm^{-1}
N_c	density of states in conduction band	cm^{-3}
Φ_B	barrier height	eV
Φ_T	trap height	eV
a	mean hopping distance	Å
λ	wavelength	nm
σ	stress	MPa
ε_r	relative permittivity	dimensionless
ε_0	vacuum permittivity	8.8542E-12 Fm^{-1}
q	elementary charge	1.6022E-19 C
h	Planck's constant	6.6261E-34 Js
k_B	Boltzmann's constant	1.3806E-23 JK^{-1}

7.6 Acknowledgements